Coda Wave Interferometry for Accurate Simultaneous Monitoring of Velocity and Acoustic Source Locations in Experimental Rock Physics

Coda Wave Interferometry for Accurate Simultaneous Monitoring of Velocity and Acoustic Source Locations in Experimental Rock Physics

J. Singh[1,3], A. Curtis[1,2,3], Y. Zhao[1], A. Cartwright-Taylor[1,3], I. Main[1,3]

[1]University of Edinburgh, School of GeoSciences, Edinburgh, UK

[2]ETH Zurich, Switzerland

[3]The International Centre for Carbonate Reservoirs, Edinburgh, UK

Key Points:

- Conventional methods for measuring changes in seismic velocity and source locations may be inaccurate, especially in a high-frequency regime
- CWI provides far greater accuracy in estimating changes in velocity and between source locations, even with high background noise levels
- A new method is presented to infer both P and S wave average velocity changes from coda wave interferometry

This article has been accepted for publication and undergone full peer review but has not been through the copyediting, typesetting, pagination and proofreading process which may lead to differences between this version and the Version of Record. Please cite this article as doi: 10.1029/2019JB017577

Corresponding author: Jonathan Singh, jonathan.singh@ed.ac.uk

Abstract

In many geoscientific, material science and engineering applications it is of importance to estimate a representative bulk seismic velocity of materials, or to locate the source of recorded seismic or acoustic waves. Such estimates are necessary in order to interpret industrial seismic and earthquake seismological data, for example in non-destructive evaluation and monitoring of structural materials, and as an input to rock physics models that predict other parameters of interest. Bulk velocity is commonly estimated in laboratories from the time-of-flight of the first-arriving wave between a source and a receiver, assuming a linear raypath. In heterogeneous media, that method provides biased estimates of the bulk velocity, and of derived parameters such as temporal velocity changes or the locations of acoustic emissions. We show that Coda Wave Interferometry (CWI) characterizes changes in the bulk properties of scattering media far more effectively on the scale of laboratory rock samples. Compared to conventional methods, CWI provides significant improvements in both accuracy and precision of estimates of velocity changes, and distances between pairs of acoustic sources, remaining accurate in the presence of background noise, and when source location and velocity perturbations occur simultaneously. CWI also allows 3D relative locations of clusters of acoustic emissions to be estimated using only a single sensor. We present a method to use CWI to infer changes in both P and S wave velocities individually. These innovations represent significant improvements in our ability to characterize the evolution of properties of media for a variety of applications.

1 Introduction

Experimental studies of wave propagation in rock cores are often performed to deduce relationships between changes in external conditions and seismic properties such as seismic velocity (Wang, 2001), anisotropy (Christensen, 1966; Sayers & Kachanov, 1995) and attenuation (Sams, Neep, Worthington, & King, 1997; Toksöz, Johnston, & Timur, 1979), and to examine the process of rock fracturing (Pyrak-Nolte, Myer, & Cook, 1990) or the distribution of acoustic emissions (Lockner, 1993; Lockner, Byerlee, Kuksenko, Ponomarev, & Sidorin, 1992). Established relationships between seismic attributes and underlying rock physical properties are particularly important for monitoring purposes in the hydrocarbon industry and in subsurface CO_2 storage projects, notably for relating effective stress changes during subsurface injection or production to changes that may

be observed in the seismic velocity (Arts et al., 2004; Brown, 2002; Guilbot & Smith, 2002; Herwanger & Horne, 2009; Stork, Allmark, Curtis, Kendall, & White, 2018). It is therefore of great importance that models developed from laboratory experiments accurately represent the response of in-situ rocks.

Standard methods for measuring either the velocity, or changes in the velocity of a medium involve picking of first-break arrival times of seismic waves traveling between a fixed source and receiver pair. The term 'first-break' is ambiguous, and can be taken to mean the signal onset which is the time of first-arriving energy (Brillouin, 1960), the arrival time of the first peak or the time of first zero-crossing (Hornby, 1998). Manual picking of first-breaks is slow and may incur inconsistent user bias and error, therefore there are many methods available for automatic picking of first-breaks (Boschetti, Dentith, & List, 1996; Earle & Shearer, 1994; Ervin, McGinnis, Otis, & Hall, 1983; Hatherly, 1982; Molyneux & Schmitt, 1999; Peraldi & Clement, 1972). Here, unless otherwise stated, we use the term first-break method to mean picking the first maximum (or extremum). This represents the point with the highest signal to noise ratio. The velocity of the medium is then estimated using the known straight-line distance between the source and receiver. For many laboratory experiments measuring such velocities, the wavelengths used are on the same order as heterogeneities in the medium (e.g., pore and grain sizes). Obvious problems then occur: 1) the measured velocity is not sensitive to the bulk properties of a medium, but rather to properties along a very specific (fastest) ray path between the source and receiver, resulting in a bias towards higher velocities. 2) The path followed by the first-arriving energy is unlikely to be straight, so that velocity estimates made using the straight-line path are biased towards lower values. 3) Biases in points 1 and 2 are generally unrelated so are not expected to cancel. 4) The effects of small perturbations in the medium that are not located along the specific source-receiver path cannot be detected. 5) Such systematic and random errors in velocity estimation are carried forward to any subsequent calculations, notably for example to the location of acoustic source positions. Also, the presence of attenuation and dispersion changes the shape of a propagating wave (Molyneux & Schmitt, 2000), thus the determination of meaningful velocity measurements can be problematic.

Weaver and Lobkis (2001) and Lobkis and Weaver (2001) showed that information about a medium can be extracted from recordings of coda waves and background ambient noise. Coda waves are the multiply-scattered waves that are recorded after the ar-

rival of the main ballistic waves. Recordings of coda waves are far more sensitive than first arrivals to changes in pore-pressure, fracture density and temperature (Snieder, Grêt, Douma, & Scales, 2002; Vlastos et al., 2006; Vlastos, Liu, Main, & Narteau, 2007), due to the fact that coda waves follow much longer and more complex paths, eventually sampling the entire medium, and sampling any sub-volume of the medium multiple times. There are now established methods grouped under the name *coda wave interferometry* (CWI) that estimate *changes* in the velocity of the medium (rather than the absolute velocity), or changes in the locations of sources or receivers using the coda (Snieder, 2006). There have been several field and laboratory applications of CWI to date, including the monitoring of velocity changes in ice sheets (James, Knox, Abbott, & Screaton, 2017; Mordret, Mikesell, Harig, Lipovsky, & Prieto, 2016), concrete (Larose & Hall, 2009; Planès & Larose, 2013), mining environments (Grêt, Snieder, & Özbay, 2006), and volcanic regions (Sens-Schönfelder & Wegler, 2006). CWI has also been used to study earthquake focal mechanisms (Robinson, Snieder, & Sambridge, 2007), earthquake separation distances (Robinson, Sambridge, & Snieder, 2011; Snieder & Vrijlandt, 2005), and source network locations of induced micro-seismic events (Zhao & Curtis, 2019; Zhao, Curtis, & Baptie, 2017). So far its implications for the interpretation of laboratory rock physics experiments has been comparatively limited.

In this paper we test the hypothesis that Coda Wave Interferometry (CWI) can provide an improvement in accuracy and precision when inferring and quantifying the changes in bulk velocity and relative source locations in rock samples in laboratory settings. We test the hypotheses that CWI provides more representative measures of bulk properties, in comparison with commonly used methods in numerical and laboratory experiments at the core-scale, and at high frequencies commonly used in a laboratory setting.

First we outline the theory of Coda Wave Interferometry and how it can be used in an experimental setting. Then we examine multiple samples of varying rock type and heterogeneity using both numerical simulations and laboratory experiments, where changes in source location and velocity are estimated using both CWI and standard methods (manually-picked first breaks for velocities and multilateration for source locations). We show how changes in source position and velocity can be jointly estimated by CWI when both perturbations occur simultaneously. We then demonstrate an optimization algorithm for estimating the relative locations of sources within a cluster, given the source separations

estimated from CWI, and show that it can be applied even in the case of having only a single transducer. Following this, we test the sensitivity of CWI as well as conventional methods to increasing contamination of noise. In all cases CWI is shown to out-perform conventional methods.

Accompanying this manuscript, we provide a well-commented set of MATLAB functions for implementing the CWI method to estimate velocity changes, and for the joint estimation of velocity change and source separation. These codes use a form of CWI that estimates changes relative to a moving reference seismogram, which is particularly important for longer deformation experiments in which scattering paths may change significantly, a situation which contravenes the assumptions of standard CWI theory, and requires the reference seismogram to be updated periodically. Together with the suite of CWI codes made publicly available by Zhao and Curtis (2019) this allows all techniques used in this paper to be implemented and reproduced.

2 Coda Wave Interferometry (CWI)

CWI is a method that allows small changes in velocity, the displacement of source or receiver locations, or movement of scatterers to be monitored (Sens-Schönfelder & Wegler, 2006; Snieder, 2006; Snieder et al., 2002). These different perturbations and their effect on recorded signals are illustrated in Figure 1. First consider the effect of a velocity perturbation (ΔV in Figure 1a). The direct arriving wave between a source and receiver would only sample the perturbation once (or not at all), whereas the multiply reflected wavefield samples the perturbation many times. Therefore the change in arrival times for later arriving waves (time window iv) is larger than for the first arrival (time window i). The second perturbation type is a displacement of the source or receiver location (Figure 1b shows a source displacement). In this case, the difference in ray paths before and after the perturbation is the path between the source and the first scattering point (blue arrows in Figure 1b). Different paths are shortened or lengthened depending on the location of the first scatterer; this is reflected by the advancement and retardation of peaks highlighted by red and blue arrows. Providing the source displacement is small, the extent to which these travel times are perturbed (specifically, the variance of the perturbation) is directly proportional to the displacement. The third perturbation type is the displacement of all scattering points (yellow circles in Figure 1c): in this case, all paths between scattering points are perturbed (both shortened and lengthened),

and similarly to the previous case the variance of travel time perturbations is proportional to the displacement of scattering points. All three perturbation types can be monitored by using a cross correlation of the unperturbed (u_{unp}) and perturbed (u_{per}) waveforms - the waveforms from the source recorded by the receiver before and after the change or displacement takes place.

One method to estimate the change in velocity is known as trace stretching (Sens-Schönfelder & Wegler, 2006), where the perturbed waveform is assumed to be a time-stretched version of a reference waveform; this follows if one assumes that a velocity perturbation is uniform across the entire medium, so all arriving energy is perturbed at the same temporal rate. This method also assumes no changes in the intrinsic attenuation of the medium. We stretch the time axis of the perturbed signal by a range of stretching factors (ϵ) and compute the correlation coefficient R between $u_{unp}(t)$ and the stretched version of the perturbed waveform $u_{per}(t[1+\epsilon])$ over a given time window (t_1, t_2):

$$R^{(t_1,t_2)}(\epsilon) = \frac{\int_{t_1}^{t_2} u_{unp}(t) u_{per}(t[1+\epsilon])dt}{\sqrt{\int_{t_1}^{t_2} u_{unp}^2(t)dt \int_{t_1}^{t_2} u_{per}^2(t[1+\epsilon])dt'}}. \quad (1)$$

The optimum stretching factor ϵ_{max} that maximizes the correlation coefficient (for which $R = R_{max}$), is related to the ratio of the change in velocity ΔV to the original velocity V by

$$\epsilon_{max} = -\frac{\Delta V}{V}, \quad (2)$$

(Sens-Schönfelder & Wegler, 2006). This method requires that velocity changes are small to avoid cycle skipping in the calculation of R in Equation 1. In cases where the medium changes significantly, such as during material deformation where new scattering paths are introduced due to fracturing, it may not be appropriate to use a constant reference trace (u_{unp}) for all recorded waveforms during deformation. We therefore propose the use of a moving reference trace, where the optimum stretching factor from the initial reference trace (u_0) to any other recorded waveform during deformation (u_n) can be calculated as

$$\epsilon_{u_0 u_n} = \epsilon_{u_0 u_s} + \epsilon_{u_s u_n}, \quad (3)$$

where $\epsilon_{u_i u_j}$ is the stretching factor of trace u_j relative to u_i, $s = k\lfloor n/k \rfloor$, n is the trace number, k is the user-selected step size of the moving reference trace, and $\lfloor \ldots \rfloor$ denotes a floor function, which outputs the greatest integer less than or equal to the argument. Accompanying this manuscript are a suite of MATLAB functions for implementing the

moving-reference stretching CWI method. Snieder (2002) derived the relationship between the inferred medium velocity change from CWI, and changes in P-wave and S-wave velocities in an isotropic case:

$$\frac{\Delta V}{V} = \frac{\beta^3}{2\alpha^3 + \beta^3}\frac{\Delta\alpha}{\alpha} + \frac{2\alpha^3}{2\alpha^3 + \beta^3}\frac{\Delta\beta}{\beta}, \tag{4}$$

where α and β are the velocities of P and S waves, respectively. In an initial Poisson medium where $\alpha = \sqrt{3}\beta$, if either or both of the P or S wave velocity changes then the relation simplifies to

$$\frac{\Delta V}{V} = 0.09\frac{\Delta\alpha}{\alpha} + 0.91\frac{\Delta\beta}{\beta}, \tag{5}$$

and if α and β change such that the Poisson medium is preserved then

$$\frac{\Delta V}{V} = \frac{\Delta\alpha}{\alpha} = \frac{\Delta\beta}{\beta}. \tag{6}$$

The strengths of the CWI technique lie in the ability to resolve very small changes in velocity compared to standard methods. If we take the sampling interval of a recorded signal to be dt, the duration of the signal to be t_{max}, and make the conservative assumption that one sample interval is the smallest resolvable time difference between waveforms in the two recordings, then the maximum resolution of CWI (the smallest resolvable change in velocity that can be measured) is

$$\left[\frac{\Delta V}{V}\right]_{min}^{CWI} = \frac{dt}{t_{max}}. \tag{7}$$

The maximum resolution for measuring $\Delta V/V$ from the standard first-break method would be

$$\left[\frac{\Delta V}{V}\right]_{min}^{FB} = \frac{dt}{(t_0 + dt)}, \tag{8}$$

where t_0 is the first-break arrival time. Both equations 7 and 8 assume no background noise and hence no uncertainty in the recorded waveforms, nor ambiguity in defining a first break which can be highly uncertain in many cases. Inserting typical values for laboratory core scale measurements, such as those used in the experiments in the following section (sampling interval $dt = 0.04\mu$s, signal duration $t_{max} = 640\mu s$, and arrival time $t_0 = 65\mu s$), the smallest perturbations that theoretically can be detected are 0.00625% for CWI and 0.062% for the standard first break method. Hence, CWI offers an order of magnitude improvement in precision in the absence of noise. The CWI method also computes the cross-correlation function using many more data points, which should make it less susceptible to the effects of noise than a single point measure of say the first peak

for the first break estimate. We test the hypothesis that CWI provides a more accurate measure of relative velocity changes in the experiments outlined in Section 3.3.

Another advantage of using CWI is that it allows a joint estimate of both a velocity perturbation and the separation r between two source/receiver locations to be made from a single receiver. This is because velocity perturbation information is retrieved from the consistent phase information along the waveforms, whereas the source or receiver separation is related to the variance of inconsistent phase perturbations and hence to the maximum value of the cross correlation value (R_{max}) in Equation 1, and these two attributes may be observed independently. Figure 1b illustrates how the perturbations of travel times (advancement and retardation of individual peaks) relates to the displacement of the source or receiver. Snieder (2006) derives the relationship between the maximum cross-correlation and the variance of the travel time perturbations (σ_τ^2) as

$$R_{max} = 1 - \frac{1}{2}\bar{\omega}^2\sigma_\tau^2, \tag{9}$$

where $\bar{\omega}^2$ is the dominant mean-squared angular frequency in the recorded waveform which can be computed as:

$$\bar{\omega}^2 = \frac{\int_{t_1}^{t_2} \dot{u}^2(t')dt'}{\int_{t_1}^{t_2} u^2(t')dt'}, \tag{10}$$

where $\dot{u}$ is the temporal derivative of the waveform u. When a source/receiver is displaced relative to another source/receiver by distance r, one can estimate separation r from the variance of the travel time perturbations in a range of scenarios. For isotropic sources in a two-dimensional acoustic medium:

$$\sigma_\tau^2 = \frac{1}{2\alpha^2}r^2. \tag{11}$$

For isotropic sources in a three-dimensional acoustic medium:

$$\sigma_\tau^2 = \frac{1}{3\alpha^2}r^2. \tag{12}$$

For double couple sources on the same fault plane, with the same source mechanism and in elastic media:

$$\sigma_\tau^2 = \frac{(\frac{6}{\alpha^8} + \frac{7}{\beta^8})}{7(\frac{2}{\alpha^6} + \frac{3}{\beta^6})}r^2, \tag{13}$$

where α and β are estimates of the P- and S-wave velocities of the medium (Snieder & Vrijlandt, 2005). These estimates of velocity represent an average for all scattering paths, assuming coda waves are evenly distributed in an isotropic medium. The type of spatial averaging that is implicit in the CWI estimate is analyzed in Section 5.

To summarize, the main advantages of using CWI over conventional first-break method in an experimental setting (at least in theory) are that: 1) CWI is more representative of changes in the bulk properties of a medium because coda waves sample the entire medium. 2) Coda waves sample the same area multiple times, so CWI is capable of resolving smaller changes in the medium giving a theoretical order of magnitude increase in precision for typical laboratory experiments. 3) CWI is generally less susceptible to the presence of noise as it uses many more data points, providing more robust estimates. 4) CWI allows for the separation between nearby sources to be estimated from a single receiver, even in cases where medium velocity changes occur simultaneously, as the two estimates utilize different measurements made from the correlation function in Equation 1. The source-separation data are then sufficient to estimate the 3D relative locations of clusters of sources using CWI with a single receiver. We now test how CWI works in practice, using numerical simulations and laboratory experiments.

3 Results

3.1 Estimating Velocity and Source Locations: Synthetic Examples

Rock cores typically used for geomechanics and rock physics experiments are on the scale of 3 mm to 100 mm in diameter, and seismic wave frequencies studied are on the order of kHz - MHz. At these frequencies, wavelengths are similar to the scale of the key heterogeneities such as pores and grains, therefore many rock samples act as strongly scattering media. Most recorded waves take very complex, long paths and experience multiple reflections, diffractions and reflections (Sato, Fehler, & Maeda, 2012). Therefore there are strong frequency dependent effects on properties derived from ultrasonic recordings at these scales (Mason & McSkimin, 1947). The complex nature of wave propagation through highly scattering media, such as the samples shown in Figure 2, can be studied using methods of digital rock physics (Madonna, Almqvist, & Saenger, 2012). First a reconstructed micro-tomography (μCT) cross-section is segmented into appropriate mineral and pore phases, and converted into velocity and density models (wave physics parameters used for different phases are shown in Table 1). Using finite difference methods (Moczo, Robertsson, & Eisner, 2007), wave propagation through the medium can be simulated so that full waveforms can be generated, as though they have been recorded at any point within the medium. These methods are increasingly used for estimating the acoustic or elastic properties of rocks based on μCT images (Saenger, Madonna, Osorno,

Table 1. Parameters used for finite difference wavefield simulation through the samples shown in Figure 2. Values are Voigt-Reuss-Hill averages taken from Bass (1995) and Mavko et al. (2009).

Phase	**Density (kg/m^3)**	**Velocity (m/s)**
Pore Fluid	1000	1500
Calcite	2710	6500
Plagioclase	2620	6500
Quartz	2650	5800
Potassium Feldspar	2560	6300
Biotite	3090	5260
Muscovite	2790	6460

Uribe, & Steeb, 2014; Saxena & Mavko, 2016). These methods are limited by the resolution of μCT images, which fail to resolve sub-micron scale structures such as any microcracks that may exist.

Our aim is to understand and address problems facing core-scale experimental rock physics, especially where strong scattering occurs. To emulate these physical experiments, we simulate wave propagation using a two-dimensional, acoustic, rotated staggered-grid finite-difference solver, through three different digital rock samples: Tivoli Travertine (TT), Westerly Granite (WG) and Copp-Crag Sandstone (CS). These rock types have been selected to represent a range of types of heterogeneity, where Tivoli Travertine has high porosity with complex pore shapes and pore size distribution, Copp-Crag is a relatively homogeneous sandstone with more uniform pore shapes and pore size distribution, and Westerly Granite is the most homogeneous and exhibits little porosity. The μCT slices and corresponding models of segmented phases for each rock type are shown in Figure 2 and are converted to wave physics models using the parameters stated in Table 1 (assuming isotropic mineralogy). The simulations do not include any effects caused by attenuation or dispersion. Each pixel is mapped to a regular grid of cells used for the finite difference method, with cell sizes of 37.5 μm, 42 μm and 2.9 μm for the TT, CS and WG, respectively. The model includes reflecting boundaries to account for side wall reflections.

The source input pulses used are Ricker wavelets with peak frequencies of 30 MHz for the TT and CS models, and 200 MHz for the smaller WG model. These frequencies are significantly higher than those conventionally used in laboratory experiments, which typically use peak frequencies around 1 MHz for 38 mm core diameter experiments. For comparison with conventional methods, we also use a Ricker wavelet with peak frequency of 1 MHz for the TT model. The simulations here are well within the high-frequency regime (approximate wavelengths for each sample are labeled as λ in Figure 2). We assume a point source and point receivers, much smaller than the apertures of conventional transducers used in laboratory experiments. We also assume perfect transducer coupling, which in a laboratory setting is unknown and may be sensitive to external conditions. Accordingly our results explore a best-case scenario at this stage of the modelling. High-contrast discontinuities such as those between pores and mineral phases may cause instability problems on a staggered grid. To avoid these difficulties, we implement the rotated staggered grid technique (Saenger & Bohlen, 2004).

First, we simulate a single point source located at the top of each sample and a row of point receivers along the bottom (e.g., Figure 3e). Velocity is estimated at each receiver by manually picking the arrival time of the first peak (as well as the signal onset for the TT model) and assuming straight ray paths between the known source and receiver locations (shown in Figure 3a, b, c and d). For the three samples, the estimated velocities at each receiver show considerable variation depending on where the receiver is located. For the TT model, we compare varying the source frequency (1 MHz and 30 MHz) as well as the method used for picking the first arrival (picking the first maximum in panel a in Figure 3, and the signal onset in panel b). The strong variation in velocity depending on receiver position is present for both frequencies and both picking methods. This response is concerning as in many cases a single receiver and hence a simple, non-representative velocity may be used to characterize an entire sample - from a receiver at the center of the core in conventional experimental configurations (shown as dashed black lines in Figure 3). Sometimes a plate-like receiver is used which spans the entire base of the sample; in that case the signal recorded would be approximately equal to the superposition of all the distributed transducers (Li, Schmitt, Zou, & Chen, 2018), and the velocity estimated using this method is shown as a dashed green line.

To further explore the variation of measured velocity, a similar numerical experiment was carried out on the three velocity models in which eikonal ray tracing was im-

plemented using the methods outlined by Margrave (2007). This gives an estimated arrival time ($t[\boldsymbol{x}]$) for every point $\boldsymbol{x}$ in the model for a fixed source location (in this case the source is located at the center-top of each sample). Using these arrival times, we can imagine a receiver placed at every point within and on the boundary of a model, and an estimate of the velocity for that source-to-receiver path can be calculated using the standard travel time method assuming straight rays. Figure 4 shows the calculated velocity $v[\boldsymbol{x}]$ for all model points $\boldsymbol{x}$ in each sample, again showing that measured velocity may be strongly dependent on source and/or receiver locations. For Tivoli Travetine (Figure 4a) the variation in velocity estimates are greater than for Copp-Crag Sandstone (Figure 4c), and Westerly Granite (Figure 4b) has the smoothest image, reflecting the smallest variation in estimated velocity $v[\boldsymbol{x}]$. In all cases the longer the source-to-receiver distance, the more stable is the result.

There are therefore several concerning implications of characterizing a medium with velocities calculated from standard methods: 1) a measured cross-core velocity is not sensitive to the bulk properties of a medium, but rather to the velocities along a specific ray path between the point source and point receiver, as demonstrated by the variation of estimated velocity with receiver position in Figures 3 and 4. Therefore, 2) the effects of small perturbations in a medium that are not located on the specific source-to-receiver path will not be detectable using these methods. In addition, although the results stabilize for a more distant source and receiver pair, they are still expected to stabilize at a velocity that is biased relative to the average across the sample since first-arrival travel times are measured along shortest travel time ray paths.

The assumption that a medium is represented by a single constant 'bulk' velocity also introduces errors into subsequent calculations, such as in the estimation of source locations. This effect can be examined using a further numerical experiment. We simulate a series of regularly spaced sources placed on a rectilinear grid throughout each of the three media, representing acoustic emissions occurring throughout the sample. We measure the arrival times for each source (S) at a set of receivers (i) as t_S^i using the first-break method, and use a single measured velocity through each sample (V_{med}), which is assumed to be representative of the entire medium. In our implementation the exact value of this velocity does not affect source locations - it only affects the estimates of the source origin time (t_0). In this case it is therefore not inaccuracy in the velocity estimate that will effect locations, but rather the assumption that there is a single representative

medium velocity. We estimate source locations (S_{est}) using multilateration, by implementing a grid-search through all model positions ($\boldsymbol{x}$) for each receiver location ($\boldsymbol{x}_i$) and through a range of source origin times (t_0), to find values of $\boldsymbol{x}$, and t_0 that minimize the objective function

$$\varphi(\boldsymbol{x}, t_0) = \sum_{i=1}^{N^i} [V_{med} \times (t_S^i - t_0) - |\boldsymbol{x}_i - \boldsymbol{x}|]. \quad (14)$$

The estimated source location S_{est} is the location $\boldsymbol{x}$ that minimizes φ. Figure 5 displays the systematic error in estimated source locations S_{est} (arrowheads) compared to true locations (arrow tails) for each of the three samples. For the majority of sources in Tivoli Travertine (5a) and Copp-Crag Sandstone (5c), the resulting systematic error in source location is significant in both amplitude and direction. In Westerly Granite (5b), such errors have much smaller amplitudes. It is therefore clear that in more heterogeneous media, a single velocity is not appropriate and estimated source locations in many areas are highly inaccurate when estimated using conventional methods of multilateration assuming a single bulk velocity.

3.2 CWI and Conventional Estimates of Changes in Velocity and Source Location: Synthetic Tests

We now test CWI against conventional methods for measuring a *change* in the velocity of a medium, using finite difference numerical wavefield simulations through the three μCT slices in Figure 2. Two slightly different velocity models for each sample are generated: one is the unperturbed medium and the other has perturbed velocities of both mineral and fluid phases equal to a -1% ($\Delta V/V = -0.01$). The simulated signals are obtained from an array of receiver positions along the bottom of the sample as used in Figure 3. The change in velocity ($\Delta V/V$) between each pair of models is estimated from these signals by CWI (using Equations 1 and 2), and using the conventional method of manual phase-picking of first-break arrivals (time of first peak) assuming straight rays. Figure 6 compares these estimates for each sample. For all samples, CWI gives more accurate (closer to the true perturbation of the model) and more precise (lower standard deviation) estimates of $\Delta V/V$, and is more robust (shows significantly less variation between different receiver locations) when compared to the first-break method. This effect is clearly dependent on the complexity of the medium: the first-break estimates for Tivoli Travertine (Figure 6a) show much stronger variation than those for Westerly Granite (Figure 6b). The CWI estimates for $\Delta V/V$, however, do not vary between samples

of differing complexity. Coda waves sample the entire medium rather than a specific (fastest) ray path, therefore CWI is more robust to changes in receiver location. This consistency of estimates shows that CWI is less dependent on sample complexity, and on receiver location, and confirms the hypothesis that the multiply reflected waves used in CWI effectively sample the entire medium, providing more representative measures of velocity changes from any source and receiver pair.

We also test CWI and conventional methods for estimating *changes* in source locations. For this test, waveforms were simulated for a cluster of sources along a fracture plane in the middle of each of the three samples, and with receivers located at the bottom and at either side of the model (experimental configuration and source cluster locations shown in Figure 5). The standard method of multilateration (minimizing Equation 14) is used to locate source positions for each source in the cluster, assuming a constant bulk velocity which is measured with a single source and receiver placed at the top-center and bottom-center of the sample respectively. CWI provides the separation between pairs of sources (it does not provide source locations in an absolute frame of reference), so Figure 7 compares separations between the estimated source locations from multilateration with source separations estimated from CWI. The latter estimates are from Equations 9 and 13, and an estimate of the bulk velocity of the medium (the same measured velocity used in multilateration) for each sample, and separations were obtained using only the top receiver (multilateration estimates require the use of all four receivers). For all three media, the multilateration-method estimates are relatively scattered, particularly for Tivoli Travertine and Copp-Crag Sandstone. CWI estimates of the relative source locations are more precise, and are more accurate up to approximately 0.2-0.4λ, where λ is the dominant wavelength. At larger separations cycle-skipping in the cross-correlation is likely to interfere with the signals that we seek in the maximum of the correlation function, causing estimates to tend to a constant value at larger source separations. We demonstrate in Section 3.5 below how relative locations of sources can be obtained using separation data from even only a single receiver, and how the working-range of source separations can be increased beyond 0.4λ.

3.3 Experimental Examples

In experimental rock physics, trends in velocity are often measured to model the response of seismic velocity to changes in external conditions (e.g., temperature, effec-

tive and differential stresses, fluid properties, etc.), conferring particular importance to the interpretation of dynamic changes. This is important for a range of geophysical scenarios on a larger scale, such as monitoring subsurface fluid reservoirs or changes in rock properties using time-lapse (4D) seismic methods. Here we show results of two laboratory experiments that impose changes in the external conditions of temperature and stress. In the first experiment illustrated in Figure 8a, a 10 cm^3 block of Halldale Sandstone was heated from room temperature to an external temperature of 54°C over one hour, and then left to relax to room temperature. In this experiment we do not aim for thermal equilibrium, because the CWI method does not require a constant medium velocity. The experiment varies temperature simply to induce a non-uniform change in velocity within the medium for comparison of CWI and conventional methods. A thermocouple was attached to an external face for continuous temperature monitoring, and two piezoelectric transducers (PZT) were attached on opposite faces of the sample for continuous ultrasonic surveys, which were undertaken during the cooling phase back down to room temperature. As the maximum temperature variation is relatively small ($\Delta 8$°C), we assume that the PZT response to temperature variation is negligible.

To measure P-wave velocity we use Glaser-type conical piezoelectric sensors sensitive to displacement normal to the sensor face (McLaskey & Glaser, 2012). These laboratory-standard, wide-band sensors are calibrated against theoretical displacement time history and have an almost flat displacement response spectrum in the 20 kHz to 1 MHz frequency band. This means that, in this frequency band, they are essentially displacement sensors and their voltage output is linearly proportional to the surface normal displacement. Aperture effects are reduced due to the relatively small 0.5 mm sensor contact area (which is even higher than the resolution used in Figure 3). We used an Itasca Image pulser-amplifier system with operating frequency range of 100 kHz to 1 MHz and pre-amp gain of 40 dB, which switches between all transducers in an ultrasonic array, allowing each to act as both a transmitter and a receiver. The amplitude of the pulse spike is 500 V with approximate signal rise time of 0.3 μs and total duration of 2.8 μs, the sampling period is 40 ns. The output recorded waveform at each receiver is a stack of received waveforms from 25 source pulses with a pulse repetition frequency of 20 kHz (as the pulse repetition is high, we assume no loss in phase resolution).

The change in velocity ($\Delta V/V$) for each temperature change (ΔT) were estimated using both the first-break method (manually picking the first extremum) and the CWI

stretching technique (plotted in Figure 9). There is a large amount of scatter in the $\Delta V/V$ estimates for the first break method, where there is no clear trend that can be resolved above the noise. In contrast, the $\Delta V/V$ estimates using CWI form a clear and coherent response to changes in temperature - a linear, negative correlation due to thermal contraction. This highlights the sensitivity of standard methods to noise, and CWI's ability to resolve small changes in spite of the presence of noise.

A second experiment was carried out, illustrated in Figure 8b, where a 38 mm diameter, 75 mm length core of a fine grained laminated carbonate was held at 45 MPa effective pressure, and a differential stress was applied with a strain rate of 10^{-5}s^{-1}, until a peak stress of 235 MPa. The stress loading history is plotted in Figure 11a, where pauses in loading are periods during which the permeability of the sample was measured. P wave velocity is estimated using the Glaser-type sensors described above. We measure S wave velocity using sensors with PZT sensitive to displacement tangential to the sensor face, with a central frequency of 700 kHz and a contact area of 20 mm^2. Example waveforms for this experiment are shown in Figure 10. The variation of velocity during the experiment is estimated using the standard first break method for estimating P and S wave velocities, and the CWI moving reference trace method (from Equations 1, 2 and 3) using the time window labeled in Figure 10a ($t1 = 0.35ms$, $t2 = 0.65ms$). In Figure 11a we see CWI provides a far clearer and more consistent response to external stress changes compared against the change in P wave velocity estimated using first-breaks, accurately mirroring the stepped stress program with far less scatter in the estimated $\Delta V/V$ values, most strikingly for the earlier stress steps. First-break S wave velocities exhibit a smoother response (less scatter), but also fail to mirror the stepped stress program. $\Delta V/V$ estimates from CWI approximately mark the average between changes in P and S wave velocities - we discuss the way in which CWI averages changes in P and S wave velocities in Section 4. The higher $\Delta V_P/V_P$ in estimates from the conventional method may also reflect the bias towards higher velocities, as the first arriving waves follow only the fastest ray path. As deformation occurs, compaction is localized to specific regions of the sample; if the fastest travel path samples such regions, the estimated change in velocity ($\Delta V_P/V_P$) would be larger using first-breaks than estimates using CWI which is more representative of the changing bulk properties of the sample.

As CWI uses a cross-correlation function, the method breaks down if there are very large changes in the medium due to wave paths being significantly altered and (if the

medium fractures) new scattering points being introduced. This means that a single reference trace is not appropriate for CWI in such deformation experiments where the rock structure is significantly deformed. This effect can be seen in Figure 11b, where different CWI algorithms are compared. The "double wavelet" method (Snieder et al., 2002) measures delay times ($\delta\tau$) for multiple time windows down the coda: these relate to the velocity perturbation by $\Delta V/V = -\delta\tau/t$. It is clear that at later stages in the experiment (after 1 hour), the estimates of $\Delta V/V$ using the double wavelet method with a fixed reference trace (dashed purple line) are heavily distorted due to the deformation occurring within the sample. The large amount of scatter exhibited by this method highlights the problem of large changes occurring in the medium. The stretching method, without implementing a moving reference trace (dashed red line), provides more consistent estimates of $\Delta V/V$ than the double wavelet method, estimating a consistent increase in velocity. At later stages in the experiment, these estimates of $\Delta V/V$ become more scattered and the mirroring of the stepped stress program becomes less clear. For both methods, implementing the moving reference trace method (Equation 3) limits estimates to small changes in velocity, for which CWI remains accurate, to obtain an overall estimate in $\Delta V/V$ that shows a much clearer stepped response. This suggests that the moving (or periodically updated) reference trace method can account for the more extreme changes that occur in the medium. There is no prescribed value for how frequently the reference trace should be updated (k in Equation 3) as it depends on the rate of deformation and the surveying frequency, except that it should be introduced before any changes produce a half-wavelength change in the waveform in the latest time window. However, the strengths of CWI lie in the ability to resolve small changes in velocity, therefore the step size k should remain small ($k = 5$ for results shown in Figure 11b, where surveys are taken every minute).

3.4 Joint Estimation of Source Separation and Velocity Change

Since CWI estimates of the bulk velocity change ($\Delta V/V$) and source separation (r) are derived from different information (the phase and the maximum value of correlation as shown in equations 2 and 9, respectively), estimates of each can be made independently when both effects occur simultaneously. This has significant experimental advantages, as fixed source and receiver locations might no longer be necessary for continuous velocity measurements, and in deformation experiments when acoustic emissions

might accompany bulk velocity changes these two effects could be analyzed independently - all using a single receiver.

We test the accuracy of these estimates using a series of finite-difference simulations taking a central source location and changing the location by up to 1.2λ and simultaneous velocity perturbations of up to 1%. Figures 12a and b show estimates of source separation (r) where no velocity perturbation occurs, and the reverse - changes in velocity when the source remains stationary. These represent the best possible estimates from CWI, as only one perturbation type occurs at a time. The additional errors associated with simultaneous perturbations of r and V are shown in Figures 12c and d. We see that estimates of source perturbation are barely affected by the presence of a velocity perturbation: the stretching method of CWI removes the effect of any velocity perturbation. However, estimates of velocity perturbation are far more sensitive to source location perturbations, giving errors of 0.5% for a source displacement of around one wavelength (a relatively large error given the accuracy otherwise expected from CWI). The additional error appears to stem from the effect of cycle skipping in the cross-correlation function when changes result in the alteration of travel times to on the order of half a wavelength.

These results also show that in the case of simultaneous perturbations of source location and velocity, source separation can be estimated much more accurately than estimates of the change in velocity. Therefore, we would expect that the 3D network of relative locations of acoustic emissions that occur during deformation can be estimated robustly using laboratory datasets even if velocity changes occur in the medium (Zhao & Curtis, 2019; Zhao et al., 2017). This is demonstrated in the following section.

3.5 Relocating relative source locations from inter-source distance

Using the inter-source distances or separations between many pairs of sources, it is possible to find the relative locations of a cluster of sources, provided that inter-source distances are within the working range of CWI . However as we see in Figure 7, CWI provides a slightly biased estimate of these separations. The relocation method solves for the relative location of a cluster of sources in a probabilistic framework within which it is possible to correct this bias to a significant extent (Robinson, Sambridge, Snieder, & Hauser, 2013; Zhao & Curtis, 2019; Zhao et al., 2017). For one pair of events, accord-

ing to Bayes' theorem

$$P(\tilde{\delta}_t|\tilde{\delta}_{CWI}) \propto P(\tilde{\delta}_{CWI}|\tilde{\delta}_t) \times P(\tilde{\delta}_t), \tag{15}$$

where the posterior probability $P(\tilde{\delta}_t|\tilde{\delta}_{CWI})$ is the probability of the true separation having value $\tilde{\delta}_t$ given that the estimated separation from CWI is $\tilde{\delta}_{CWI}$. This is proportional to the likelihood $P(\tilde{\delta}_{CWI}|\tilde{\delta}_t)$ of having observed $\tilde{\delta}_{CWI}$ in the case that the true separation is $\tilde{\delta}_t$, multiplied by the prior probability $P(\tilde{\delta}_t)$ which describes any available information about event locations known prior to the location process. The likelihood function $P(\tilde{\delta}_{CWI}|\tilde{\delta}_t)$ describes the bias in separations estimated by CWI, and can be approximated by a Gaussian probability density function whose mean and standard deviation are described by empirical functions proposed by Robinson et al. (2011). The tilde over parameters indicates that the separation quantities are used in normalized form - they are the true values divided by the wavelength of the dominant frequency recorded in the seismogram coda.

For multiple events, Equation 15 holds for each event pair. The separation estimated from CWI for a cluster of events can be incorporated into a joint posterior function by multiplying the formulae for all available event pairs, assuming that they are independent of one another (Robinson et al., 2013):

$$P(\boldsymbol{e}_1, \ldots, \boldsymbol{e}_n|\tilde{\delta}_{CWI}) = c\prod_{i=1}^{n} P(\boldsymbol{e}_i) \times \prod_{i=1}^{n-1}\prod_{j=i+1}^{n} P(\tilde{\delta}_{CWI,ij}|\boldsymbol{e}_i, \boldsymbol{e}_j), \tag{16}$$

where c is a constant, n is the number of events, $\boldsymbol{e}_i = (x_i, y_i, z_i)$ is the location of event i. Within the last term we use the locations of the ith and jth events ($\boldsymbol{e}_i$ and $\boldsymbol{e}_j$) from which we can calculate their separation $\delta_{t,ij} = ||\boldsymbol{e}_i - \boldsymbol{e}_j||_2$ (subscript 2 denotes the L-2 norm), and thus we implicitly include Equation 15. The most probable set of the event locations can be found where the joint posterior function attains its maximum. Therefore, the event locations can be estimated by solving an optimization problem. The optimization problem is converted to a minimization problem by taking the negative logarithm of Equation 16:

$$-ln[P(\boldsymbol{e}_1, \ldots, \boldsymbol{e}_n|\tilde{\delta}_{CWI})] = -ln[c] - \sum_{i=1}^{n} ln[P(\boldsymbol{e}_i)] - \sum_{i=1}^{n-1}\sum_{j=i+1}^{n} ln[P(\tilde{\delta}_{CWI,ij}|\boldsymbol{e}_i, \boldsymbol{e}_j)]. \tag{17}$$

A uniform prior $P(\boldsymbol{e}_i)$ is considered in this work, so the terms containing $ln[P(\boldsymbol{e}_i)]$ are constant, and the term $ln[c]$ can be ignored in the minimization problem. Thus, the objective function becomes:

$$L(\boldsymbol{e}_1, \ldots, \boldsymbol{e}_n) = -\sum_{i=1}^{n-1}\sum_{j=i+1}^{n} ln[P(\tilde{\delta})_{CWI,ij}|\boldsymbol{e}_i, \boldsymbol{e}_j)]. \tag{18}$$

This function can be minimized using a conjugate gradient algorithm (Press, Flannery, Teukolsky, & Vetterling, 1986).

We test this location method using the Tivoli Travertine model shown in Figure 2b, and source locations shown in Figure 13a, simulating a cluster of 80 acoustic emissions around a fracture plane. We divided the events into multiple sub-clusters with 20 overlapping event locations, where the maximum separations in each sub-cluster remained roughly within or just outside of the working range of CWI (approximately 0.5λ). The separation into sub-clusters can be achieved using only the pairwise separation estimates from CWI, by sorting pairs of events by estimated proximity, an optimal configuration of sub-clusters can be found so that all separation values are within 0.5λ. We therefore do not require knowledge of the true source locations for this step in the method.

For each sub-cluster, we solved for the relative event locations by minimizing Equation 18 using the publicly available CWI-relocation code package of Zhao and Curtis (2019), taking the CWI separation estimates as inputs. We conducted the location process five times with different randomly distributed initial event locations to ensure convergence to the global minimum of the objective function (Equation 17). The optimizations all converge to the same minimum to within trivial numerical differences. Receiver locations follow the same configuration as shown in Figure 5a. Since absolute event locations remain unknown in this method, we then rotate and translate the resulting sub-clusters to match locations of the overlapping sources. For comparison, we also performed the conventional method for locating sources, using manual phase-picking of first-break (first extremum) arrivals for multiple receivers, and multilateration (Equation 14) to estimate locations of sources. The results of multilateration and CWI relocations are shown in Figure 13b and c, respectively in order to cluster events.

We note immediately that the cluster of events from multilateration in Figure 13b is rotated by 45° relative to the true locations due to velocity heterogeneity in the sample. Since CWI only provides *relative* locations, the cluster of CWI location in panel c has been rotated to best match the results in panel b for fair comparison. The spatial area of events in panel c appears to be more rectangular (like the true shape of the area in panel a) than the area in panel b. Nevertheless, it is difficult to decide which of Figure 13b and c is better from these plots alone so Figure 14 shows the source separation values of these two clusters as a function of true source separation normalized by wave-

length λ. This highlights the improvement of accuracy and precision offered by the CWI source relocation procedure. It is also important to note from Figure 14 that using the sub-cluster matching methods, the overall source network size can extend well beyond the usual working range of CWI and the source-separation bias can be largely corrected, providing there are overlapping sources between sub-clusters.

3.6 Sensitivity to Noise

In order to test the ability of CWI to estimate changes in velocity and in source or receiver location when using noise-contaminated data, we generate a synthetic record of noise which is superimposed onto the numerically simulated signals used above. We generate realistic noise as follows: 1) measure a long noise record in the Edinburgh rock physics laboratory, and process it to create a record of de-meaned and de-trended seismic noise. 2) Take the Fourier Transform of the noise recording, and smooth the record in the Fourier domain to ensure there are no spectral gaps (frequency bands without noise). 3) Convolve the resulting spectrum with a sample of random Gaussian white noise so that generated noise is uncorrelated and transform back into the time domain. The resulting signal is therefore a randomly generated recording of realistic noise, which can be superimposed on the effectively noiseless waveforms generated from synthetic finite difference simulations. The signal-to-noise ratio (SNR) is calculated as $SNR = P_{signal}/P_{noise}$, where P is the average power. We add the noise at different SNR values to a range of numerically simulated signals where the velocity has been perturbed from 0 - 10% and where the source location is perturbed by 0.01λ. Estimates of the range of velocity perturbations are calculated using CWI, as well as by using conventional phase-picking methods for each level of noise contamination. For the phase-picking of first arrivals, we use automatic methods (STA/LTA method described by Earle and Shearer (1994)) as well as manually picking the time of the first extremum. These estimates are shown for low noise contamination (SNR=8) and high noise contamination (SNR=0.43) in Figure 15. The total error at each SNR value, calculated as the sum of residuals of each estimate to the true $\Delta V/V$ value is shown in Figure 16a. We find that at high SNR values, all estimates for $\Delta V/V$ show a clear response to the increasing velocity perturbation, though CWI estimates are over an order of magnitude more accurate. At low SNR values, conventional methods based on phase-picking show much more scatter in the estimates of $\Delta V/V$, whereas CWI is much more precise, and is mostly unaffected by the increased

contamination of noise. The first-break arrivals are of lower amplitude and are therefore more susceptible to contamination by noise, whereas CWI uses the entire signal, including many more data points, and is therefore more robust in the presence of noise.

For estimation of source separation in the presence of noise (see Figure 16b), the absolute locations of sources within a small cluster were estimated by multilateration by assuming a constant, isotropic P-wave velocity. However, because CWI does not provide absolute source locations but instead gives the separation between two sources, r, we estimate the separation r between pairs of absolute locations from multilateration for comparison. We compare this to the r estimate from CWI for each pair of sources, and plot the sum of individual residuals for all source pairs and for each method in Figure 16. We find that at all SNR values CWI outperforms multilateration, particularly at high levels of noise. These results show that CWI is a more robust way to characterize changes in a medium's velocity or in relative source locations in the presence of noise. Since no phase picking is necessary for CWI, this also means that less pre-processing of data is required before analysis. CWI requires the computation of many cross-correlation functions, therefore can be computationally expensive compared to conventional methods, however we have demonstrated this method to offer significant improvements in both accuracy and precision.

4 Estimating Individual P and S Wave Contributions to CWI Observations

The results from CWI only provide a measure of the change in velocity and not the absolute velocity itself. In itself this is not of particular concern since in many real-world problems, such as those relating to the interpretation of 4D seismic data, we seek to characterize the dynamic dependence of velocity on changes in external properties (Landrø & Stammeijer, 2004). However, ΔV/V estimates from CWI are more difficult to interpret than separate estimates of V_P and V_S that are obtainable from conventional methods. Given an estimate of density, estimates of V_P and V_S allow bulk and shear moduli to be estimated, and these are parameters that appear in the majority of rock physics models. CWI estimates of $\Delta V/V$ reflect a combination of P-wave and S-wave velocity information due to the multiple phase conversions that occur during wave propagation.

To aid the interpretation of CWI $\Delta V/V$ estimates, consider the scattering model presented by Snieder (2002) which assumes isotropic point scatterers inside a constant

velocity medium. This model represents P and S wave states as many packets of energy traveling with velocities V_P and V_S. A packet can only be in one state at a given time. When a packet of P energy travels distance a (the average distance between scatterers), it has a probability p_{PS} of converting to an S state; likewise a packet of S energy has a probability p_{SP} of converting to the P state. Over a time interval dt, a packet in the P state encounters $V_P dt/a$ scatterers, meaning that in a system with N_P and N_S packets in the P and S states, the reduction in P packets due to $P-to-S$ conversions is given by $-2p_{PS}N_P V_P dt/a$ and the increase due to $S-to-P$ conversions is given by $p_{SP}N_S V_S dt/a$. Following from this, Snieder (2002) derives the following system of differential equations:

$$\dot{N}_P = \frac{1}{a}(p_{SP}V_S N_S - 2p_{PS}V_P N_P), \tag{19}$$

$$\dot{N}_S = \frac{1}{a}(2p_{PS}V_P N_P - p_{SP}V_S N_S), \tag{20}$$

where the dot over N_P and N_S on the left side indicates a rate of change over time. Now consider a receiver not co-located with the source, at which the time of first arriving energy in the signal is comprised of only P state energy. After this time the proportions of P and S wave energy can be calculated using equations 19 and 20, and therefore so can the proportions of *changes* in P-wave velocity ($\Delta V_P/V_P$) and S-wave velocity ($\Delta V_S/V_S$). The way in which these proportions of $\Delta V/V$ vary as a function of time is shown in Figure 17. For time values to be independent of the scattering properties of the medium, time is normalized by the travel time of one mean free path ($\tau_P = l_P/V_P$), where the mean free path l_P is defined as $l_P = a/(2P_{PS})$. In practice, the mean free path of a scattering medium can be estimated from the apparent attenuation of energy in recorded signals (Anugonda, Wiehn, & Turner, 2001; Obermann, Planès, Larose, Sens-Schönfelder, & Campillo, 2013). Figure 17 shows how the proportions of $\Delta V_P/V_P$ and $\Delta V_S/V_S$ change depend on the V_P/V_S ratio. At equilibrium, the proportion of $\Delta V_S/V_S$ is higher than $\Delta V_P/V_P$, even at very low V_P/V_S ratios (Figure 17a), explained by S having two states (S_1 and S_2, which represent the two polarizations of S waves) where P only has one state. As V_P/V_S increases, so does the proportion of $\Delta V_S/V_S$ at equilibrium, as energy in S waves are traveling more slowly than P waves and so spend more time in that state before encountering scatterers.

We can use this model to estimate the independent changes of P and S wave velocity. Define $q(t,\gamma)$ to be the relative contribution of $\Delta V_S/V_S$ (the red curves in Fig-

ure 17), where $\gamma = V_P/V_S$. The function q depends on time t and on the V_P/V_S ratio γ, and the relative contribution of $\Delta V_P/V_P$ (blue curves in Figure 17) is $1-q(t,\gamma)$. If P and S wave velocities change by different amounts, the measured change in velocity from CWI $[\Delta V/V]_{CWI}$ therefore varies as a function of time along the coda by

$$\left[\frac{\Delta V}{V}\right]_{CWI}(t) = [1-q(t,\gamma)]\left[\frac{\Delta V_P}{V_P}\right] + q(t,\gamma)\left[\frac{\Delta V_S}{V_S}\right]. \quad (21)$$

For a single time window, this equation has two unknown parameters, $\Delta V_P/V_P$ and $\Delta V_S/V_S$; the value of $[\Delta V/V]_{CWI}$ can be measured and $q(t,\gamma)$ is known (from Figure 17). Measuring $[\Delta V/V]_{CWI}$ in multiple time windows along the coda therefore gives multiple equations, the same number as there are time windows. Quantities $\Delta V_P/V_P$ and $\Delta V_S/V_S$ can be estimated using an ordinary least squares inversion approach to solve the system: $d = Am$, where d is a matrix of measured values of $[\Delta V/V]_{CWI}$ for each time window, and A is matrix of $(1-q)$ and q values expected at each time window for a given V_P/V_S ratio γ. The resulting vector m contains estimates of $\Delta V_P/V_P$ and $\Delta V_S/V_S$ for a given V_P/V_S ratio, and we denote these estimates by $[\Delta\widehat{V_P/V_P}]_\gamma$ and $[\Delta\widehat{V_S/V_S}]_\gamma$, respectively. Clearly, in order to estimate the changes of V_P and V_S independently we need to be able to estimate $\gamma = V_P/V_S$.

One way to estimate γ would be to use the conventional experimental method to estimate V_P and V_S, but as we have shown herein, those methods are less accurate than CWI for subtle changes in the medium so it is desirable to find alternative methods. As Figure 17 shows, values for $q(t)$ can vary significantly depending on the V_P/V_S ratio. We can therefore refine estimates of $\Delta V_P/V_P$ and $\Delta V_S/V_S$ within a probabilistic framework, using a statistical distribution of V_P/V_S ratios rather than a single value. We illustrate this by compiling a database of 296 measured V_P/V_S ratios for dry carbonates combining data from Bakhorji (2010), Fournier et al. (2011) and Verwer, Braaksma, and Kenter (2008). This data is selected purely as a demonstration of how such a distribution could be used; in practice such a distribution should be refined as the database contains samples with a large range porosities, pore structures and measurements at different confining pressures, only some of which would be relevant for our rock type or volume of interest. From the carbonate database, we create a prior distribution of V_P/V_S ratios γ for carbonate rocks $P_{carb}(\gamma)$, shown in Figure 18a. In order to test the method we also calculate synthetic $[\Delta V/V]_{CWI}$ data using Equation 21 with a change in P wave velocity of 1%, a change in S wave velocity of 0.5%, and a V_P/V_S ratio equal to $\sqrt{3}$ ($\Delta V_P/V_P = 1\%$, $\Delta V_S/V_S = 0.5\%$, $\gamma = \sqrt{3}$), which gives $[\Delta V/V]_{CWI}$ as a function of time (Fig-

ure 18b). The method then proceeds as follows: using the generated $[\Delta V/V]_{CWI}$ data and the known values for $q(t,\gamma)$, we invert for $[\Delta\widehat{V_P/V_P}]_\gamma$ and $[\Delta\widehat{V_S/V_S}]_\gamma$ for a range of values of V_P/V_S ratios (γ), shown in Figure 18c. However, given the knowledge that the sample is a carbonate, not all of these values are equally likely. We should therefore weight this set of solutions by the probability P that each V_P/V_S ratio is the one in our sample - represented by the probability distribution in Figure 18a. Thus we can generate probability density functions for estimates of $\Delta V_P/V_P$ and $\Delta V_S/V_S$ with the following equations:

$$P\left(\frac{\Delta V_P}{V_P}\right) = \int_{\gamma\in R_\gamma} \delta\left(\frac{\Delta V_P}{V_P} - \left[\frac{\widehat{\Delta V_P}}{V_P}\right]_\gamma\right) \cdot P_{carb}(\gamma)d\gamma, \tag{22}$$

$$P\left(\frac{\Delta V_S}{V_S}\right) = \int_{\gamma\in R_\gamma} \delta\left(\frac{\Delta V_S}{V_S} - \left[\frac{\widehat{\Delta V_S}}{V_S}\right]_\gamma\right) \cdot P_{carb}(\gamma)d\gamma, \tag{23}$$

where R_γ is the prior range of V_P/V_S ratios γ. In the case where $\Delta V_P/V_P = 1\%$ and $\Delta V_S/V_S = 0.5\%$, the resulting probability distributions for changes in P and S wave velocities are shown in Figures 18d and e. For both changes in P and S wave velocity, the method accurately estimates the velocity change. The probability distribution change in P wave velocity $\Delta V_P/V_P$ is relatively precise, with almost all estimates within $\pm 0.01\%$ of the true value for velocity change. The distribution of change in S wave velocity has a wider spread, though still significant precision when compared to standard methods, with the majority of estimates within $\pm 0.03\%$ of the true velocity change. From this we can see that it is possible to estimate independent changes in P and S wave velocity using CWI given the statistical distribution of V_P/V_S ratios for a rock type, and with the assumption of isotropic scattering.

5 Discussion

We have demonstrated that under the conditions examined here, using Coda Wave Interferometry for experimental applications can provide significant improvements over conventional methods, particularly in the accuracy and precision of estimates of changes in velocity and source location.

An important aid in the interpretation of CWI estimates is an understanding of the type of spatial average of material parameters that is implicit in CWI estimates. To examine this, a numerical experiment is conducted using the μCT derived velocity and density models of the Tivoli Travertine (Figure 2a). The fluid velocity (initially 1500 m/s) is perturbed by a range of values (up to a +10% perturbation), and CWI is used to es-

timate the velocity perturbation of the bulk medium. As the exact amount of calcite and pore fluid phases are known, as well as their properties, the change in the average properties of the medium can be calculated with various averaging methods. Here we use the Voigt upper bound M_V (Voigt, 1928):

$$M_V = \sum_{i=1}^{N} f_i M_i, \tag{24}$$

and the Reuss lower bound M_R (Reuss, 1929):

$$\frac{1}{M_R} = \sum_{i=1}^{N} \frac{f_i}{M_i}, \tag{25}$$

where f_i is the volume fraction of the ith phase and M_i is the elastic modulus of the ith phase, M can represent the bulk modulus K or the shear modulus μ. We also use the Voigt-Reuss-Hill average (Hill, 1952) $[M_V+M_R]/2$, and the Hashin-Shtrikman bounds (Hashin & Shtrikman, 1963):

$$K^{HS\pm} = K_1 + \frac{f_2}{(K_2 - K_1)^{-1} + f_1(K_1 + \frac{4}{3}\mu_1)^{-1}} \tag{26}$$

$$\mu^{HS\pm} = \mu_1 + \frac{f_2}{(\mu_2 - \mu_1)^{-1} + 2f_1(K_1 + 2\mu_1)/[5\mu_1(K_1 + \frac{4}{3}\mu_1)]} \tag{27}$$

where the subscripts 1 and 2 refer to the two phases in the medium and the upper and lower bounds are computed by interchanging which phase is termed 1 and 2 (Mavko et al., 2009). The Reuss lower bound is equal to the Hashin-Shtrikman lower bound when one of the constituents is a liquid with zero shear modulus. We calculate the various averages taking the bulk and shear moduli to be $K_{calcite} = 129.53$ GPa, $\mu_{calcite}$=35 GPa, $K_{fluid} = 2.25$ GPa, and $\mu_{fluid} = 0$. A comparison of how these different measures spatially average the medium is shown in Figure 19. Of the different methods used, the Reuss lower bound shows the closest estimate to the measured first break velocity in Figure 19a, and of the CWI estimates for velocity change in Figure 19b.

The use of CWI estimates in current rock physics protocols is therefore possible because the appropriate information required for many rock physics models is available: the relative proportions of P and S wave velocity changes (Figure 18) is obtainable given prior knowledge of V_P/V_S ratios of the medium (based for instance on rock type as in the example above), and we can infer how CWI averages the bulk velocity change properties of a medium spatially (Figure 19).

The method of CWI used here (Equation 1) is known as trace stretching and has some underlying assumptions and limitations. Namely it assumes that the velocity perturbation is uniform across the entire medium so that all arriving energy is perturbed

at the same temporal rate, and therefore the trace is stretched linearly in time along the seismogram. Mikesell, Malcolm, Yang, and Haney (2015) provides a comparison of different methods to estimate changes in velocity for CWI, and suggests a dynamic time warping method as a solution for inhomogeneous velocity perturbations.

As we have shown, CWI is able to resolve both changes in velocity and changes in source and/or receiver locations, allowing for the estimation of relative source locations. However CWI is also able to resolve another type of perturbation on which we have not focused: the average displacement of all scatterers, δ, illustrated in Figure 1c (Snieder et al., 2002). This value is related to the variance of travel time perturbations by

$$\sigma_\tau^2 = \frac{2\delta^2 t}{v l_\star}, \tag{28}$$

where $l_\star$ is the transport mean free path. It would be interesting to monitor how this parameter varies during experimental rock physics and geomechanics experiments. For example, it may be possible to monitor changes in the average distance between scattering points, which could act as a proxy measure for inter-pore distance, itself a strong control on the time of failure (Vasseur et al., 2017). During the confining or varying of fluid pressure in an isotropic sample, scattering points would be displaced in all directions, and this displacement might be measured by CWI. Similar effects occur at reservoir scale where fluid injection or extraction can lead to seismically observable volumetric expansion of the reservoir. We leave this for future research.

Most of the numerical experiments presented here assume a high frequency regime as well as point sources and receivers. In one experiment where we lowered the frequency of by more than an order of magnitude we did not observe any significant differences in the method. Nevertheless, another area for the development of the CWI method is to investigate the dependence of CWI results over a broad range of frequencies, and using much larger aperture transducers such as those modelled by Li et al. (2018). We leave this for future research.

6 Conclusion

Conventional first-break methods based on manual phase-picking provide an estimate of seismic velocity that is not representative of the bulk medium in a high frequency regime with point sources and point receivers. Such estimates of seismic velocity, changes in velocity, and source location are highly variable even for a single sample,

and depend on the specific source/receiver path of the first arriving wave. They are therefore inadequate for characterizing the bulk properties of a rock sample, particularly those with complicated pore structures approximately similar size to the wavelength of the interrogating waves. By contrast, Coda Wave Interferometry is an effective method for countering these problems because coda waves sample the entire medium, and sample the same regions multiple times. CWI is shown to provide an increase in precision by an order of magnitude in the absence of noise, and to be a robust and accurate method for estimating both bulk velocity changes and perturbations of the source or receiver locations when compared with standard methods in both synthetic digital rock physics and laboratory experimental data. When noise is present, CWI remains far more accurate than conventional methods, even at very low signal-to-noise ratios. Additionally, when velocity and source/receiver location perturbations occur simultaneously CWI can still estimate velocity and source separation under some conditions: source separation estimates are mostly unaffected by the velocity perturbation, but velocity change estimates are much more sensitive and become inaccurate in the presence of larger source perturbations, possibly due to cycle-skipping. Using source separation estimates, relative locations of a cluster of sources can be estimated using a single receiver, and show higher precision and accuracy compared to conventional methods. CWI estimates a combination of changes in both P and S wave velocities, and we demonstrate a model for the equilibration of the contributions from P and S waves as a function of time, and show how the independent changes in P and S wave velocity can be measured, given probabilistic *a priori* information about the V_P/V_S ratio. Overall these results show significant potential for the use of CWI to characterize changes in porous media undergoing changes in effective stress and strain, and in temperature.

Acknowledgments

The authors would like to thank Petrobras and Shell for their sponsorship of the International Centre for Carbonate Reservoirs (ICCR), and for permission to publish this work from the 4DRP project. We are also grateful to Ian Butler, Florian Fussies, Phil Cilli, Angus Lomas, and Roseanne Clement for their helpful scientific input and comments. We also acknowledge the thoughtful and constructive reviews of Editor Douglas Schmitt and two anonymous reviewers. The MATLAB code package is available at:

`https://github.com/JonathanSingh/cwi_codes/`

The code package of Zhao and Curtis (2019) is available at:

`https://www.geos.ed.ac.uk/eip/codes.html`

References

Anugonda, P., Wiehn, J. S., & Turner, J. A. (2001). Diffusion of ultrasound in concrete. *Ultrasonics*, *39*(6), 429–435.

Arts, R., Eiken, O., Chadwick, A., Zweigel, P., Van der Meer, L., & Zinszner, B. (2004). Monitoring of CO2 injected at Sleipner using time-lapse seismic data. *Energy*, *29*(9-10), 1383–1392.

Bakhorji, A. M. (2010). *Laboratory measurements of static and dynamic elastic properties in carbonate* (Unpublished doctoral dissertation). PhD Thesis, University of Alberta, Edmonton, Alberta , Canada.

Bass, J. D. (1995). Elasticity of minerals, glasses, and melts. *Mineral physics & crystallography: a handbook of physical constants*, *2*, 45–63.

Boschetti, F., Dentith, M. D., & List, R. D. (1996). A fractal-based algorithm for detecting first arrivals on seismic traces. *Geophysics*, *61*(4), 1095–1102.

Brillouin, L. (1960). *Wave propagation and group velocity*. Academic Press.

Brown, L. T. (2002). *Integration of rock physics and reservoir simulation for the interpretation of time-lapse seismic data at Weyburn field, Saskatchewan* (Unpublished doctoral dissertation). Colorado School of Mines. Arthur Lakes Library.

Christensen, N. I. (1966). Shear wave velocities in metamorphic rocks at pressures to 10 kilobars. *Journal of Geophysical Research*, *71*(14), 3549–3556.

Earle, P. S., & Shearer, P. M. (1994). Characterization of global seismograms using an automatic-picking algorithm. *Bulletin of the Seismological Society of America*, *84*(2), 366–376.

Ervin, C. P., McGinnis, L., Otis, R., & Hall, M. (1983). Automated analysis of marine refraction data: A computer algorithm. *Geophysics*, *48*(5), 582–589.

Fournier, F., Leonide, P., Biscarrat, K., Gallois, A., Borgomano, J., & Foubert, A. (2011). Elastic properties of microporous cemented grainstones. *Geophysics*, *76*(6), E211–E226.

Grêt, A., Snieder, R., & Özbay, U. (2006). Monitoring in situ stress changes in a mining environment with coda wave interferometry. *Geophysical Journal Inter-*

national, *167*(2), 504–508.

Guilbot, J., & Smith, B. (2002). 4-D constrained depth conversion for reservoir compaction estimation: Application to Ekofisk field. *The Leading Edge*, *21*(3), 302–308.

Hashin, Z., & Shtrikman, S. (1963). A variational approach to the theory of the elastic behaviour of multiphase materials. *Journal of the Mechanics and Physics of Solids*, *11*(2), 127–140.

Hatherly, P. (1982). A computer method for determining seismic first arrival times. *Geophysics*, *47*(10), 1431–1436.

Herwanger, J. V., & Horne, S. A. (2009). Linking reservoir geomechanics and time-lapse seismics: Predicting anisotropic velocity changes and seismic attributes. *Geophysics*, *74*(4), W13–W33.

Hill, R. (1952). The elastic behaviour of a crystalline aggregate. *Proceedings of the Physical Society. Section A*, *65*(5), 349.

Hornby, B. E. (1998). Experimental laboratory determination of the dynamic elastic properties of wet, drained shales. *Journal of Geophysical Research: Solid Earth*, *103*(B12), 29945–29964.

James, S., Knox, H., Abbott, R., & Screaton, E. (2017). Improved moving window cross-spectral analysis for resolving large temporal seismic velocity changes in permafrost. *Geophysical Research Letters*, *44*(9), 4018–4026.

Landrø, M., & Stammeijer, J. (2004). Quantitative estimation of compaction and velocity changes using 4D impedance and traveltime changes. *Geophysics*, *69*(4), 949–957.

Larose, E., & Hall, S. (2009). Monitoring stress related velocity variation in concrete with a 2× 10- 5 relative resolution using diffuse ultrasound. *The Journal of the Acoustical Society of America*, *125*(4), 1853–1856.

Li, W., Schmitt, D. R., Zou, C., & Chen, X. (2018). A program to calculate pulse transmission responses through transversely isotropic media. *Computers & geosciences*, *114*, 59–72.

Lobkis, O. I., & Weaver, R. L. (2001). On the emergence of the Greens function in the correlations of a diffuse field. *The Journal of the Acoustical Society of America*, *110*(6), 3011–3017.

Lockner, D. (1993). The role of acoustic emission in the study of rock fracture. *In-*

ternational Journal of Rock Mechanics and Mining Sciences & Geomechanics Abstracts, *30*(7), 883–899.

Lockner, D., Byerlee, J., Kuksenko, V., Ponomarev, A., & Sidorin, A. (1992). Observations of quasistatic fault growth from acoustic emissions. *International Geophysics*, *51*, 3–31.

Madonna, C., Almqvist, B. S., & Saenger, E. H. (2012). Digital rock physics: numerical prediction of pressure-dependent ultrasonic velocities using micro-CT imaging. *Geophysical Journal International*, *189*(3), 1475–1482.

Margrave, G. F. (2007). Methods of seismic data processing. *Geophysics*, *557*, 657.

Mason, W. P., & McSkimin, H. (1947). Attenuation and scattering of high frequency sound waves in metals and glasses. *The Journal of the Acoustical Society of America*, *19*(3), 464–473.

Mavko, G., Mukerji, T., & Dvorkin, J. (2009). *The rock physics handbook: Tools for seismic analysis of porous media*. Cambridge university press.

McLaskey, G. C., & Glaser, S. D. (2012). Acoustic emission sensor calibration for absolute source measurements. *Journal of Nondestructive Evaluation*, *31*(2), 157–168.

Mikesell, T. D., Malcolm, A. E., Yang, D., & Haney, M. M. (2015). A comparison of methods to estimate seismic phase delays: Numerical examples for coda wave interferometry. *Geophysical Journal International*, *202*(1), 347–360.

Moczo, P., Robertsson, J. O., & Eisner, L. (2007). The finite-difference time-domain method for modeling of seismic wave propagation. *Advances in Geophysics*, *48*, 421–516.

Molyneux, J. B., & Schmitt, D. R. (1999). First-break timing: Arrival onset times by direct correlation. *Geophysics*, *64*(5), 1492–1501.

Molyneux, J. B., & Schmitt, D. R. (2000). Compressional-wave velocities in attenuating media: A laboratory physical model study. *Geophysics*, *65*(4), 1162–1167.

Mordret, A., Mikesell, T. D., Harig, C., Lipovsky, B. P., & Prieto, G. A. (2016). Monitoring southwest Greenlands ice sheet melt with ambient seismic noise. *Science advances*, *2*(5), e1501538.

Obermann, A., Planès, T., Larose, E., Sens-Schönfelder, C., & Campillo, M. (2013). Depth sensitivity of seismic coda waves to velocity perturbations in an elastic

heterogeneous medium. *Geophysical Journal International*, *194*(1), 372–382.

Peraldi, R., & Clement, A. (1972). Digital processing of refraction data study of first arrivals. *Geophysical Prospecting*, *20*(3), 529–548.

Planès, T., & Larose, E. (2013). A review of ultrasonic coda wave interferometry in concrete. *Cement and Concrete Research*, *53*, 248–255.

Press, W. H., Flannery, B. P., Teukolsky, S. A., & Vetterling, W. T. (1986). *Numerical recipes: The art of scientific computing*. Cambridge University Press.

Pyrak-Nolte, L. J., Myer, L. R., & Cook, N. G. (1990). Transmission of seismic waves across single natural fractures. *Journal of Geophysical Research: Solid Earth*, *95*(B6), 8617–8638.

Reuss, A. (1929). Berechnung der fließgrenze von mischkristallen auf grund der plastizitätsbedingung für einkristalle. *ZAMM-Journal of Applied Mathematics and Mechanics/Zeitschrift für Angewandte Mathematik und Mechanik*, *9*(1), 49–58.

Robinson, D., Sambridge, M., & Snieder, R. (2011). A probabilistic approach for estimating the separation between a pair of earthquakes directly from their coda waves. *Journal of Geophysical Research*, *116*, B04309. doi: 10.1029/2010JB007745

Robinson, D., Snieder, R., & Sambridge, M. (2007). Using coda wave interferometry for estimating the variation in source mechanism between double couple events. *Journal of Geophysical Research: Solid Earth*, *112*(B12), B12302.

Robinson, D. J., Sambridge, M., Snieder, R., & Hauser, J. (2013). Relocating a cluster of earthquakes using a single seismic station. *Bulletin of the Seismological Society of America*, *103*(6), 3057–3072.

Saenger, E. H., & Bohlen, T. (2004). Finite-difference modeling of viscoelastic and anisotropic wave propagation using the rotated staggered grid. *Geophysics*, *69*(2), 583–591.

Saenger, E. H., Madonna, C., Osorno, M., Uribe, D., & Steeb, H. (2014). Digital carbonate rock physics. In *Seg technical program expanded abstracts 2014* (pp. 2915–2919). Society of Exploration Geophysicists.

Sams, M., Neep, J., Worthington, M., & King, M. (1997). The measurement of velocity dispersion and frequency-dependent intrinsic attenuation in sedimentary rocks. *Geophysics*, *62*(5), 1456–1464.

Sato, H., Fehler, M. C., & Maeda, T. (2012). *Seismic wave propagation and scattering in the heterogeneous earth* (Vol. 484). Springer.

Saxena, N., & Mavko, G. (2016). Estimating elastic moduli of rocks from thin sections: Digital rock study of 3D properties from 2D images. *Computers & Geosciences*, *88*, 9–21.

Sayers, C., & Kachanov, M. (1995). Microcrack-induced elastic wave anisotropy of brittle rocks. *Journal of Geophysical Research: Solid Earth*, *100*(B3), 4149–4156.

Sens-Schönfelder, C., & Wegler, U. (2006). Passive image interferometry and seasonal variations of seismic velocities at Merapi Volcano, Indonesia. *Geophysical research letters*, *33*(21), L21302.

Snieder, R. (2002). Coda wave interferometry and the equilibration of energy in elastic media. *Physical review E*, *66*(4), 046615.

Snieder, R. (2006). The theory of coda wave interferometry. *Pure and Applied Geophysics*, *163*(2-3), 455–473.

Snieder, R., Grêt, A., Douma, H., & Scales, J. (2002). Coda wave interferometry for estimating nonlinear behavior in seismic velocity. *Science*, *295*(5563), 2253–2255.

Snieder, R., & Vrijlandt, M. (2005). Constraining the source separation with coda wave interferometry: Theory and application to earthquake doublets in the Hayward fault, California. *Journal of Geophysical Research: Solid Earth*, *110*(B4).

Stork, A. L., Allmark, C., Curtis, A., Kendall, J.-M., & White, D. J. (2018). Assessing the potential to use repeated ambient noise seismic tomography to detect CO2 leaks: Application to the Aquistore storage site. *International Journal of Greenhouse Gas Control*, *71*, 20–35.

Toksöz, M., Johnston, D. H., & Timur, A. (1979). Attenuation of seismic waves in dry and saturated rocks: I. laboratory measurements. *Geophysics*, *44*(4), 681–690.

Vasseur, J., Wadsworth, F. B., Heap, M. J., Main, I. G., Lavallée, Y., & Dingwell, D. B. (2017). Does an inter-flaw length control the accuracy of rupture forecasting in geological materials? *Earth and Planetary Science Letters*, *475*, 181–189.

Verwer, K., Braaksma, H., & Kenter, J. A. (2008). Acoustic properties of carbonates: Effects of rock texture and implications for fluid substitution. *Geophysics*, *73*(2), B51–B65.

Vlastos, S., Liu, E., Main, I., Schoenberg, M., Narteau, C., Li, X., & Maillot, B. (2006). Dual simulations of fluid flow and seismic wave propagation in a fractured network: effects of pore pressure on seismic signature. *Geophysical Journal International*, *166*(2), 825–838.

Vlastos, S., Liu, E., Main, I. G., & Narteau, C. (2007). Numerical simulation of wave propagation in 2-D fractured media: scattering attenuation at different stages of the growth of a fracture population. *Geophysical Journal International*, *171*(2), 865–880.

Voigt, W. (1928). *Lehrbuch der kristallphysik* (Vol. 962). Teubner Leipzig.

Wang, Z. (2001). Fundamentals of seismic rock physics. *Geophysics*, *66*(2), 398–412.

Weaver, R. L., & Lobkis, O. I. (2001). Ultrasonics without a source: Thermal fluctuation correlations at MHz frequencies. *Physical Review Letters*, *87*(13), 134301.

Zhao, Y., & Curtis, A. (2019). Relative source location using coda wave interferometry: method, code package, and application to mining induced earthquakes. *Geophysics*, *84*(3), 1–58.

Zhao, Y., Curtis, A., & Baptie, B. (2017). Locating microseismic sources with a single seismometer channel using coda wave interferometry. *Geophysics*, *82*(3), A19–A24.

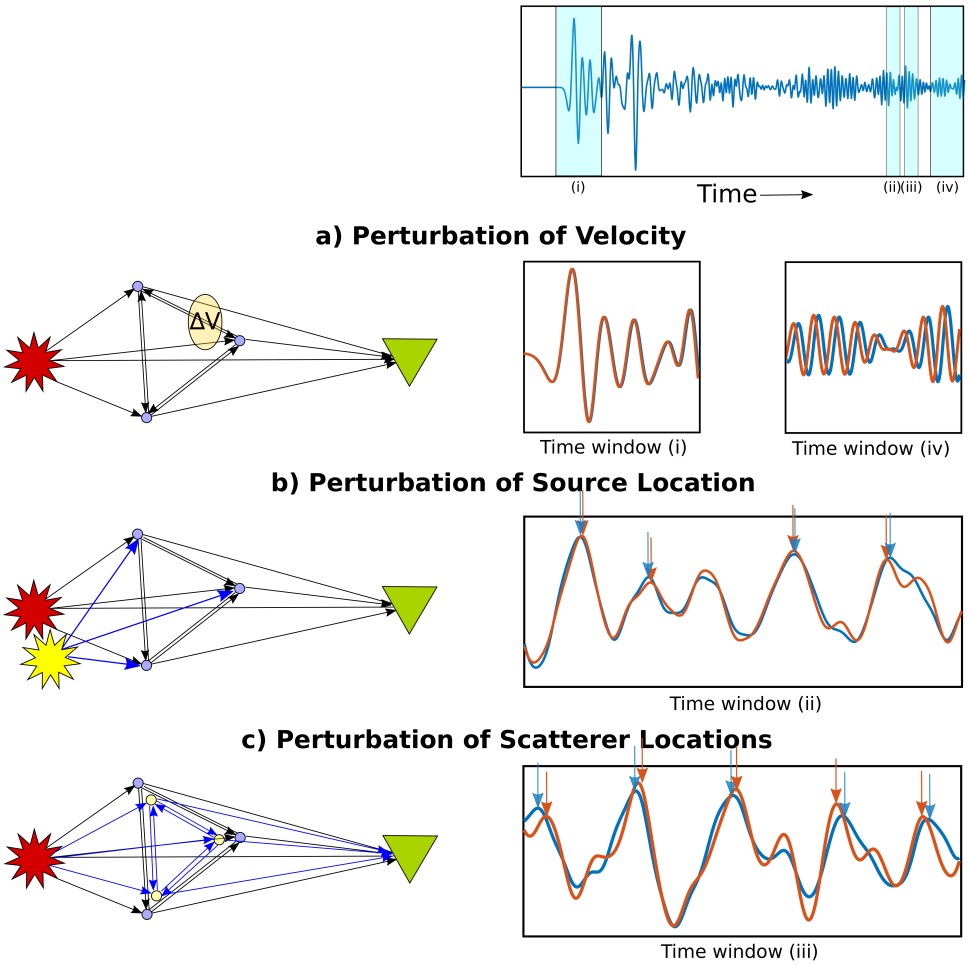

Figure 1. Illustrations of different perturbation types and their effects on coda waves. The cartoons (left) represent a scattering medium, with a source (star), receiver (triangle), and point scatterers (circles). Ray paths between the source and receiver, including multiple reverberations, are represented as black arrows. A velocity perturbation (a) is represented as a yellow ellipse, which has a velocity different to the background medium. New ray paths that are introduced due to changes in source location (b) and scatterer locations (c) are represented as blue arrows. Example recorded signals (right) at a range of time windows (i-iv) are shown before and after each perturbation takes place (blue and red, respectively). Differences in travel times of arriving energy for b) and c) are highlighted by vertical arrows.

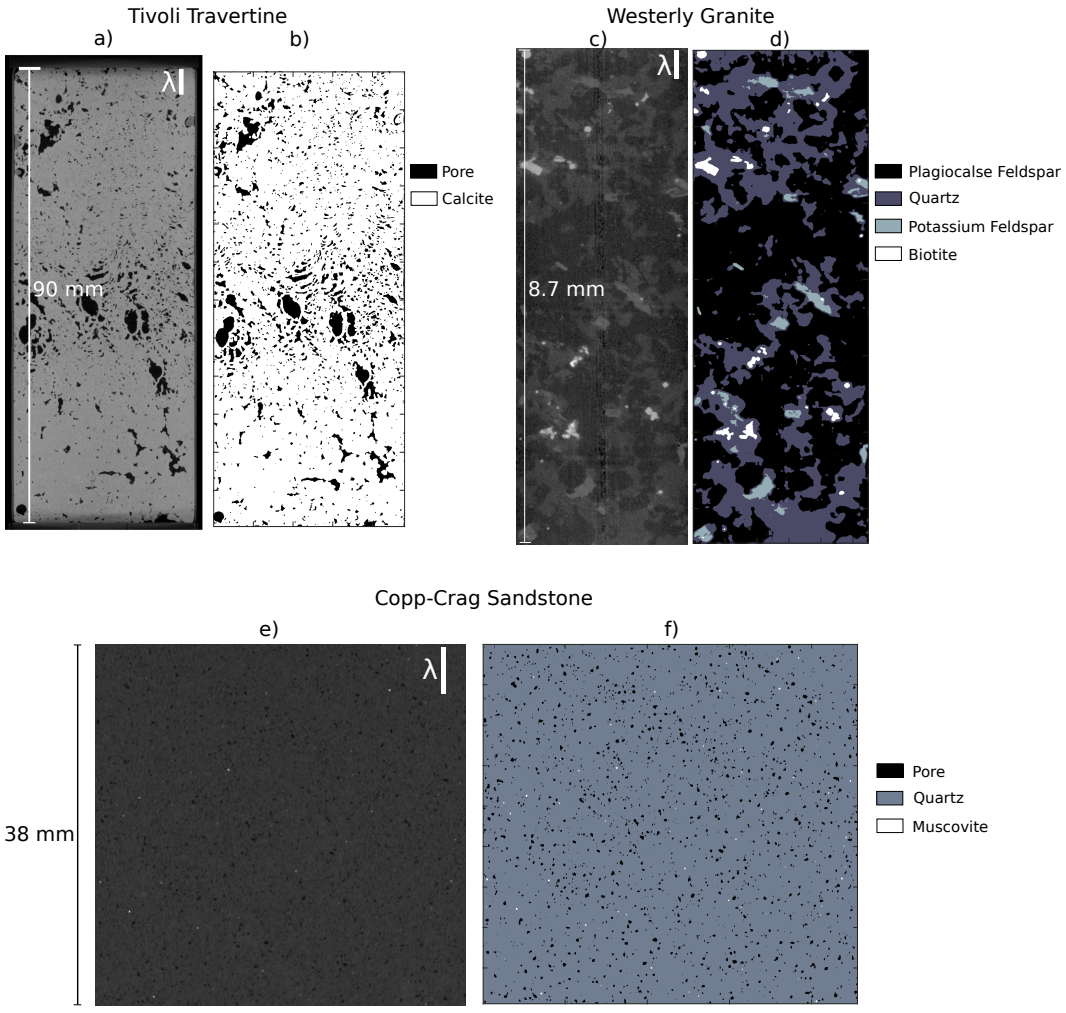

Figure 2. Set of X-ray μCT slices (left images) and equivalent models of segmented phases (right images) for three rock cores with varying heterogeneity and rock type: a) and b) Tivoli Travertine, c) and d) Westerly Granite, e) and f) Copp-Crag Sandstone. Model sizes are: 900x2400, 1000x3000 and 900x900 pixels for Tivoli Travertine, Westerly Granite and Copp-Crag, respectively. Approximate wavelength λ for each sample is labeled with a white bar, where the source signals contain a peak frequency of 30 MHz for Tivoli Travertine and Copp-Crag Sandstone, and 200 MHz for the smaller Westerly Granite model. The properties assigned to each material phase for wavefield simulation can be found in Table 1.

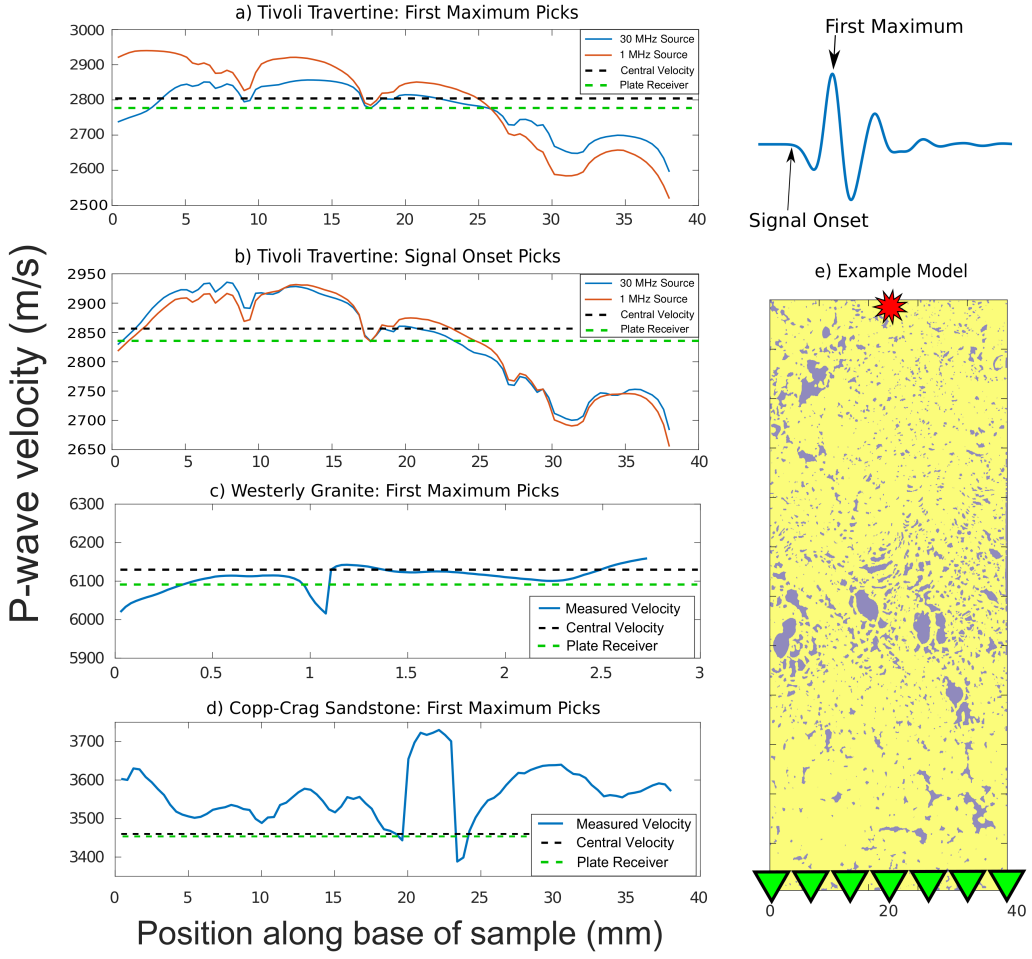

Figure 3. (a-d) Estimated seismic velocity as a function of receiver position, obtained from simulated waveforms through a μCT digital rock sample in a model shown (e) for the Tivoli Travertine. The source (star) is fixed at the top and receivers (triangles) are distributed along the bottom. The blue curve shows velocity estimates made using first-break arrival times and straight-line source-to-receiver distances. The dashed green line represents the conventional estimate of velocity using a single receiver at the center of the core. The dashed black line represent the fastest measured velocity. Results are for a) Tivoli Travertine picking the travel time of the first maximum and using a 30 MHz (blue) and 1 MHz (red) sources, b) Tivoli Travertine picking the travel time of the signal onset and using a 30 MHz (blue) and 1 MHz (red) sources c) Westerly Granite (200 MHz source), and d) Copp-Crag Sandstone (30 MHz source). The results in panels c and d are from picking the first maximum.

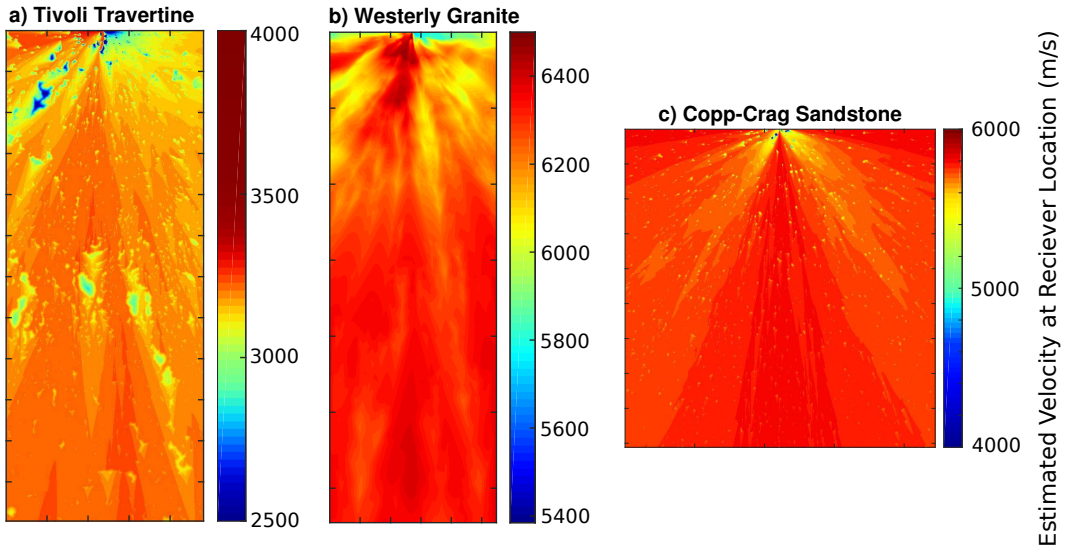

Figure 4. The estimated velocity as if a receiver was placed at every position in the model $\boldsymbol{x}$, using a fixed source location (centre of the top of the sample). To emulate estimates from the first break method, an eikonal ray tracing method (Margrave, 2007) was used to calculate travel times $t[\boldsymbol{x}]$, while a straight source-to-receiver ray path was used to calculate velocity $v[\boldsymbol{x}]$. Results are for a) Tivoli Travertine, b) Westerly Granite, and c) Copp-Crag Sandstone.

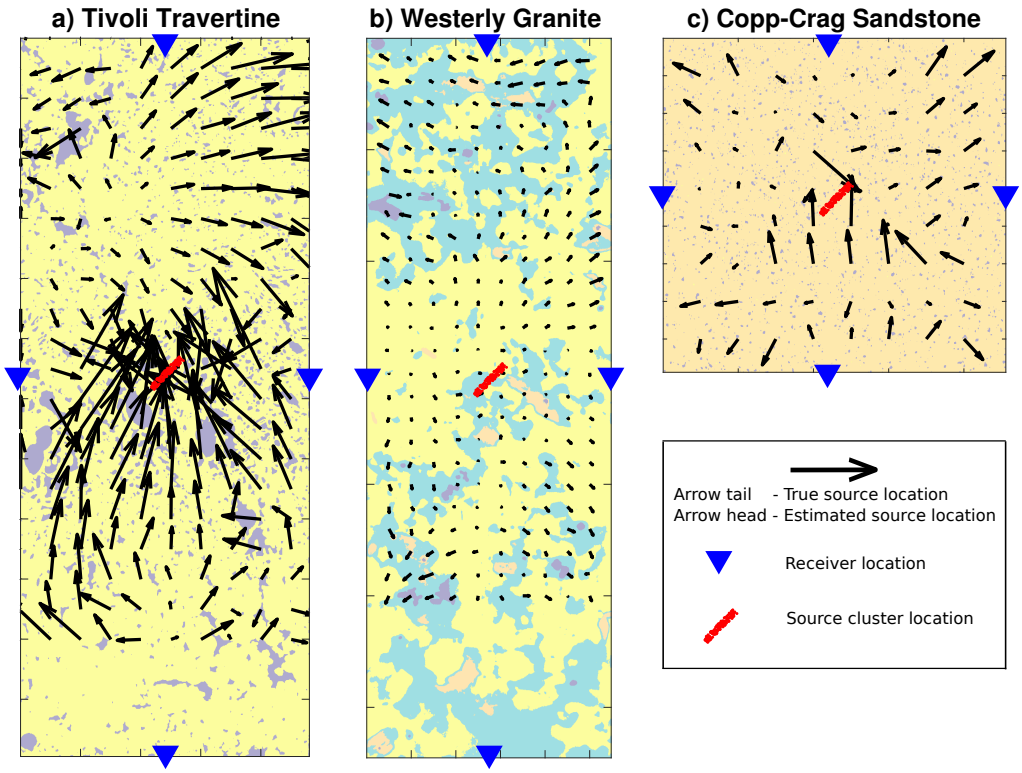

Figure 5. The resulting systematic errors in source location, represented as black arrows, using standard phase picking methods that assume a single representative velocity for each sample, for a) Tivoli Travertine, b) Westerly Granite, and c) Copp-Crag Sandstone. The base of each arrow is located at the true source positions (S_j), and estimated locations (S_{est}) are displayed at arrow tips. The red points represent the source cluster used for the source location experiment with results shown in Figure 7.

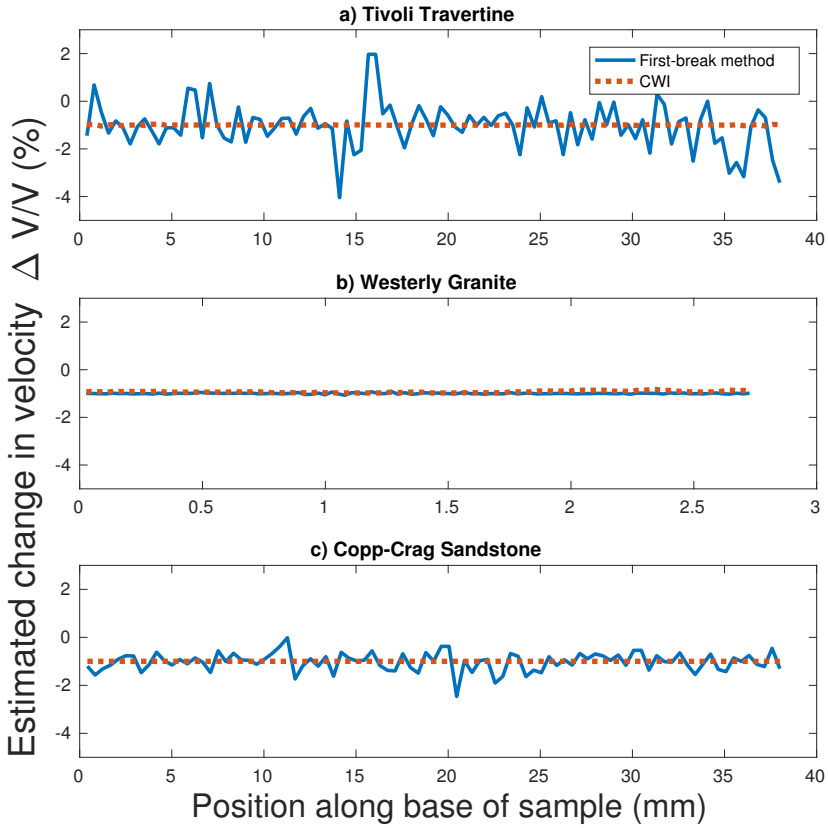

Figure 6. The estimation of a relative velocity change ΔV/V for a true change in velocity of -1%, i.e., ΔV/V = -0.01. Results for a) Tivoli Travertine, b) Westerly Granite, and c) Copp-Crag Sandstone. ΔV/V is estimated using the standard phase-picking method and Coda Wave Interferometry using each of 100 receiver locations along the base of each sample and a single source location at the center-top of each sample.

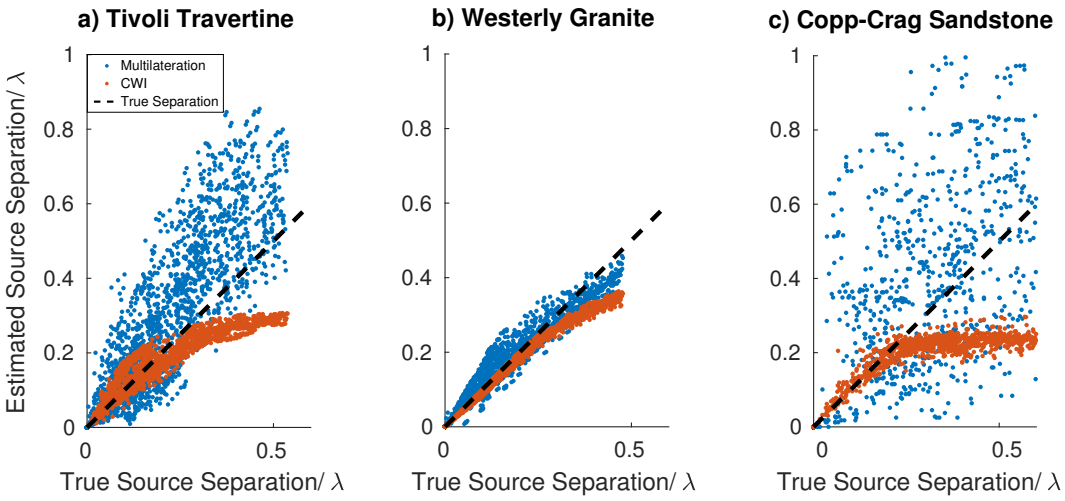

Figure 7. A comparison of estimated inter-source separation as a function of true inter-source separation (scaled by the wavelength λ at peak frequency) for the conventional multilateration method (using arrival times obtained from phase picking of first arrivals) and Coda Wave Interferometry. The true source cluster locations are represented as red dots in Figures 5a, b and c. a) Tivoli Travertine, b) Westerly Granite, and c) Copp-Crag Sandstone. The dashed line indicates the graph locations corresponding to perfect estimates.

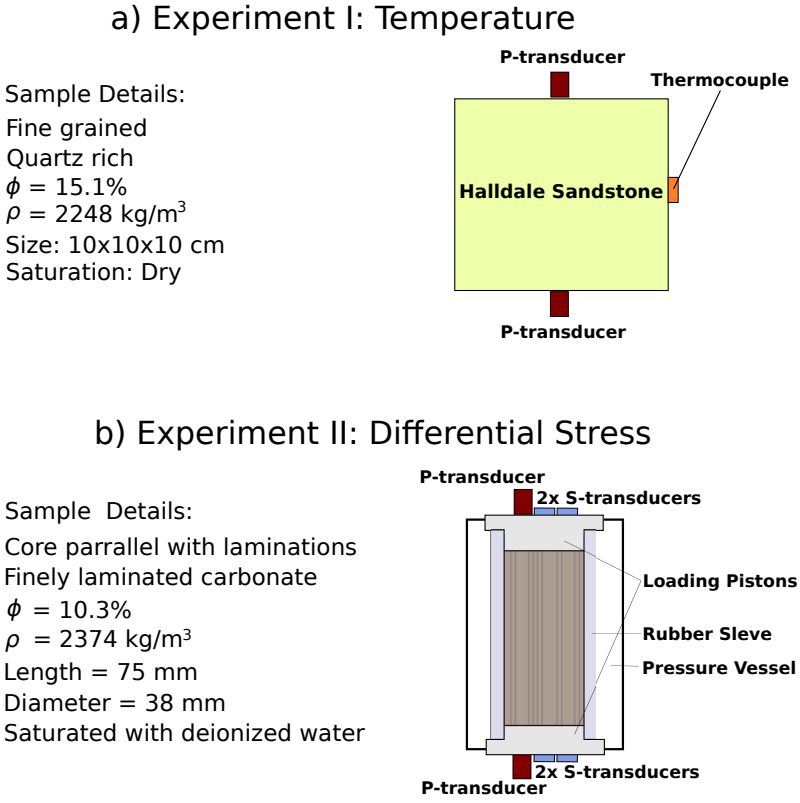

Figure 8. Schematic diagrams for the two experimental examples used for inducing a velocity change in the medium. a) Experiment I uses a variation in temperature of a cubic block of Halldale Sandstone. b) Experiment II uses varying differential stress on a finely laminated carbonate within a triaxial Hoek cell. Values for porosity (ϕ), density (ρ) and other properties of each sample are shown for each case.

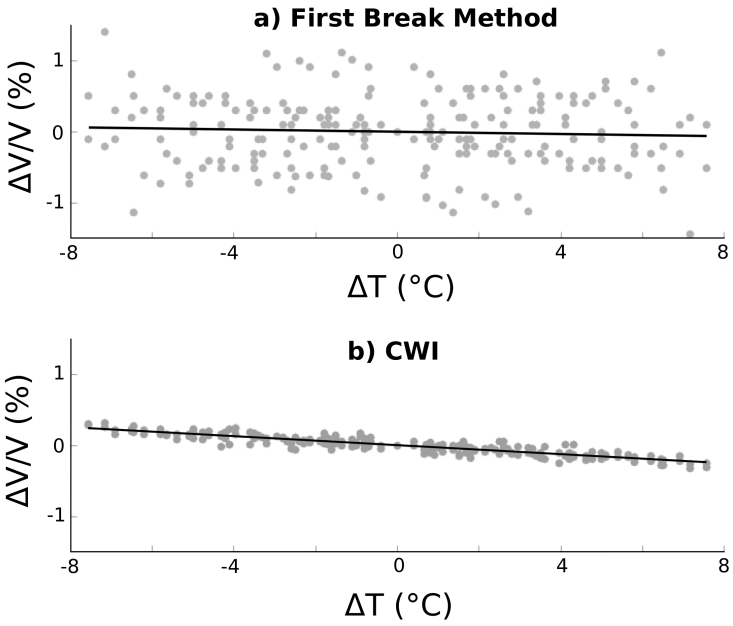

Figure 9. Estimated values of percentage velocity change ($\Delta V/V$) as a function of the change in temperature (ΔT) in a 10 cm^3 sample of Halldale Sandstone, a) for the standard method of picking arrival times, and b) for Coda Wave Interferometry. Solid lines are best-fit linear regressions. The zero point on the x axis ($\Delta T = 0$) is arbitrary.

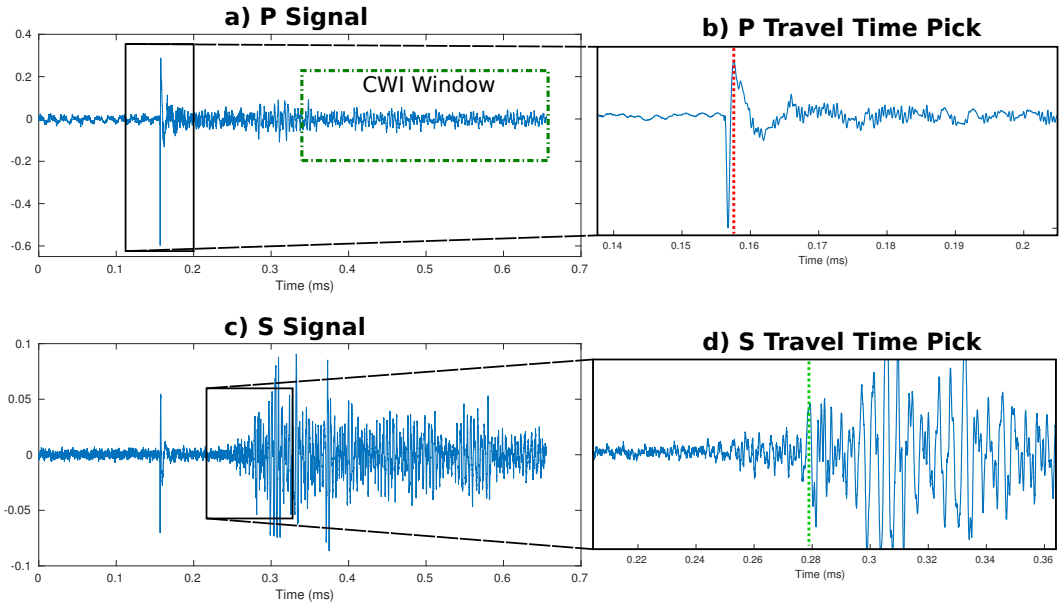

Figure 10. Example waveforms to illustrate the picking procedure for the first break method. a) Full recorded signal using Glaser-type sensors sensitive to displacement normal to the sensor face. b) First arriving waves: the first maximum is manually picked as the arrival time. c) Full recorded signal using S wave transducers for the source and receiver, sensitive to displacement tangential to the sensor face. d) Manually picked first arriving S wave maximum. The time window used for CWI is labeled in panel a.

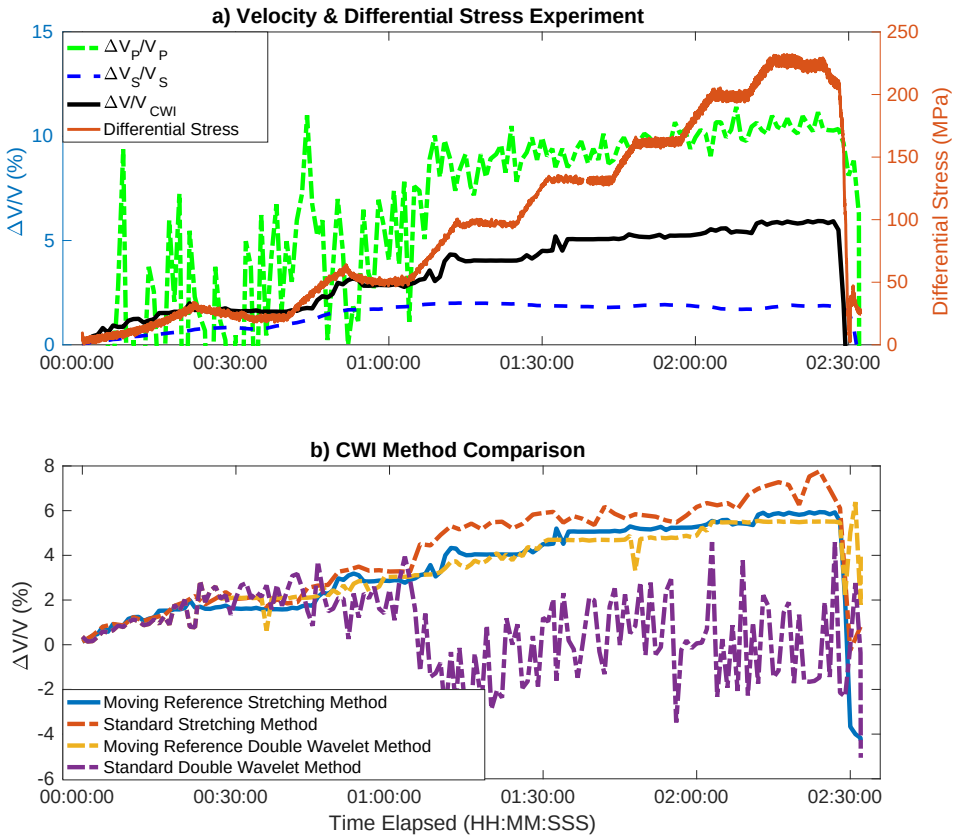

Figure 11. a) Velocity change of a finely laminated carbonate rock during experimental deformation by increasing differential stress (red), with corresponding stress values labeled on the right axis. The response of velocity ($\Delta V/V$), labeled on the left axis, is estimated by the first-break method for P and S wave velocities (dashed lines) and by a CWI moving-reference trace method (black). b) A comparison of CWI algorithms, showing the effect of implementing a moving reference trace (Equation 3) for both the stretching and double wavelet methods.

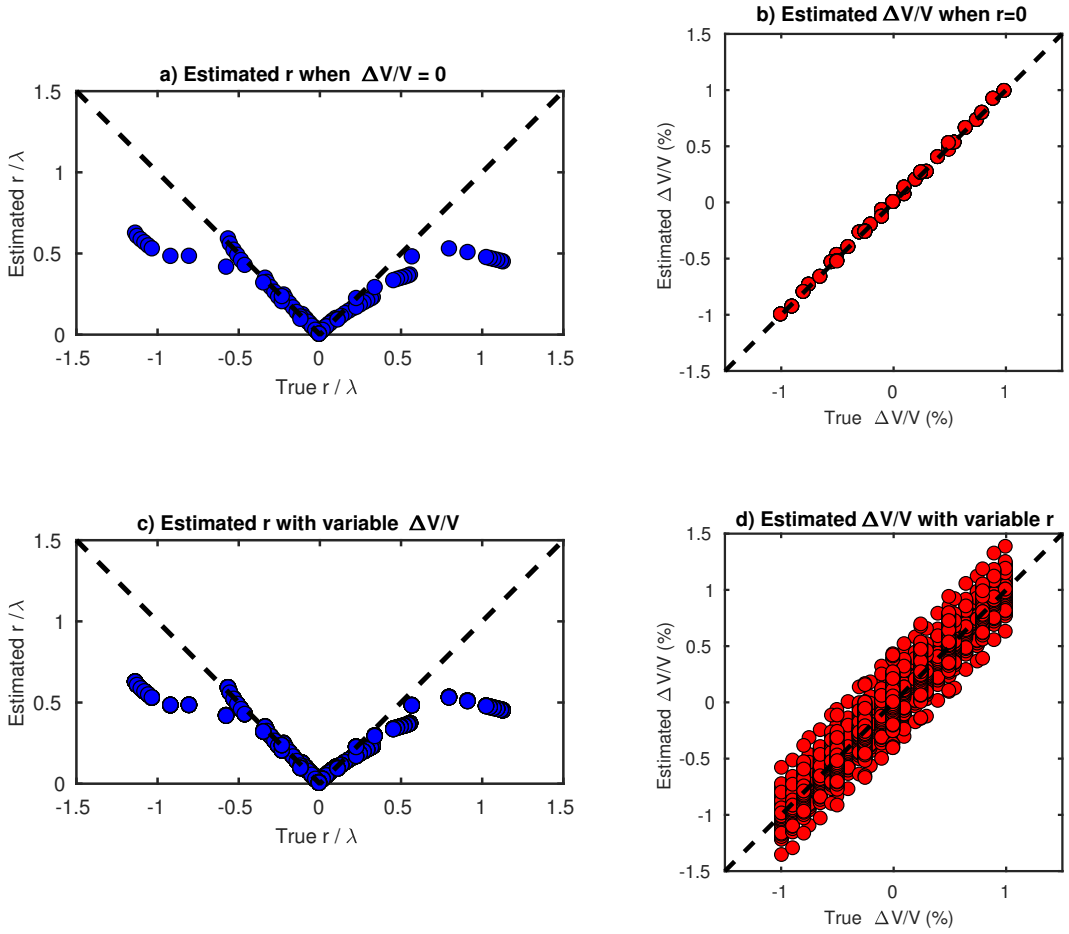

Figure 12. Assessing the ability of CWI to estimate velocity changes $\Delta V/V$ and inter-source separation r simultaneously in the presence of both velocity and source location perturbations. a) Estimated r when velocity is not perturbed. b) Estimated $\Delta V/V$ when the source location is not perturbed. c) Estimates of r with simultaneous velocity perturbations. d) Estimates of $\Delta V/V$ with simultaneous perturbations of source location.

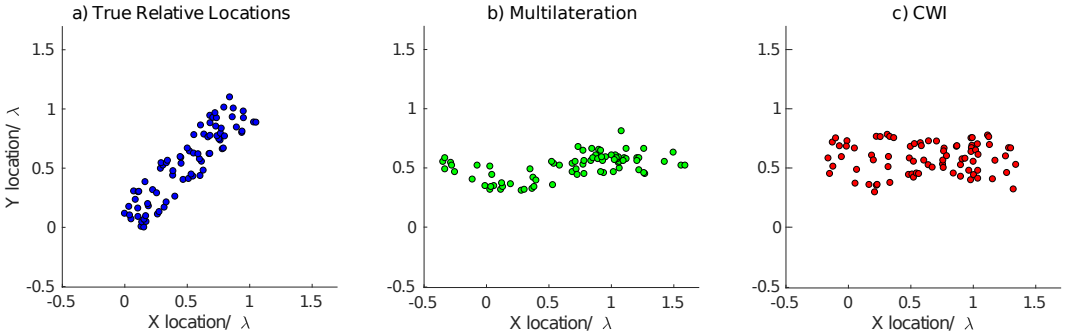

Figure 13. a) True locations of a cluster of acoustic emissions simulated in the Tivoli Travertine μCT slice in Figure 2b. b) Estimated cluster locations using the conventional method of first-break arrival times and multilateration using the receiver geometry in Figure 5a. c) Estimated relative locations found by implementing the CWI-based optimization algorithm described in Zhao et al. (2017), using the inter-source separations estimated from CWI using the same receiver geometry (note these locations have been rotated in plane to best fit the locations in panel b for fair for comparison, as the optimization provides only relative locations).

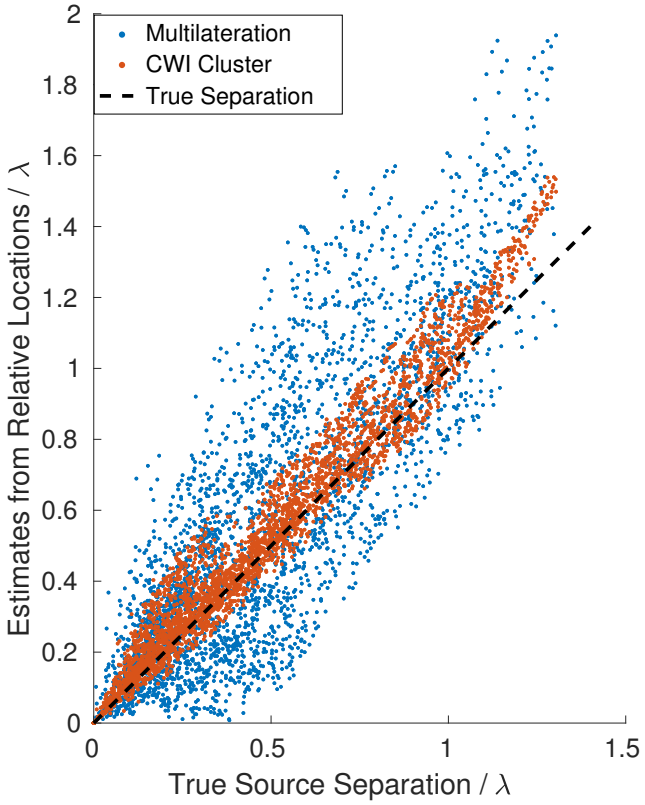

Figure 14. Source separation values from the estimated location clusters shown in Figures 13b and c, as a function of true source separation. The dashed line shows where true separation estimates would lie.

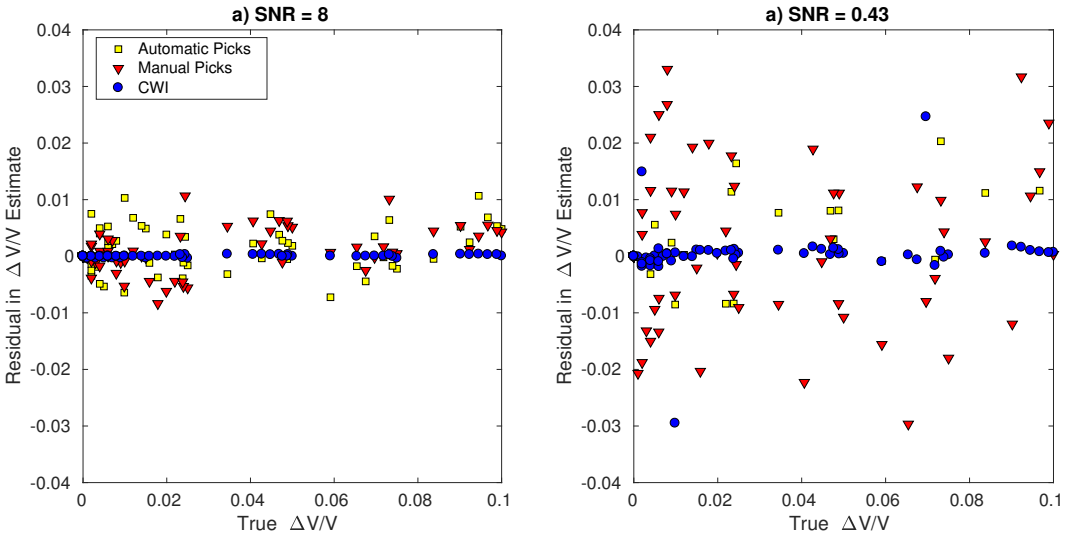

Figure 15. Residuals of estimated $\Delta V/V$ from Coda Wave Interferometry, and from travel times obtained by auto-picking and manual picks, estimated at a) SNR = 8 and b) SNR = 0.43 and plotted as a function of the true velocity change.

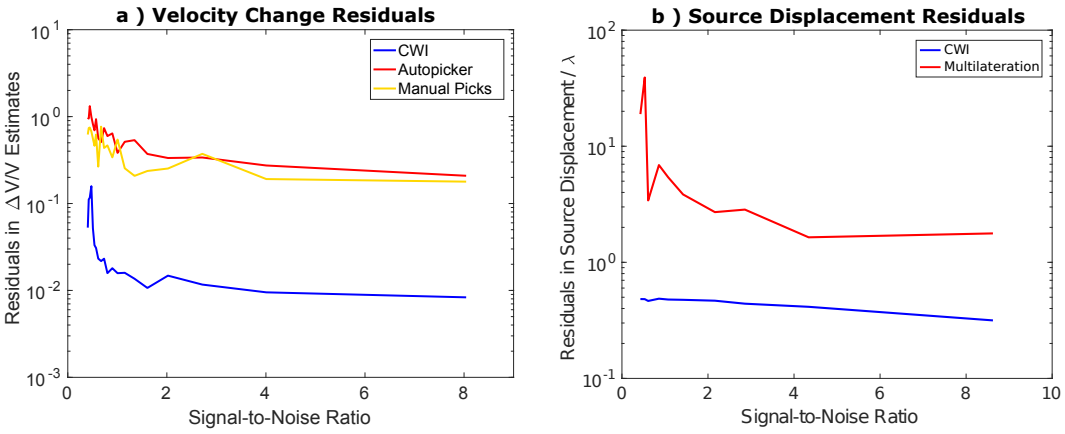

Figure 16. a) Residuals between true and estimated velocity change ($\Delta V/V$) as a function of signal-to-noise ratio. b) Residuals between true and estimated source displacement r/λ as a function of signal-to-noise ratio.

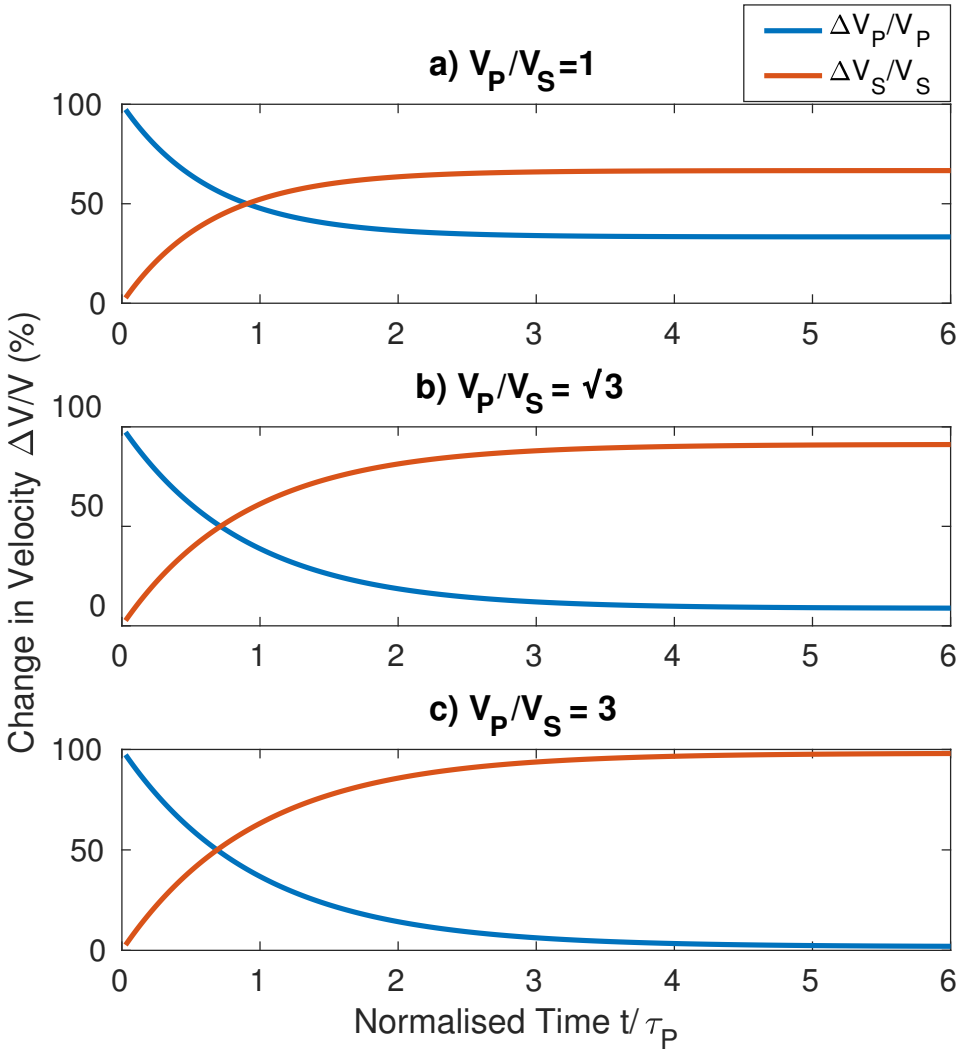

Figure 17. Relative proportions of changes in P-wave velocity ($\Delta V_P/V_P$) and S-wave velocity ($\Delta V_S/V_S$) which make up the change in velocity estimated from CWI ($\Delta V/V$) as a function of time along the coda, using equations 19 and 20 taken from Snieder (2002). Multiple relations are shown for media of varying V_P/V_S ratios: a) b) $V_P/V_S = 1$, b) $V_P/V_S = \sqrt{3}$, c) $V_P/V_S = 3$. Time is normalized by dividing time t by the transit time of one mean free path ($\tau_P = l_P/V_P$).

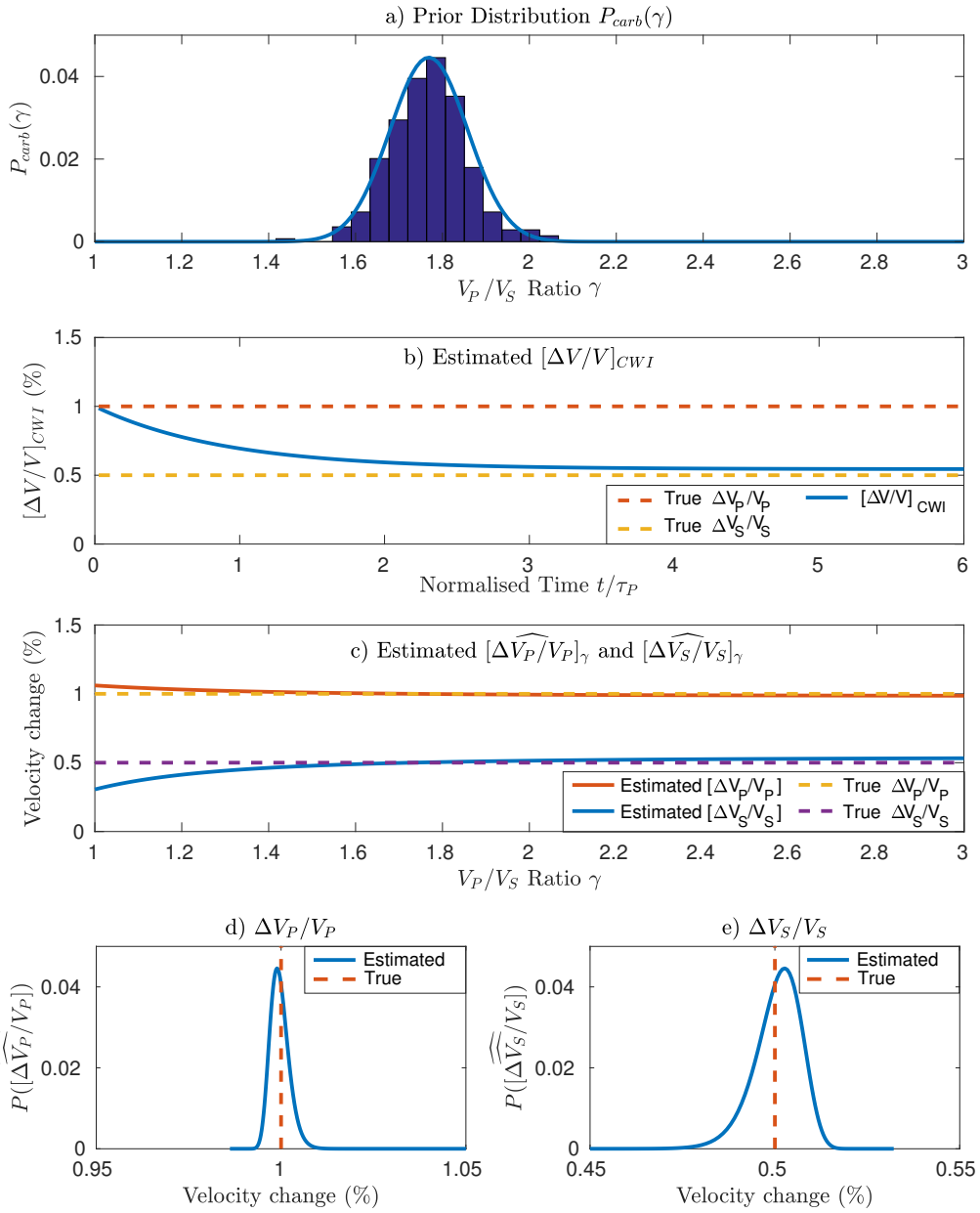

Figure 18. a) Prior distribution of V_P/V_S ratios from measured dry carbonate data compiled from Bakhorji (2010), Fournier et al. (2011) and Verwer et al. (2008). The curve shows the best fitting normal distribution function of the histogram. b) Synthetic $[\Delta V/V]_{CWI}$ data generated using Equation 21, where $\Delta V_P/V_P = 1\%$, $\Delta V_S/V_S = 0.5\%$ and $\gamma = \sqrt{3}$). c) Estimated $[\Delta\widehat{V_P/V_P}]_\gamma$ and $[\Delta\widehat{V_S/V_S}]_\gamma$ from an ordinary least squares inversion of the forward modeled $[\Delta V/V]_{CWI}$ data in panel b, as a function of the V_P/V_S ratio used in the inversion. d) and e) show the probability density functions (solid blue lines) for estimates of $\Delta V_P/V_P$ and $\Delta V_S/V_S$, where the dashed red lines represent the true changes in velocity ($\Delta V_P/V_P = 1\%$, $\Delta V_S/V_S = 0.5\%$), using samples from prior distribution in panel a and Equations 22 and 23.

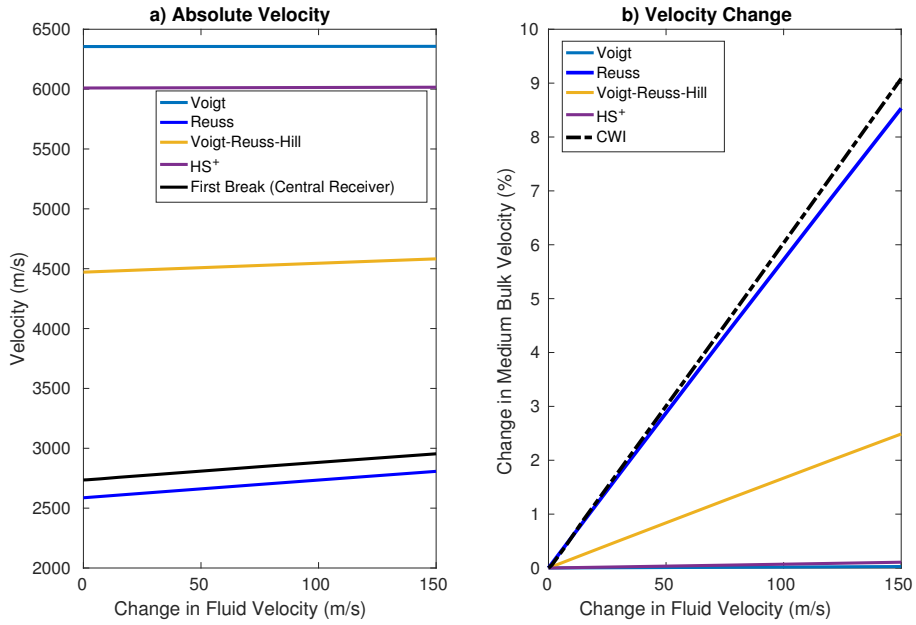

Figure 19. a) Calculated average velocity for the Tivoli Travertine digital rock sample following multiple perturbation of fluid velocity. The medium velocity is calculated using a range of bounding methods including the Voigt upper bound, Reuss lower bound, the Voigt-Reuss-Hill average and the Hashin-Shtrikman upper bound (HS^+), see Mavko et al. (2009). The velocity is also estimated using the first break method on a central receiver (black). b) The change in bulk velocity ($\Delta V/V$) as a function of fluid velocity perturbation, calculated with the multiple averages. The dotted black line is the estimate of velocity change ($\Delta V/V$) attained using CWI.

Figure 1.

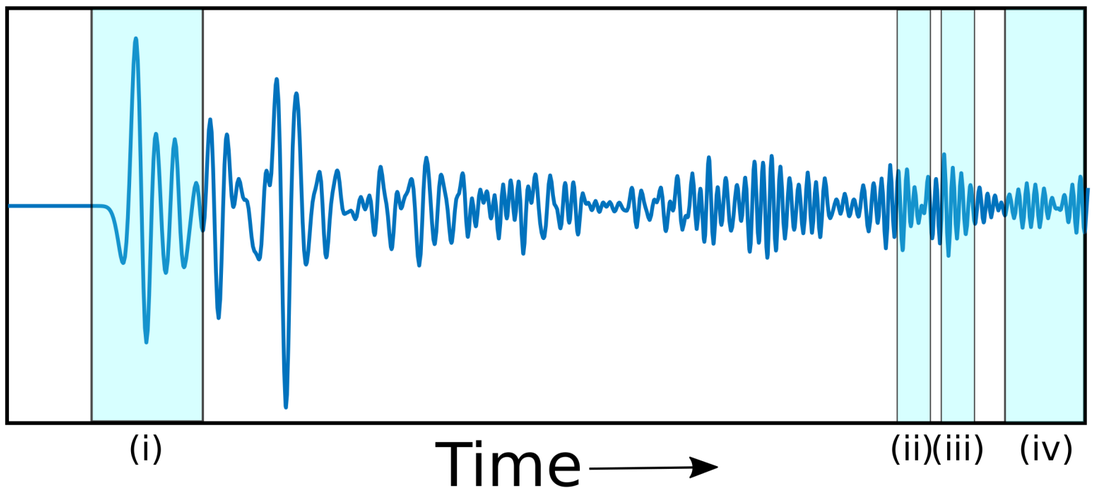

a) Perturbation of Velocity

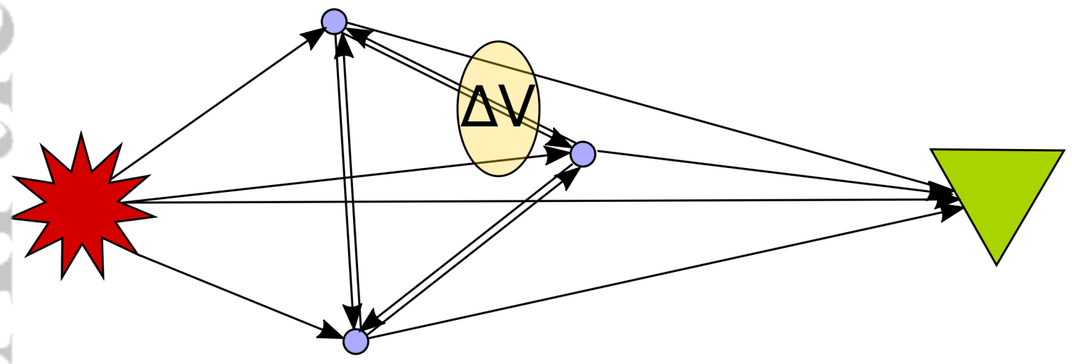

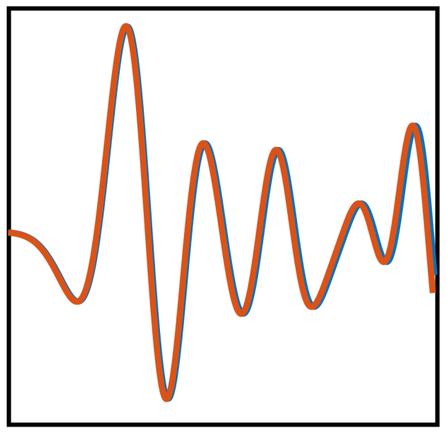
Time window (i)

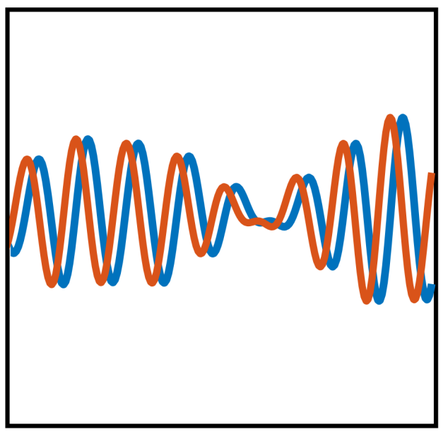
Time window (iv)

b) Perturbation of Source Location

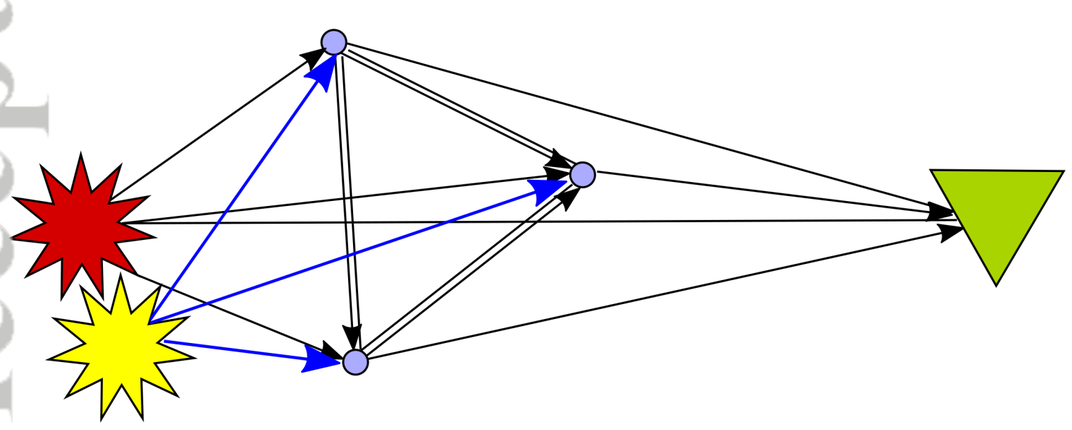

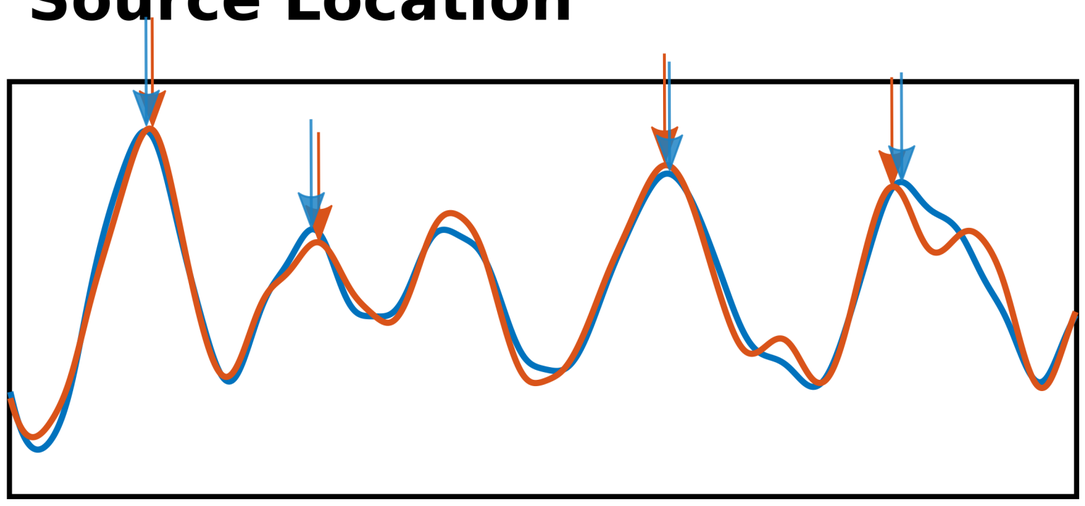
Time window (ii)

c) Perturbation of Scatterer Locations

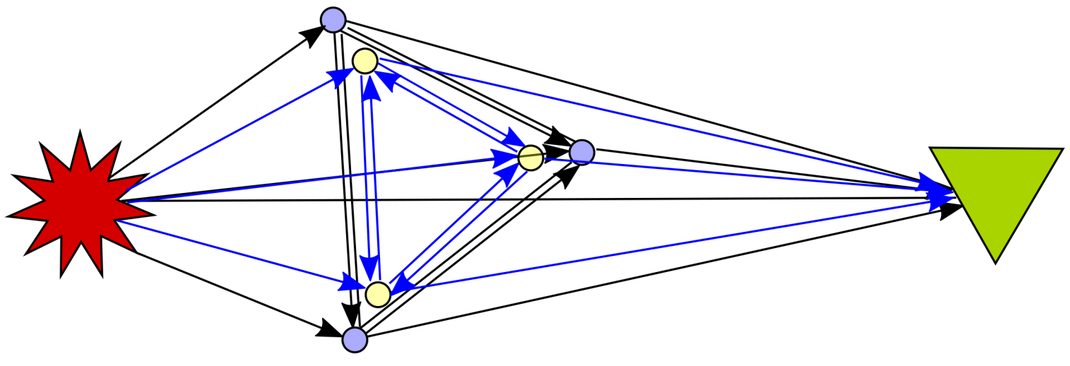

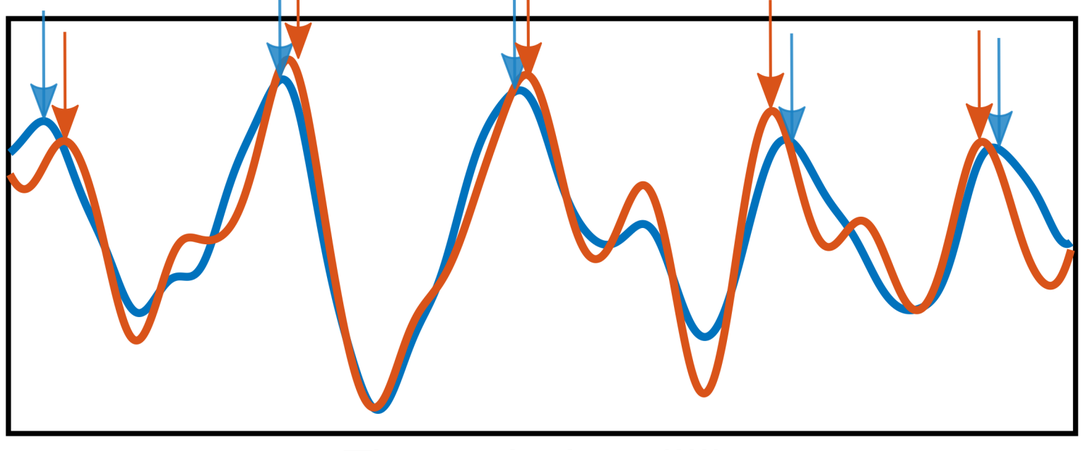
Time window (iii)

Figure 2.

Tivoli Travertine

a)

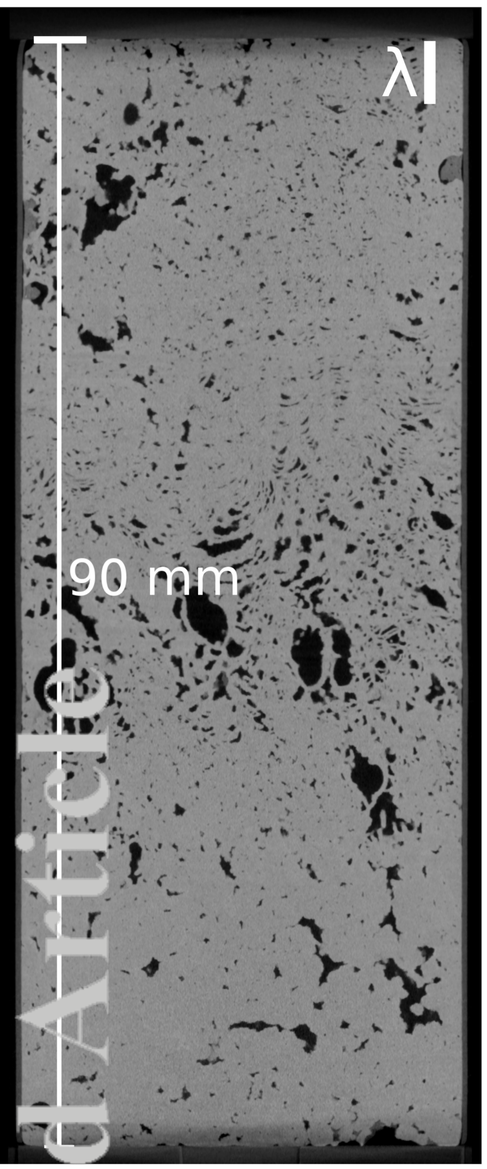

b)

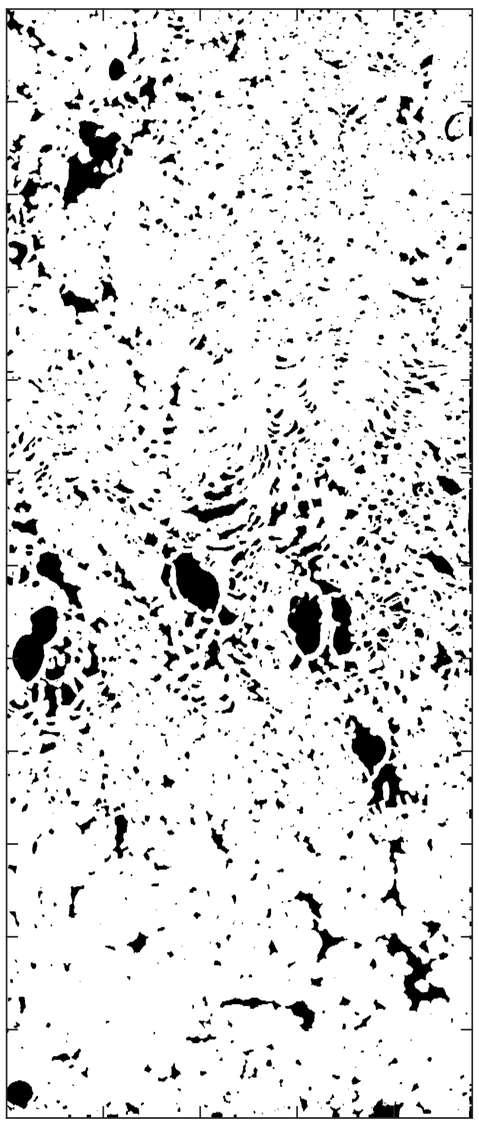

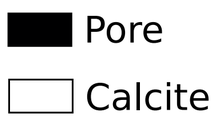

Westerly Granite

c)

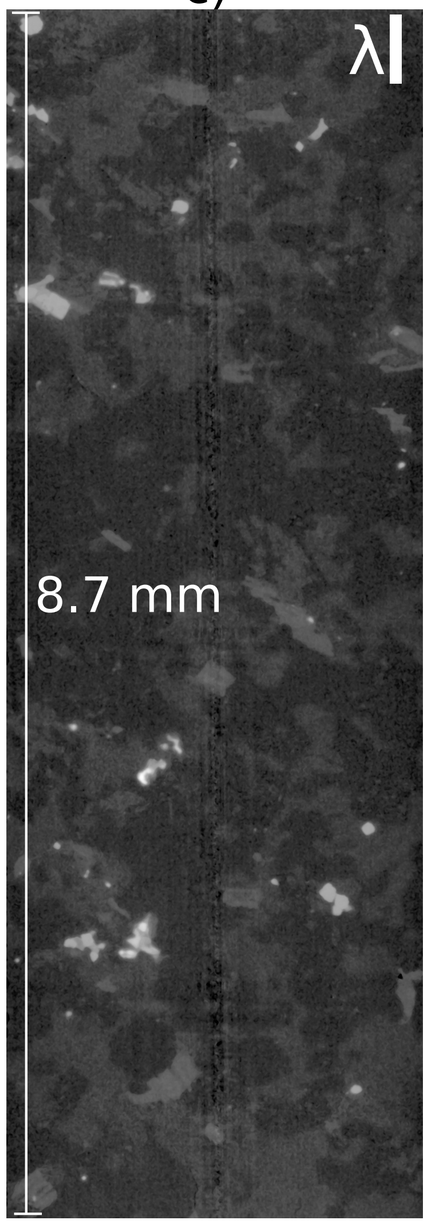

d)

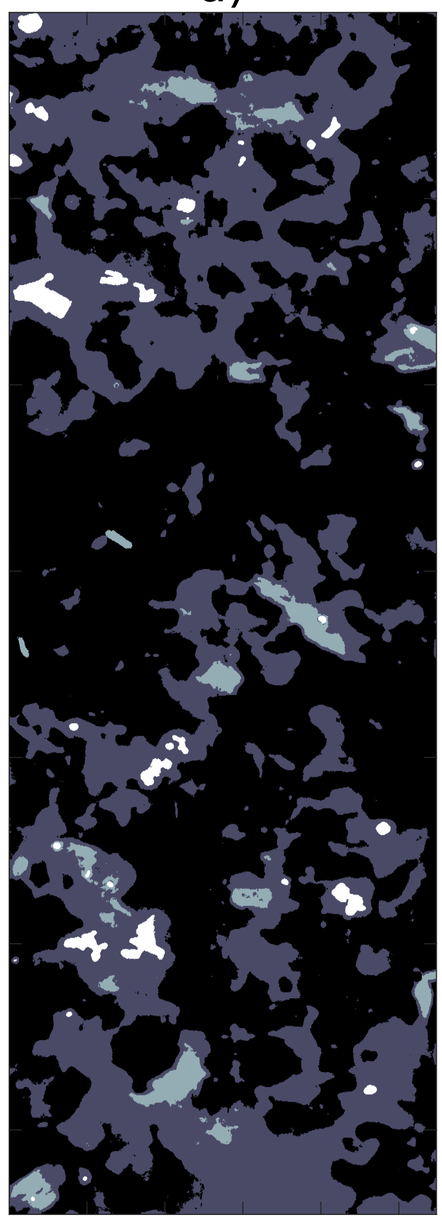

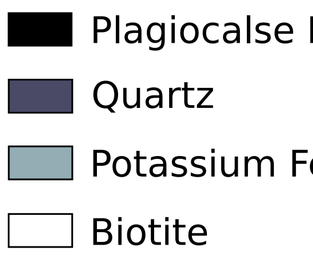

Copp-Crag Sandstone

e)

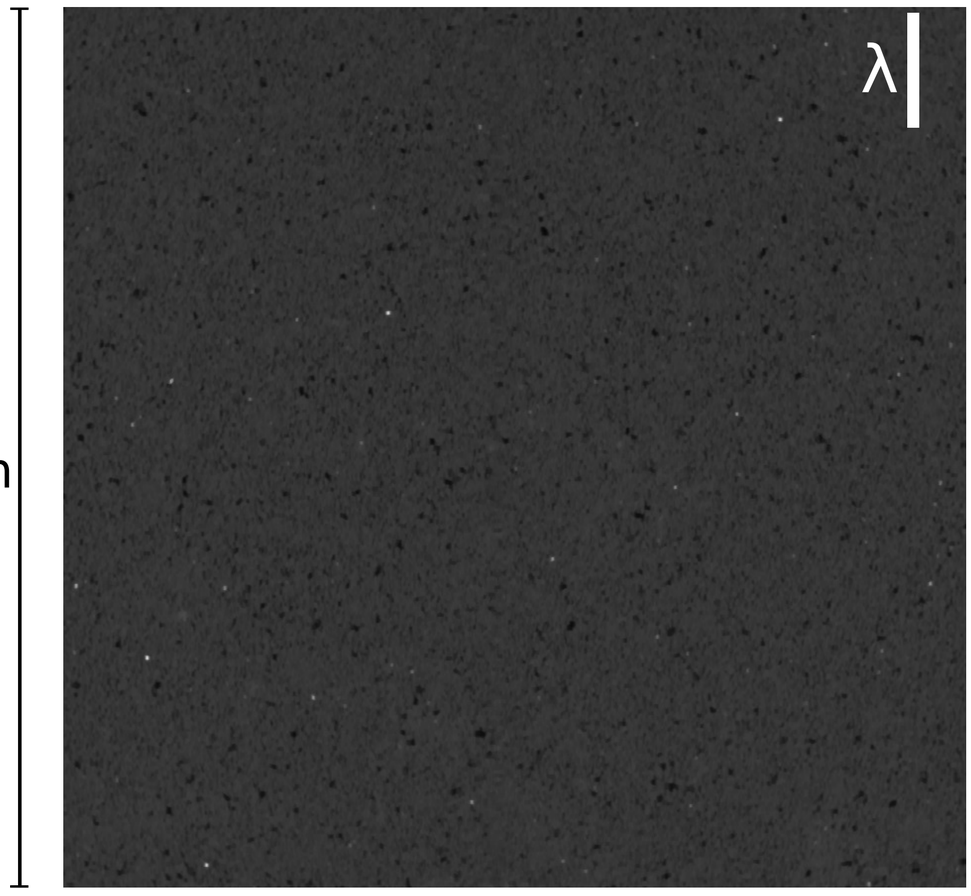

f)

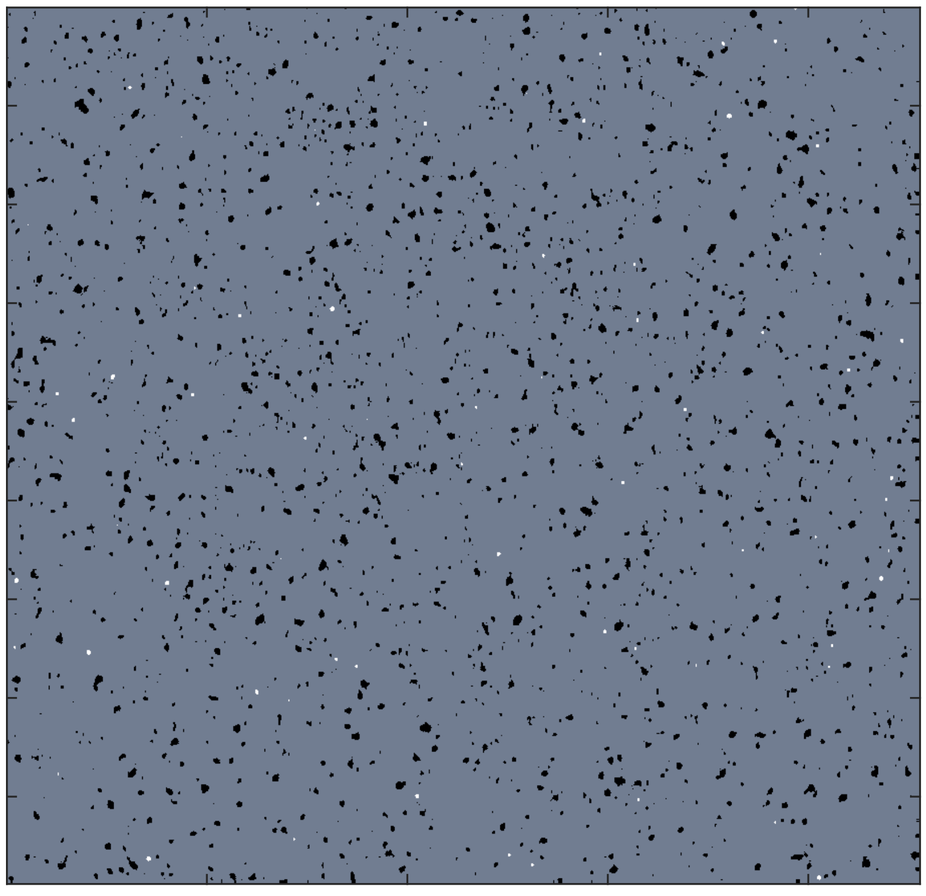

Figure 3.

a) Tivoli Travertine: First Maximum Picks

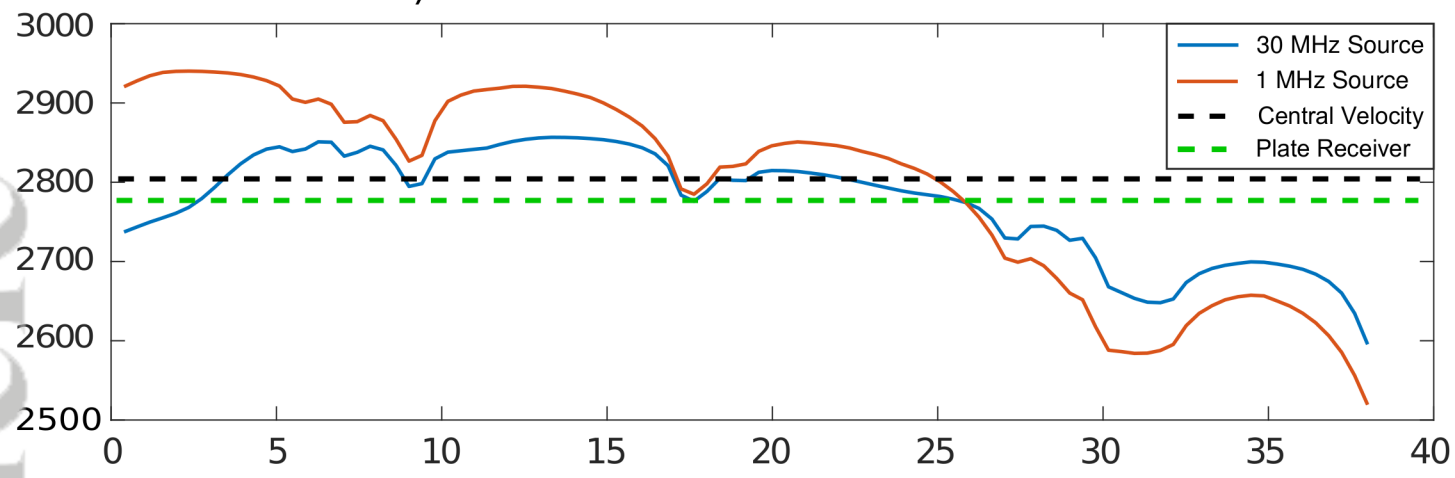

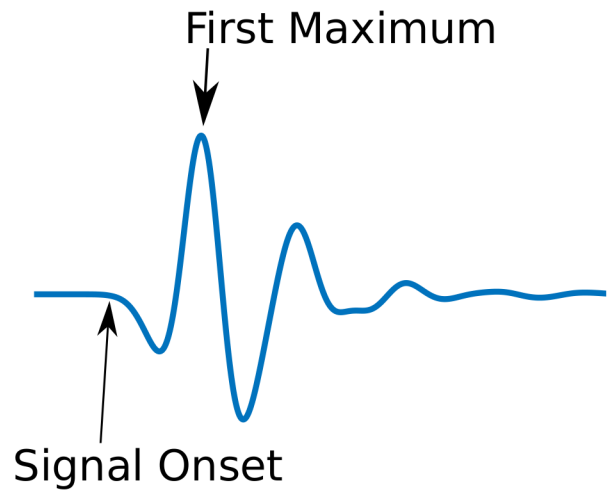

b) Tivoli Travertine: Signal Onset Picks

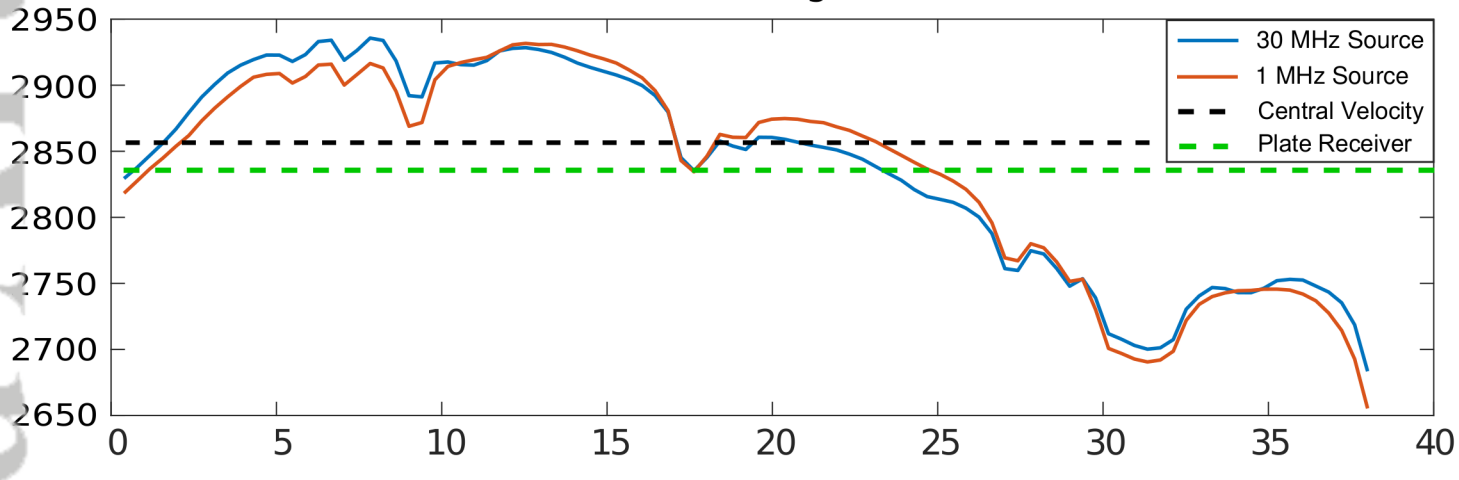

e) Example Model

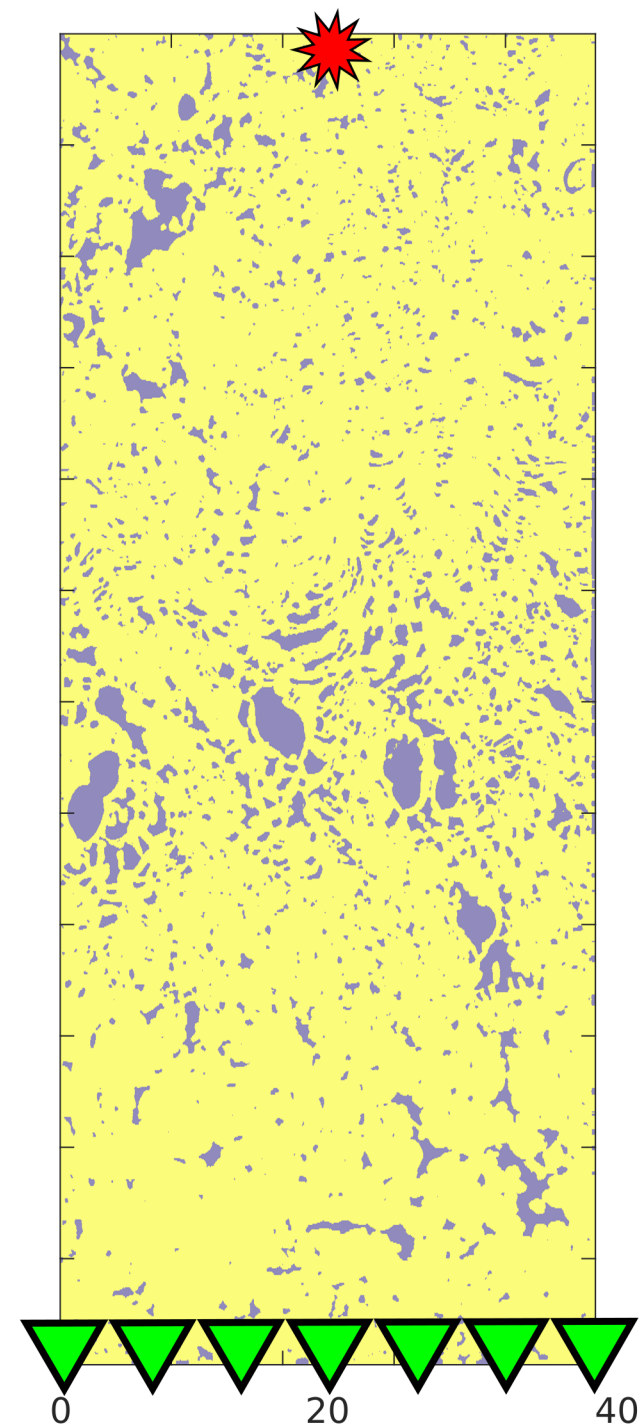

c) Westerly Granite: First Maximum Picks

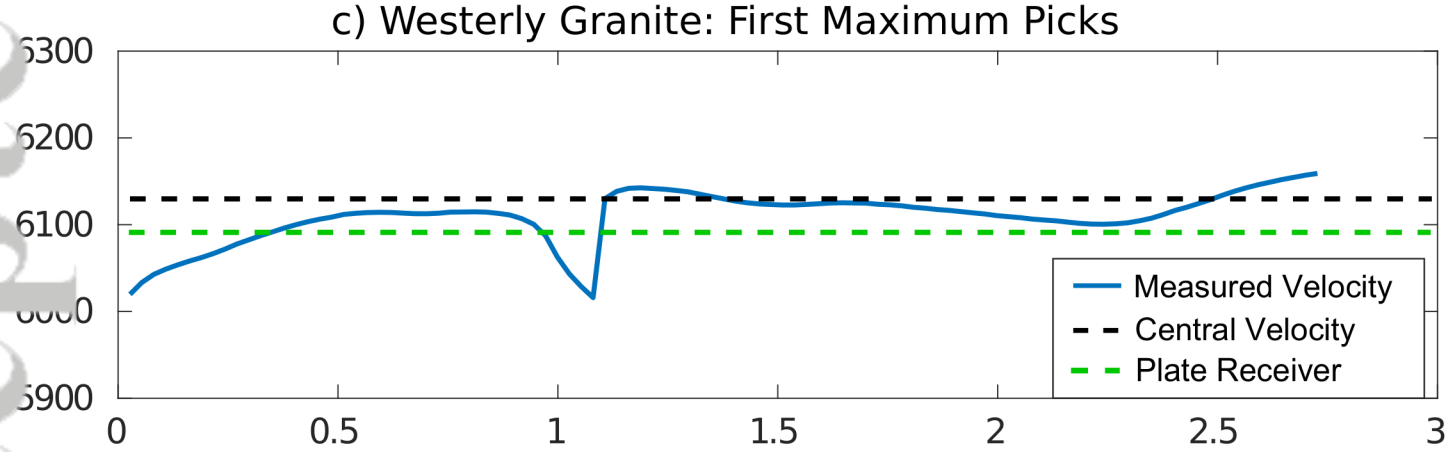

d) Copp-Crag Sandstone: First Maximum Picks

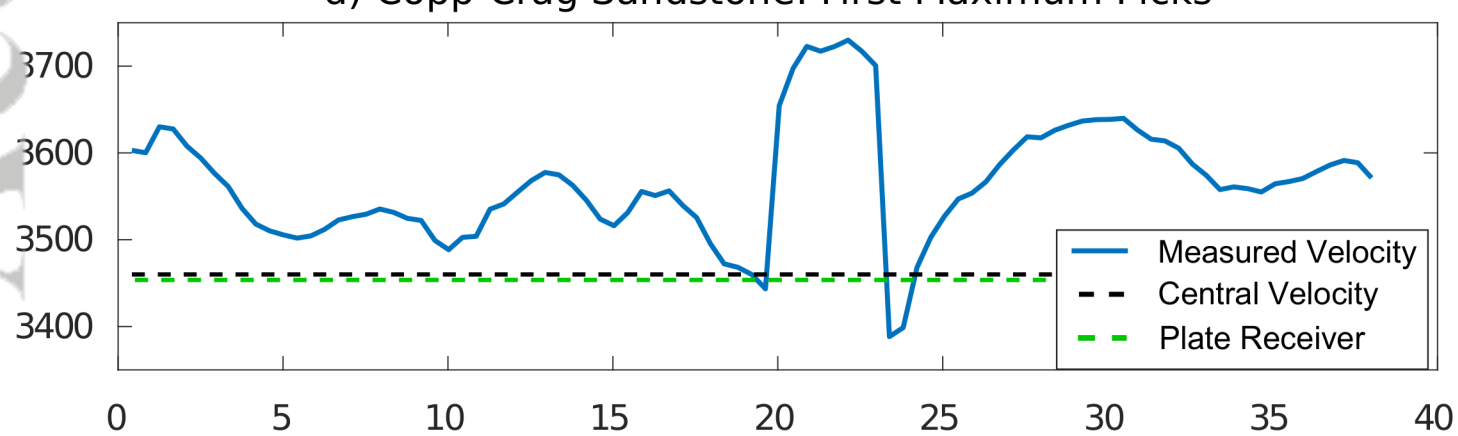

P wave velocity (m/s)

Position along base of sample (mm)

Figure 4.

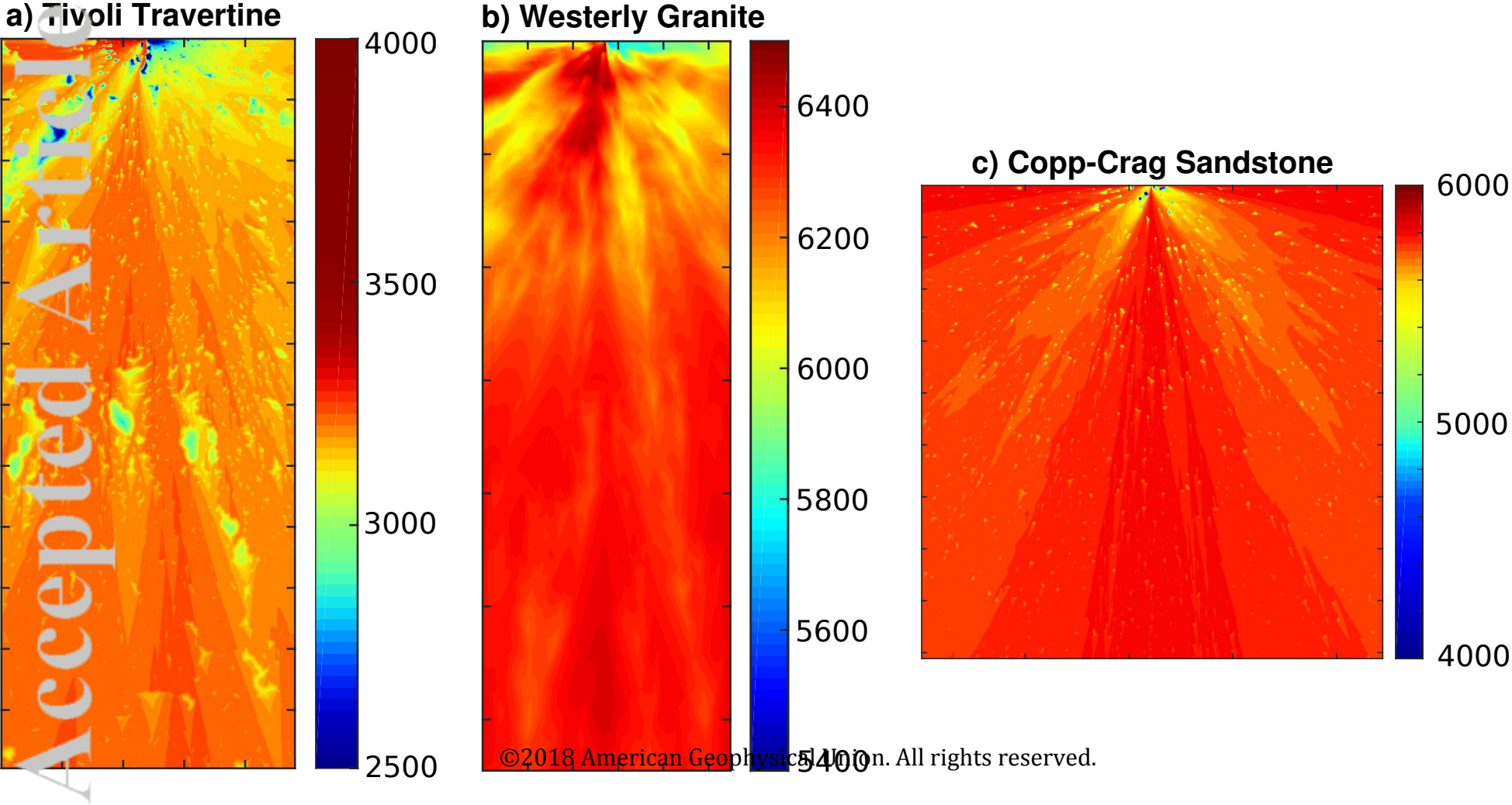

Figure 5.

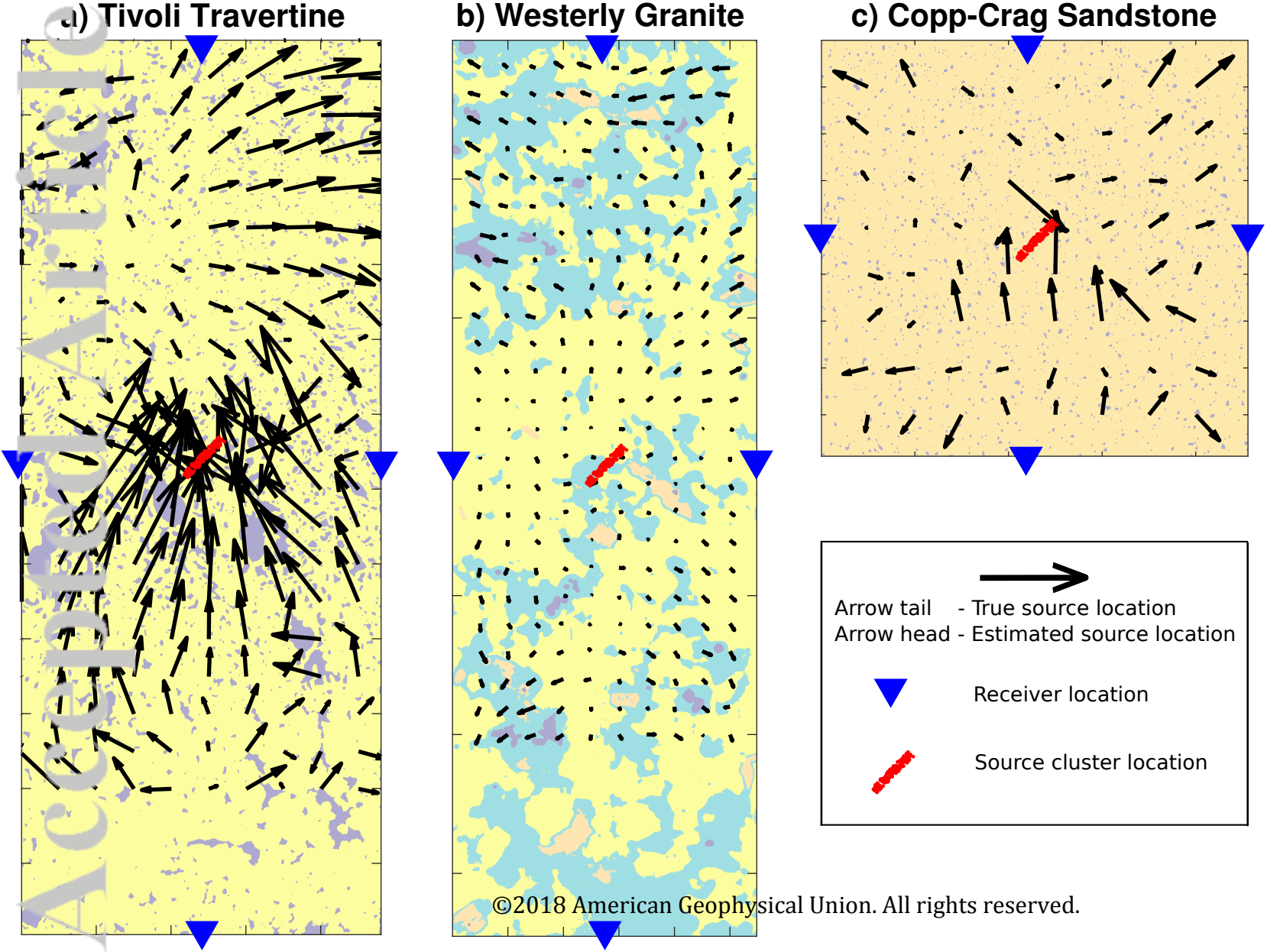

Figure 6.

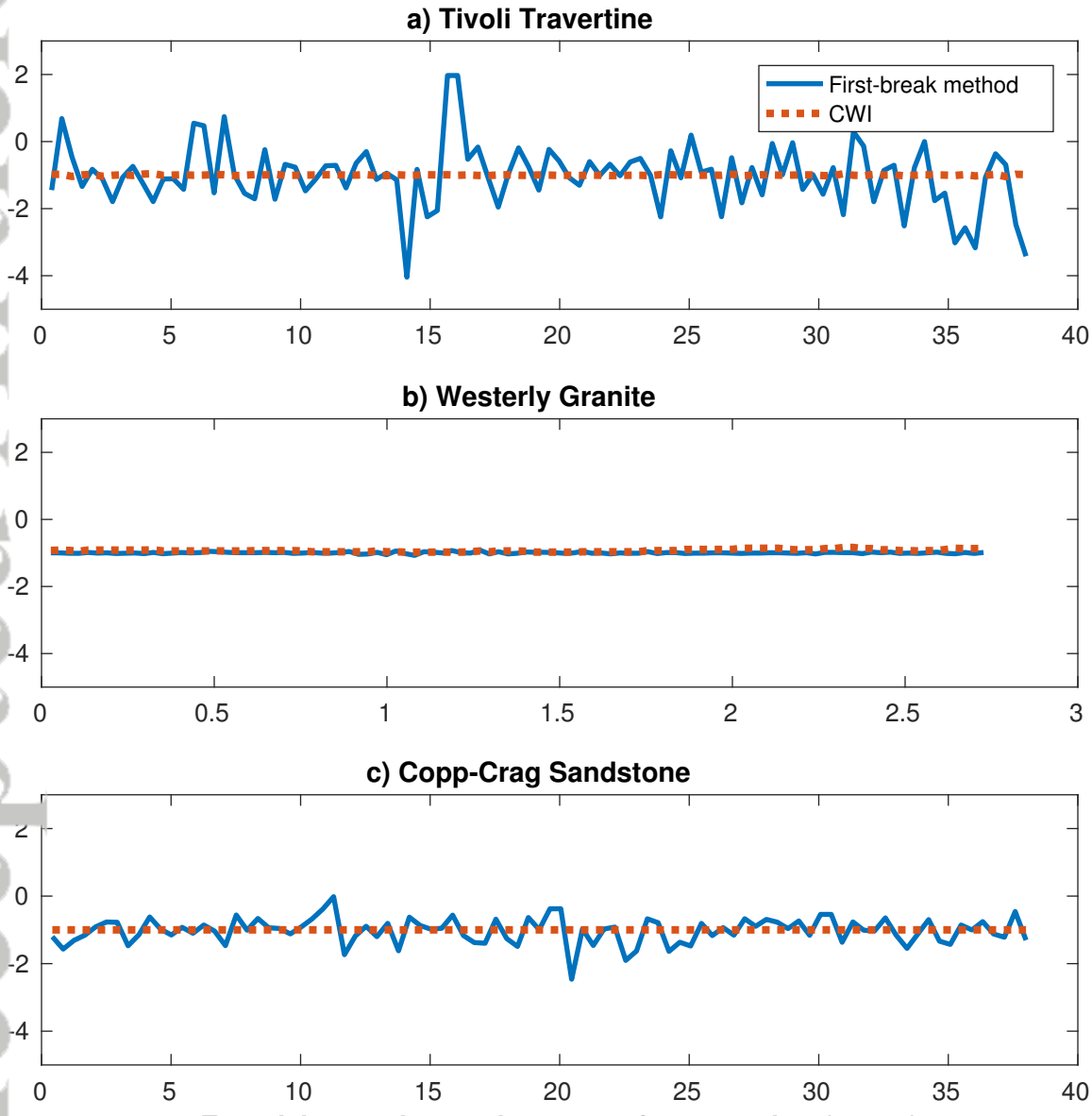

Figure 7.

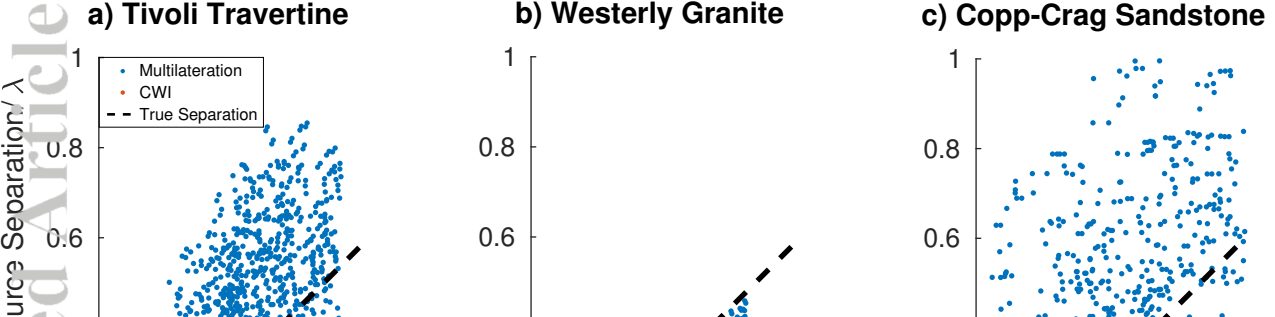

Figure 8.

a) Experiment I: Temperature

Sample Details:

Fine grained

Quartz rich

ϕ = 15.1%

ρ = 2248 kg/m^3

Size: 10x10x10 cm

Saturation: Dry

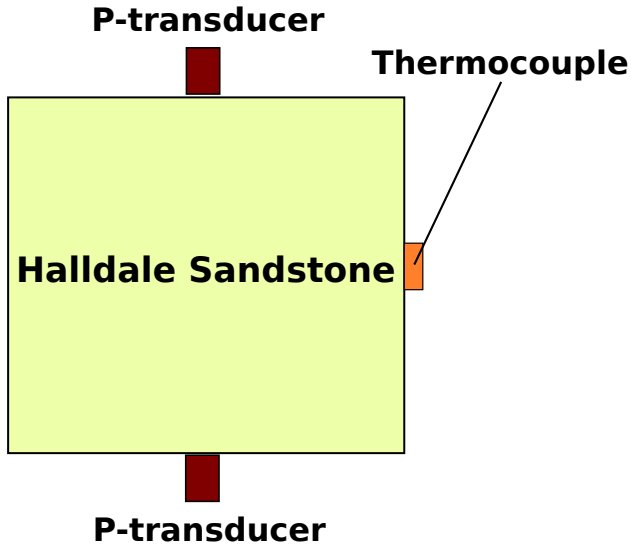

b) Experiment II: Differential Stress

Sample Details:

Core parallel with laminations

Finely laminated carbonate

ϕ = 10.3%

ρ = 2374 kg/m^3

Length = 75 mm

Diameter = 38 mm

Saturated with deionized water

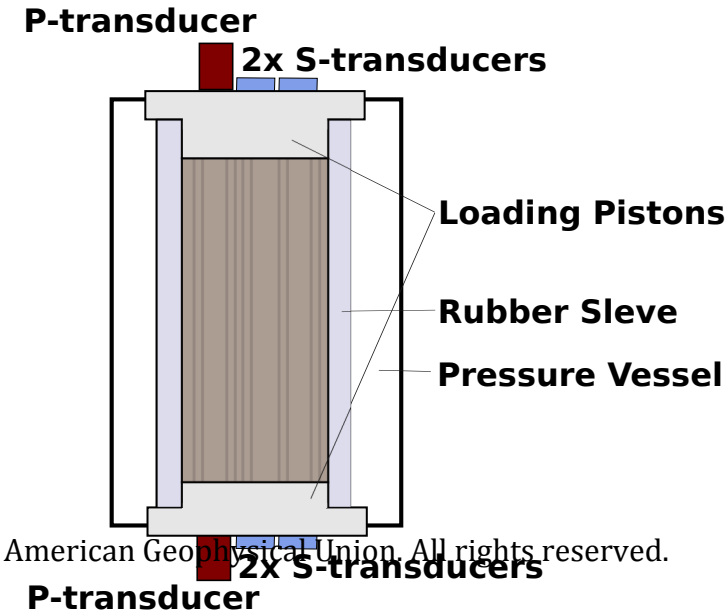

Figure 9.

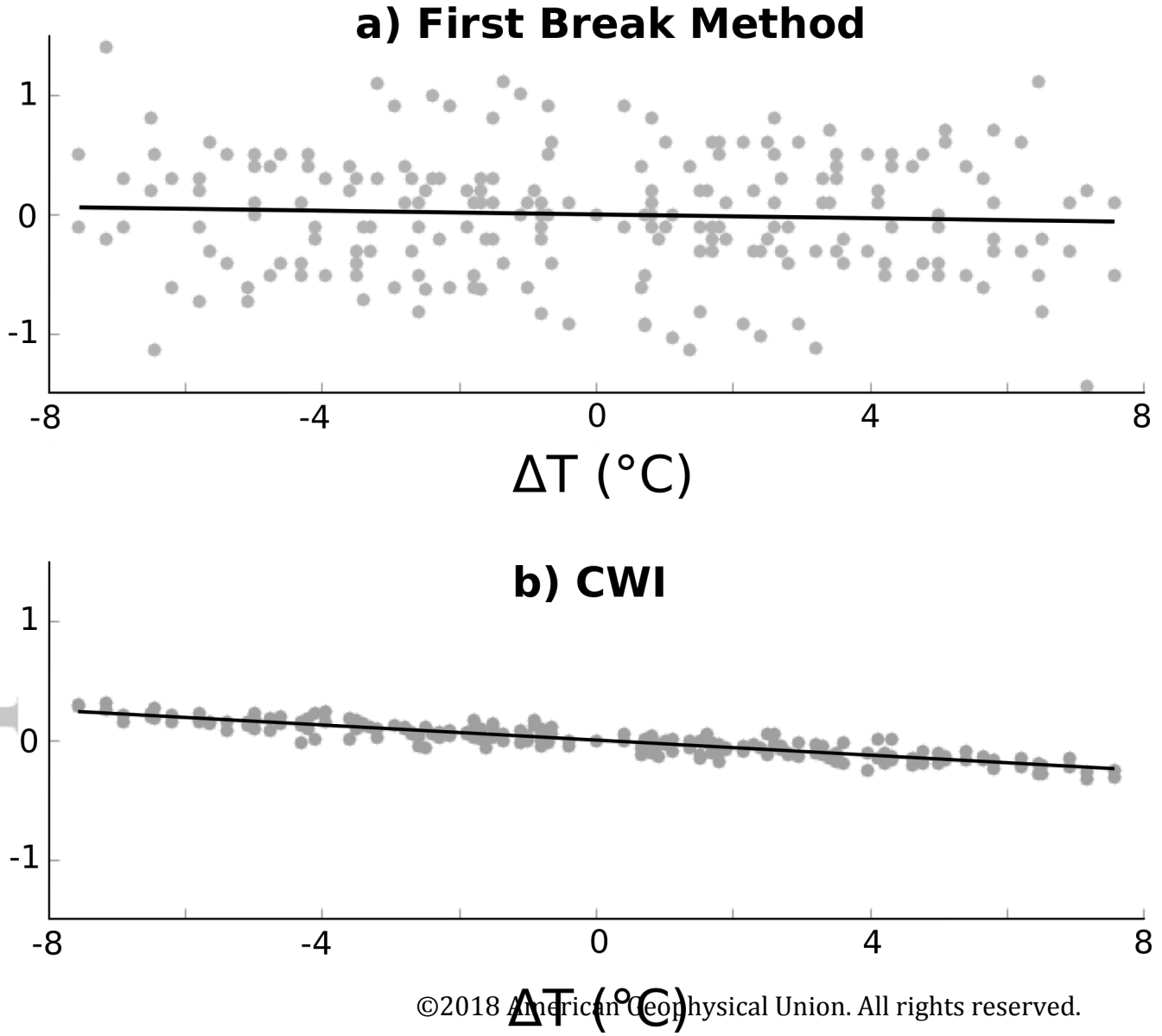

Figure 10.

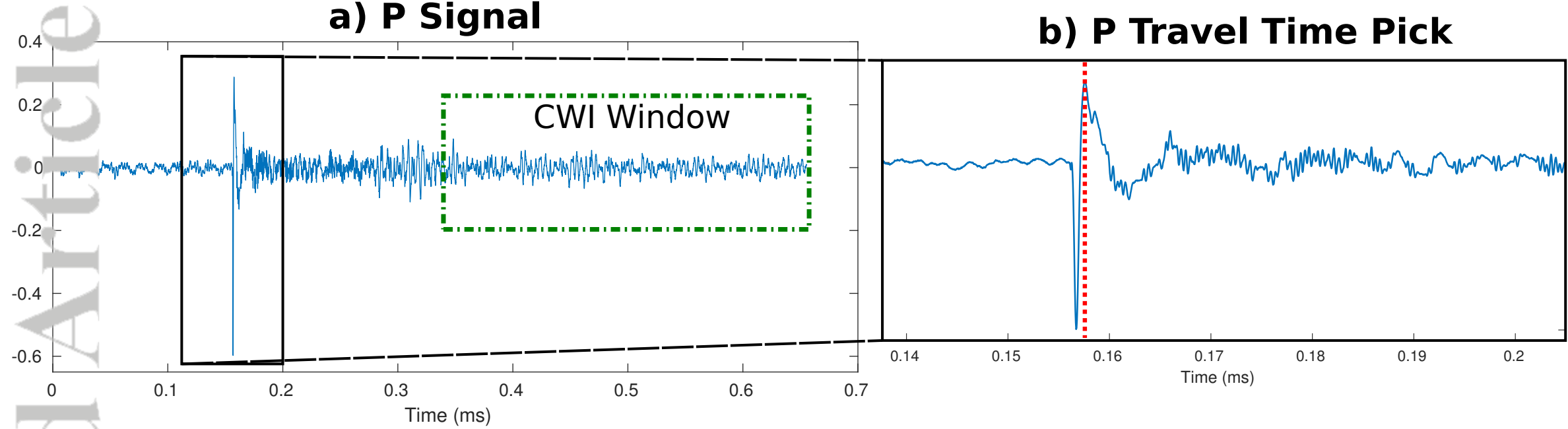

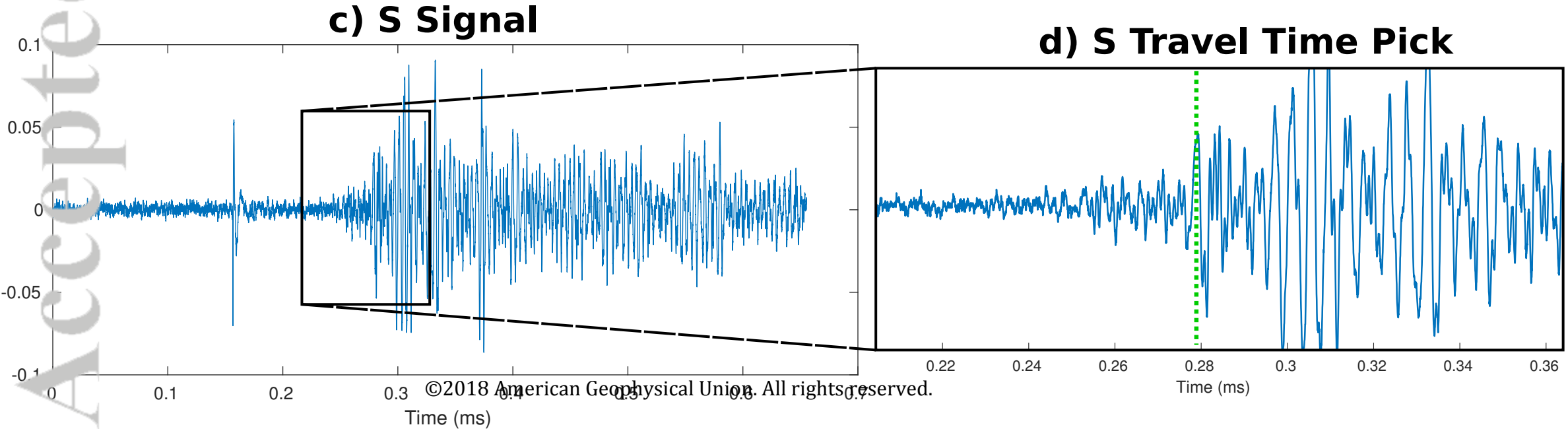

Figure 11.

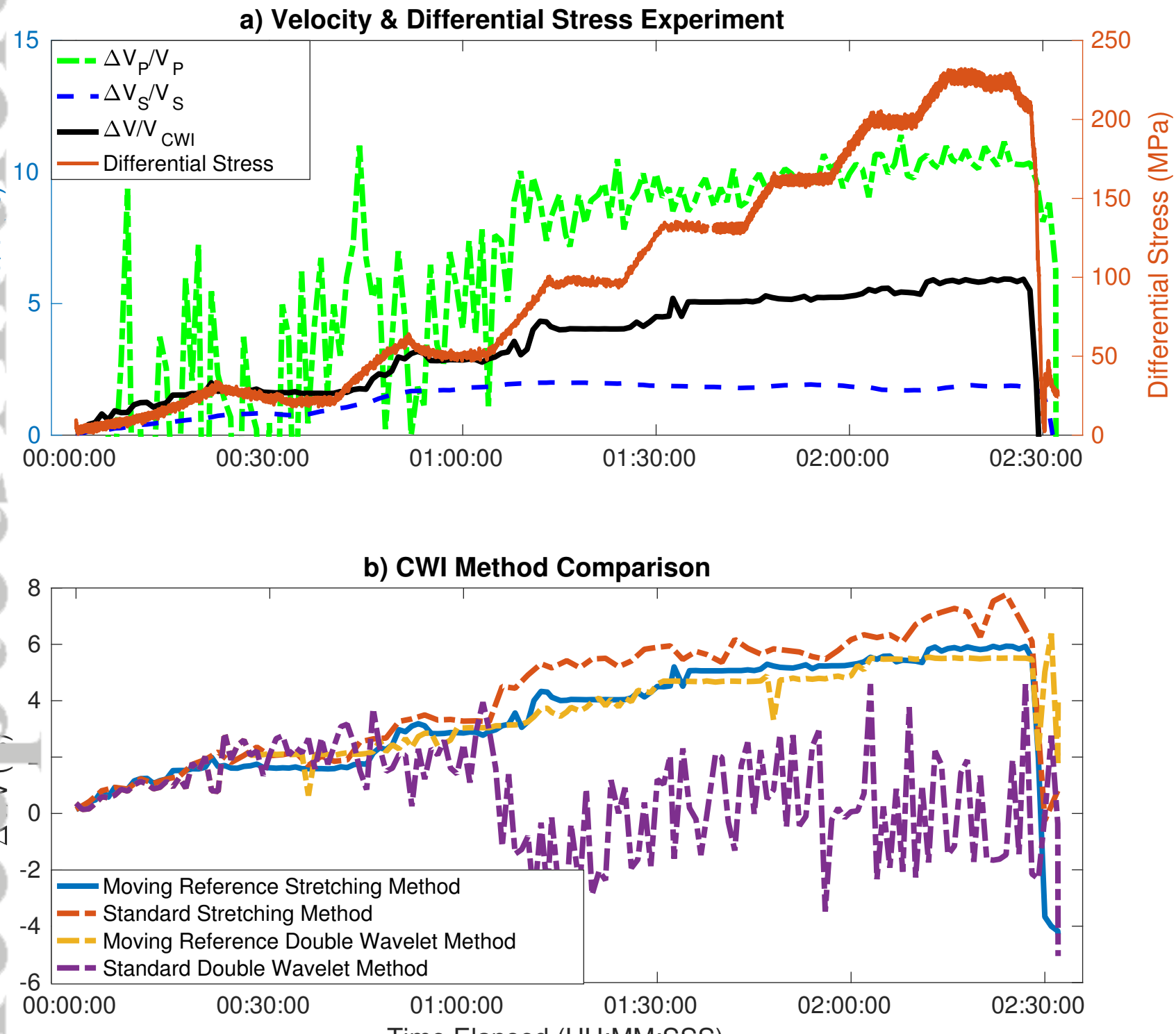

Figure 12.

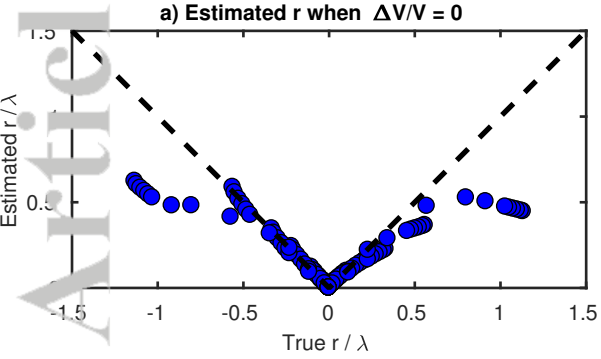

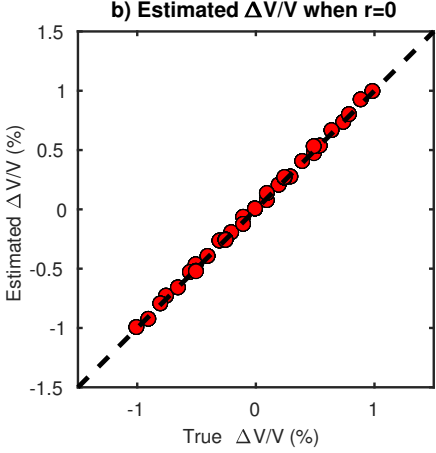

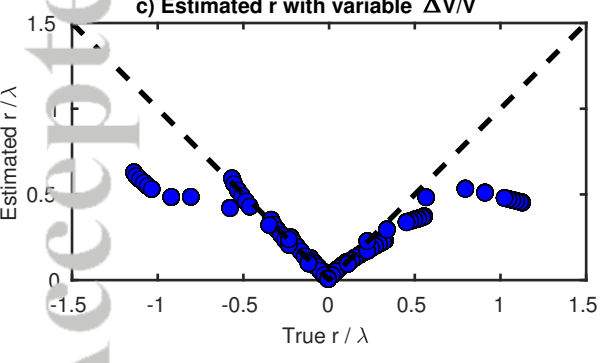

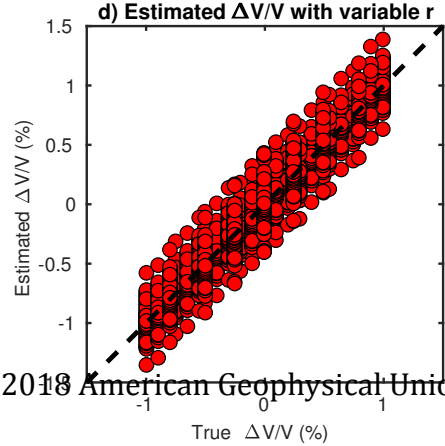

Figure 13.

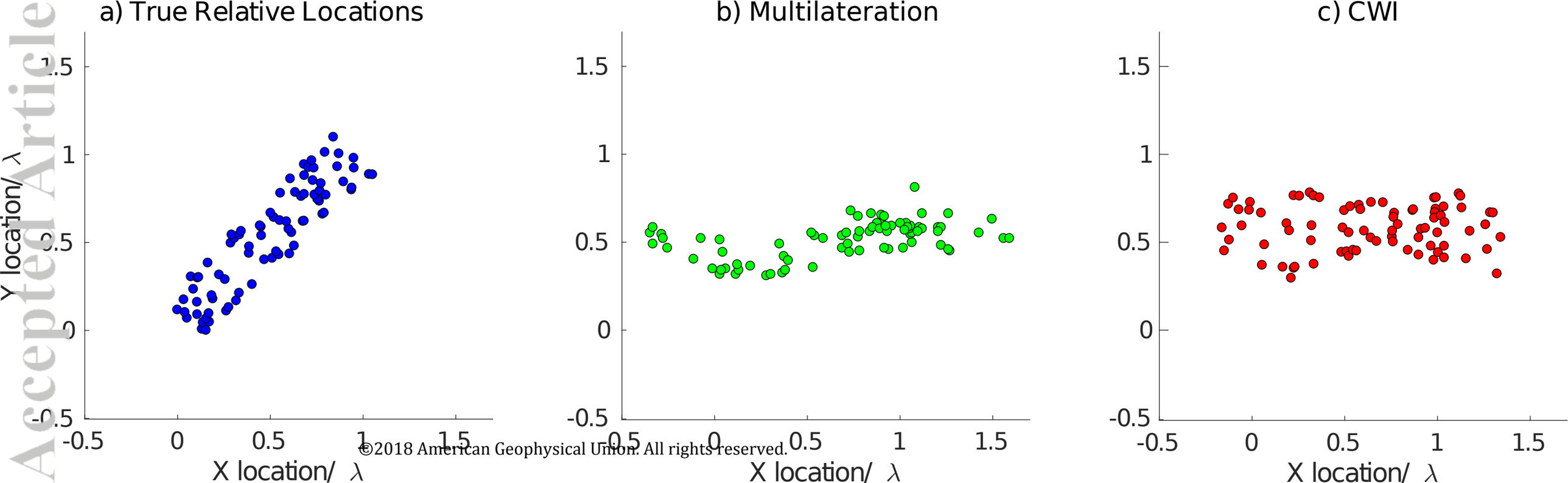

Figure 14.

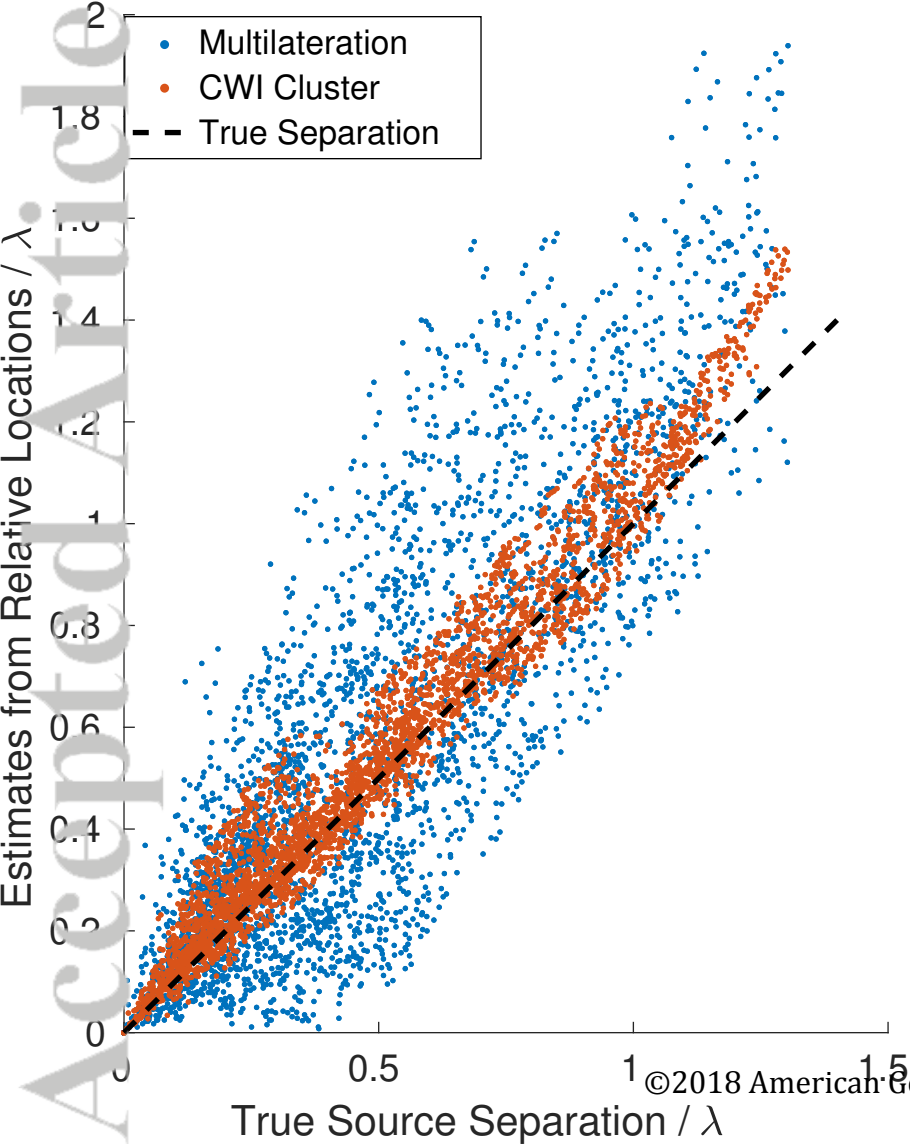

Figure 15.

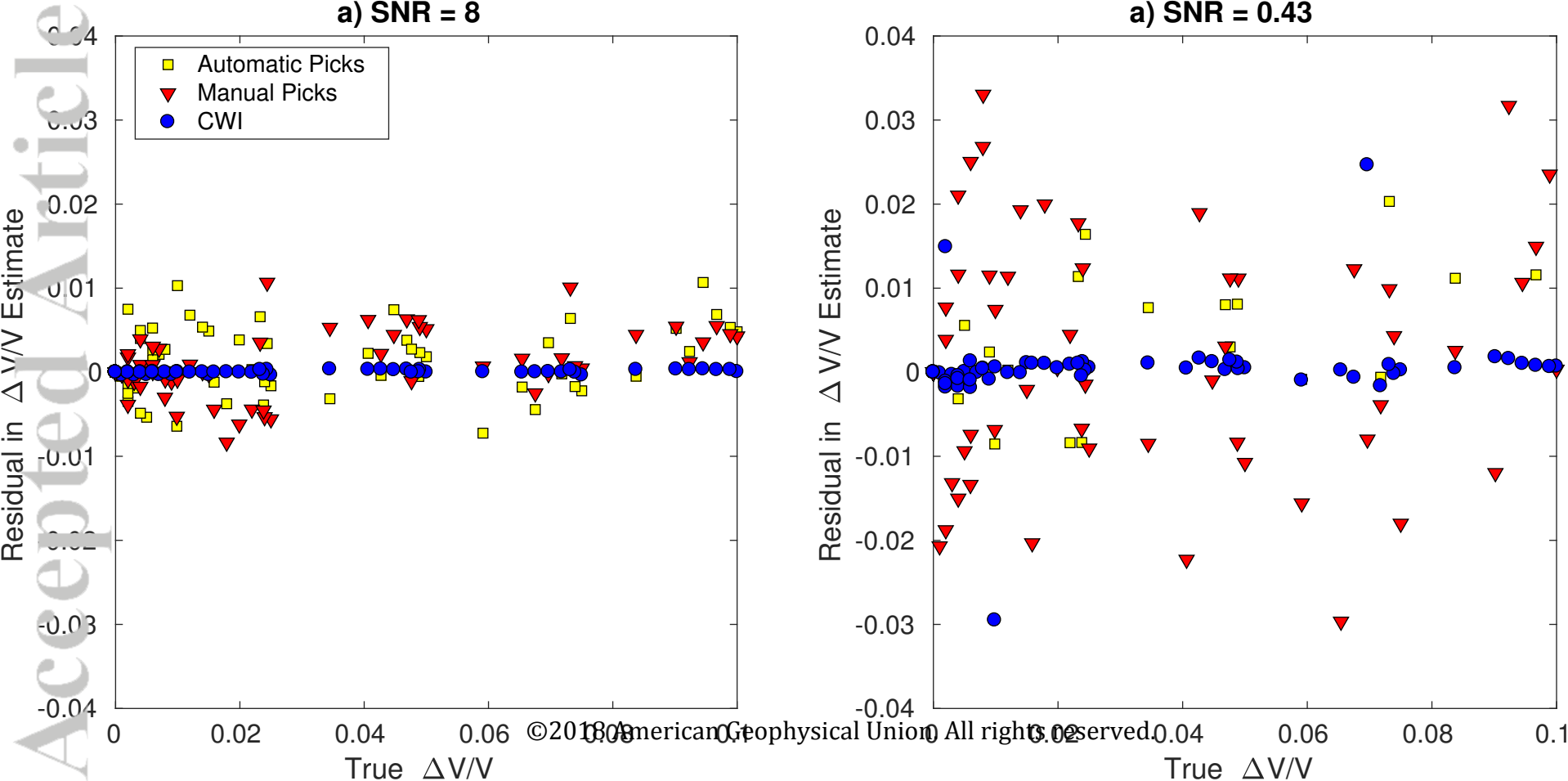

Figure 16.

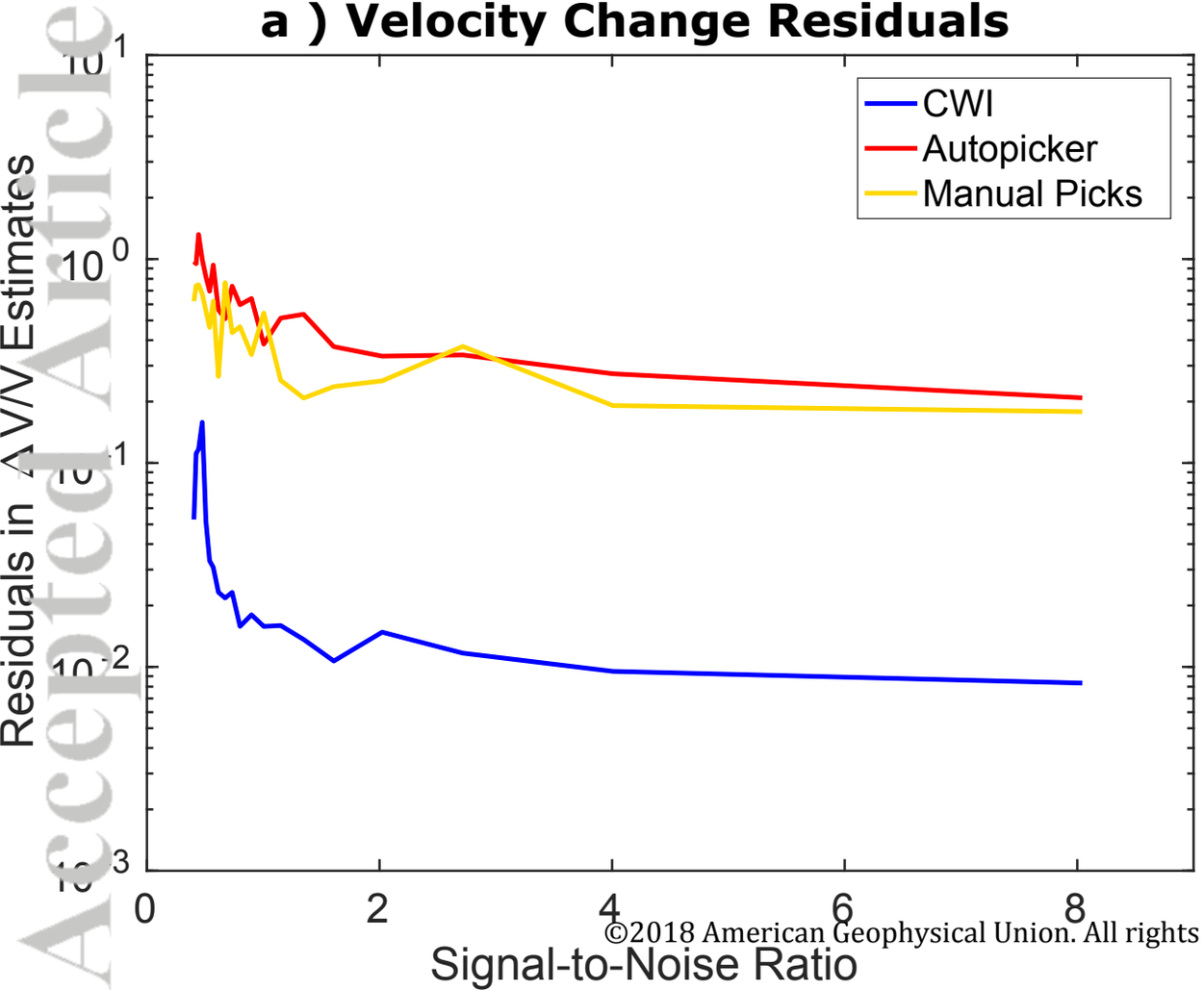

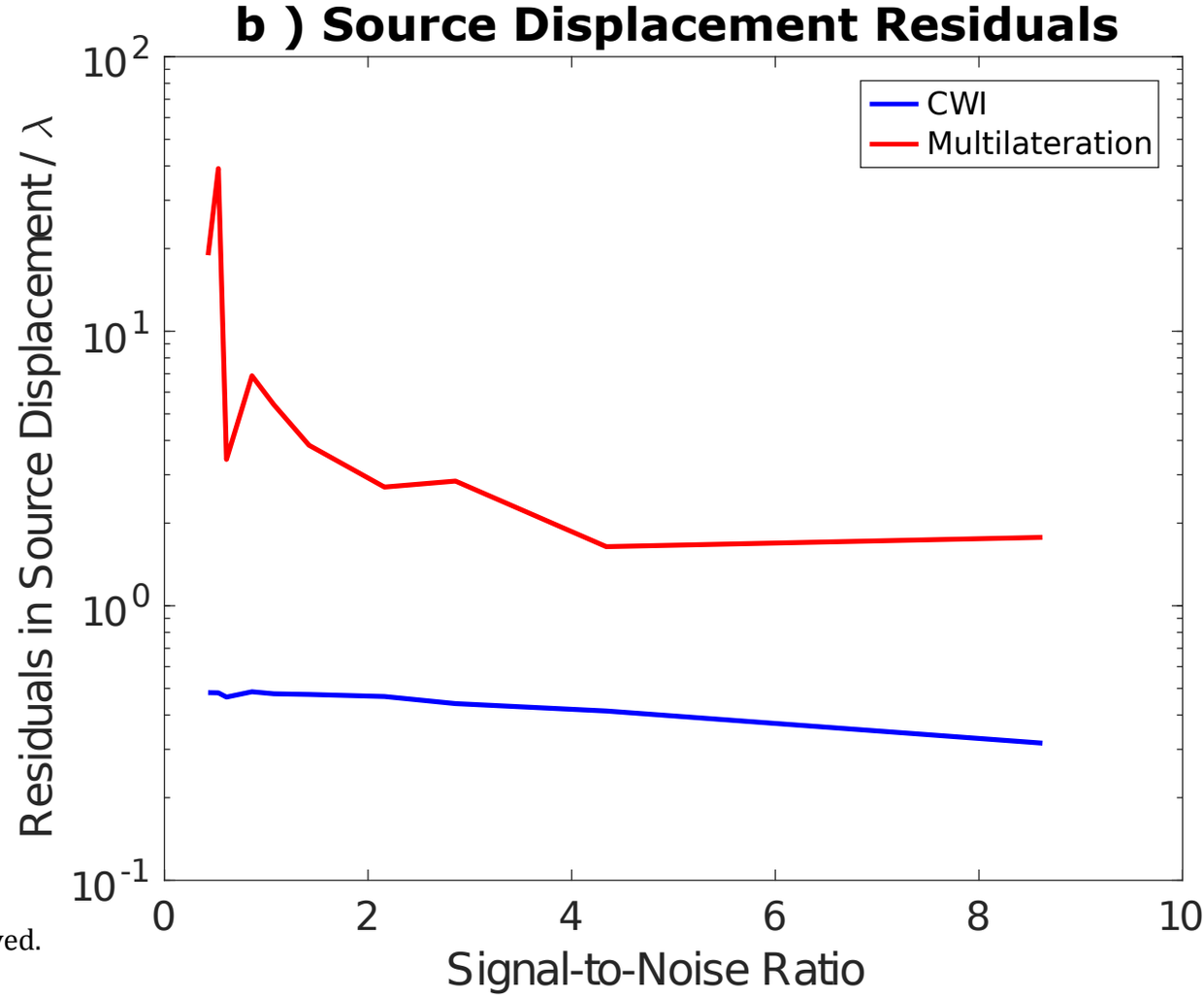

Figure 17.

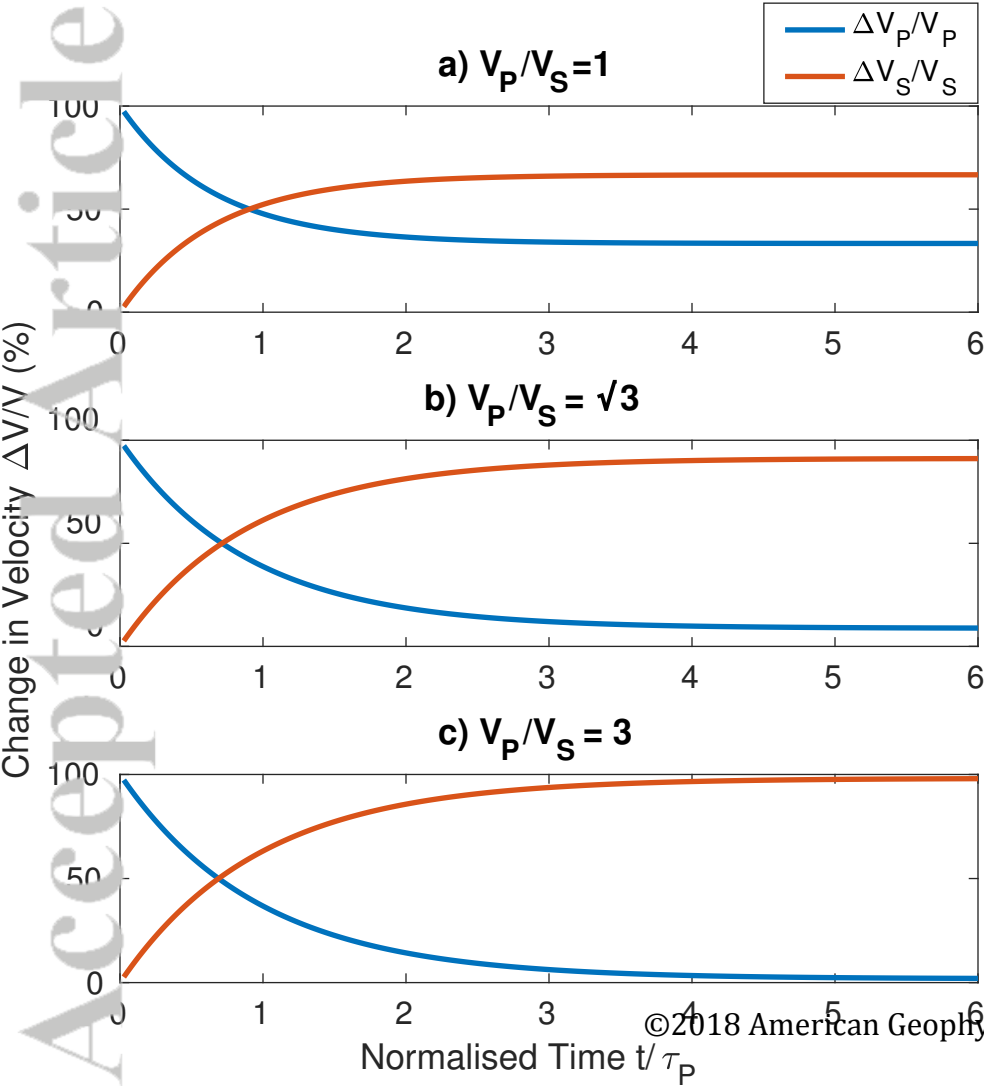

Figure 18.

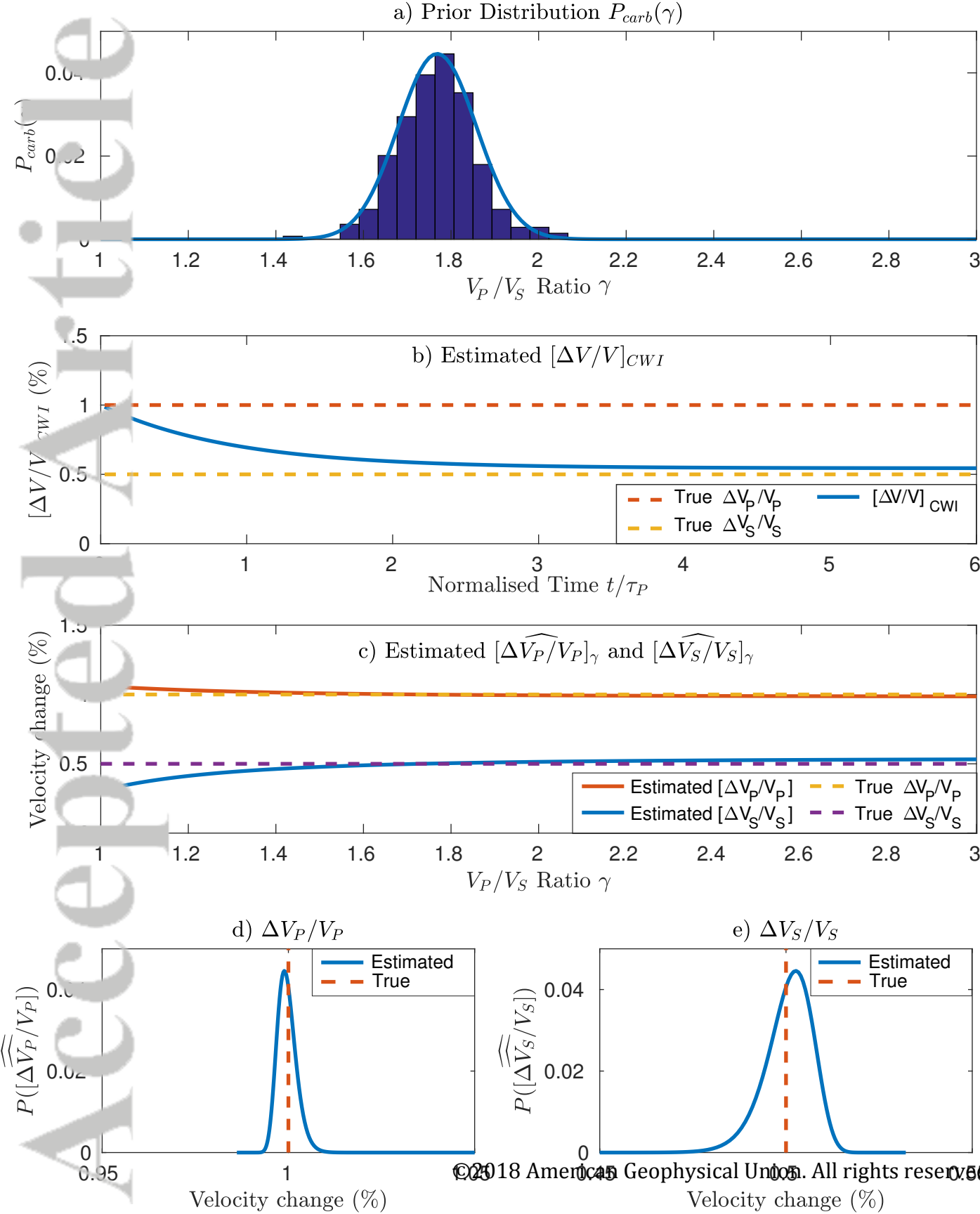

Figure 19.